Corrosion Studies on Thermally Sprayed Materials for Hexavalent Chromium Replacement

A Dissertation Presented

by

Ravi Manik Dey

To

The Graduate School
in Partial Fulfillment of the
Requirements
for the Degree of

Doctor of Philosophy

in

Materials Science and Engineering

Stony Brook University

August 2012

Stony Brook University

The Graduate School

Ravi Manik Dey

We, the dissertation committee for the above candidate for the
Doctor of Philosophy degree, hereby recommend
acceptance of this dissertation.

Prof. Christopher M. Weyant – Dissertation Advisor

Adjunct Professor, Department of Materials Science and Engineering, Stony Brook University

Prof. David O. Welch

Senior Scientist Condensed Matter Physics and Materials Science Department

Brookhaven National Laboratory & Adjunct Professor, Department of Materials Science and Engineering, Stony Brook University

Prof. Charles M. Fortmann

Adjunct Professor, Department of Materials Science and Engineering, Stony Brook University

Prof. Chad S. Korach

Assistant Professor, Department of Mechanical Engineering, Stony Brook University

This dissertation is accepted by the Graduate School

Charles Taber

Interim Dean of the Graduate School

Abstract of the Dissertation

Corrosion Studies on Thermally Sprayed Materials for Hexavalent Chromium Replacement

by

Ravi Manik Dey

Doctor of Philosophy

in

Materials Science and Engineering

Stony Brook University

2012

Electroplated hard chrome (EHC) is used for wear and corrosion resistance applications in many industries. The hexavalent chrome present in the plating baths is a major concern due to its highly carcinogenic behavior. . In addition, EHC has technological problems including micro and macro cracking, inconsistent corrosion protection, long processing time and wide differences in behavior of coatings deposited by different plating houses. Thermally sprayed (TS) cermet coatings with a hard ceramic (e.g. tungsten carbide (WC)) embedded in a ductile matrix (Co, Cr and/or Ni) are being developed as candidates for chrome replacement. Thermal spray techniques, specifically high velocity oxy-fuel (HVOF), provide an environmental friendly method for coating surfaces and are increasingly used for wear, friction and corrosion protection. However, to validate the TS cermets, the issue of interconnected porosity, usually a marked characteristic of TS coatings, needs to be addressed. In this study, the influence of processing parameters on the corrosion performance of HVOF-deposited metallic and cermet coatings has been determined. Electrochemical studies including open circuit potential and cyclic polarization were performed to assess corrosion susceptibility and passivation behavior. The results indicate a strong correlation of processing parameters, in situ particle state and mechanical properties with corrosion behavior.

Dedication

This dissertation is dedicated to my Parent, Teachers and Sister who had always encouraged me for higher studies and research!

Contents

Abbreviations

APS	Atmospheric Plasma Spray
CS	Cold Spray
CTSR	Centre for Thermal Spray Research
CVD	Chemical Vapor Deposition
DJ	Diamond Jet
$\mathbf{E_{corr}}$	Corrosion Potential
EHC	Electroplated Hard Chrome
EIS	Electrochemical Impedance Spectroscopy
Hex-Cr	Hexavalent Chromium
HPPS	High Pressure Plasma Spray
HVAF	High Velocity Air Fuel
HVLF	High Velocity Liquid Fuel
HVOF	High Velocity Oxygen Fuel
HVOGF	High Velocity Oxygen Gas Fuel
HVOLF	High Velocity Oxygen Liquid Fuel
IPS	In-Situ Plasma Spray
JK	Jet Kote
LPPS	Low Pressure Plasma Spray
OCP	Open Circuit Potential
PD	Potentiodynamic
PSZ	Partially Stabilized Zirconia
RF	Radio Frequency
RPS	Reactive Plasma Spray
SCC	Stress Corrosion Cracking
SEM	Scanning Electron Microscope
TS	Thermal Spray
VPS	Vacuum Plasma Spray
WSP	Water Spray Plasma

List of Figures

List of Tables

Acknowledgments

It gives me pleasure to highly acknowledge my supervisor Prof. Christopher M. Weyant for introducing me to the world of corrosion of thermally sprayed materials. I am grateful to Prof. Sanjay Sampath and Prof. Christopher M. Weyant for allowing me to work in the CTSR laboratory and perform experiments on corrosion of thermal sprayed (TS) materials. Furthermore, I am grateful to them for encouraging me to pursue the corrosion of different TS materials.

My special thanks are to David O. Welch for giving invaluable suggestions regarding corrosion experiments.

My sincere thanks are to Dr. Wanhuk Brian Choi , Dr. Dimitrios Zois and Dr. Alfredo Valarezo for providing the samples on WC-Co, Ni and NiCr. Further I thank them for clarifying the concepts on thermal spray.

I am grateful to my lab mates who constantly assist me in my research work. Without them my work wouldn’t have progressed. Am thankful to Salvatore Marino, Dr. Gopal Dwivedi, Travis Wentz, Dr. Yang Tan, Dr. Kentaro Shinoda, Sue Liang, Jongkwon, Ari Sagiv, Vaishakh.

Also, I am grateful to Mrs. Debbie Michienzie and Lynn Allopenna for helping in the needful paper works.

Furthermore, I would like to thanks my beloved friends Shayan Mysore Byrappa, Saurabh Patel, Saurabh Sheravat, Mehul Mehta, Talapady Vatsa Bhat, Omkar Aphale, Saurabh Joglekar, Kailash Raghuvanshi, Vaishak Viswanathan, Aruna Devi, Anthony Maiarano, Diya Bhattacharya, Divya Bhatnagar and others who have assisted me throughout the Ph. D course time.

Also am thankful to all the people who have knowingly and unknowingly assisted me in my research.

Chapter 1

Corrosion and Corrosion Mitigation

1.1 Introduction

Corrosion is a natural process that enables materials to gain lowest potential energy state. It can be defined as *a chemical or electrochemical reaction between material, usually a metal, and its environment that produces a deterioration of the material and its properties* [1]. Corrosion of metals is a worldwide problem leading to loss of billions of dollars, natural resources in the form of metals and fuels, mechanical properties, and aesthetic appearance. Further, it is of great concern since it endangers life due to catastrophic failure of functional components during operation [1]. Figure 1.1 illustrates the corrosion of different systems and the impact on the human civilization. Therefore it is necessary to control and mitigate the effects of corrosion.

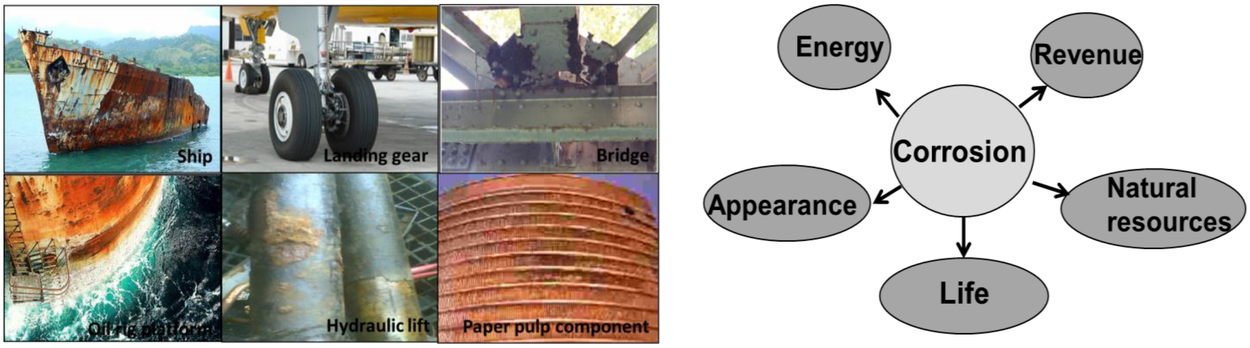

(a) (b)

Figure 1.1: (a) Corrosion in different systems. (b) Impact of corrosion on human civilization.

1.2. Concepts in Corrosion

In this section certain terminologies and conventions pertinent to corrosion and their usage in the present work is described [2].

1.2.1 Definitions

Oxidation: It is a process in which there is loss or emission of electrons. In this process the oxidation number (formal charge) of an element is increased [2].

Reduction: It is a process in which there is gain or consumption of electrons. In this process the oxidation number (formal charge) of an element is reduced [2].

Redox reaction: The simultaneous occurrence of oxidation and reduction reaction is called redox reaction. Any chemical reaction involves a redox reaction to maintain charge conservation. In an electrochemical reaction there is donation or acceptance of electrons. Electrons cannot exist in free form in solution. Hence, the electrons emitted during oxidation are simultaneously consumed during reduction [2].

In the following reaction, Ox is the oxidizing agent, Red is the reducing agent and n is the number of electrons taking part in the reaction.

$$\mathrm{Ox} + \mathrm{ne}^- = \mathrm{Red} \tag{1.1}$$

In the redox reaction, the oxidizing agent gets reduced whereas the reducing agent gets oxidized.

Electrolyte: In general, electrolyte consists of a solvent, and dissolved solutes which dissociates into cations and anions.

Anode: It is the part of electrochemical cell through which the positive electric current enters the electrolyte. In corrosion the corroding metals are anode. The metal ions enter the electrolyte leaving electrons in the anode [2,3].

Cathode: It is the part of electrochemical cell through which the positive electric current leaves the electrolyte. During corrosion the electrons formed on anode due to dissolutions are consumed by cathode [2,3].

Electronic current: It is the current constituted by electrons.

Ionic current: It is the current constituted by ions. Generally, current transported through electrolyte are ions.

Figure 1.2 shows a typical electrochemical cell for corrosion. In corrosion anodic or oxidation reaction takes at anode whereas cathodic or reduction reaction takes place at cathode. Thus corrosion takes place at the anode where the metal ions enter into the electrolyte and weight loss occurs. During the anodic reaction, electrons left behind the metal whereas the metal ions enter the solution. At the cathode the direct electronic current enters through the metal connection and electrons are consumed by cathodic reaction. The direct current passing through the electrolyte is the positive ionic or cationic current which flows from anode to cathode, and negative ionic or anionic current flows from cathode to anode.

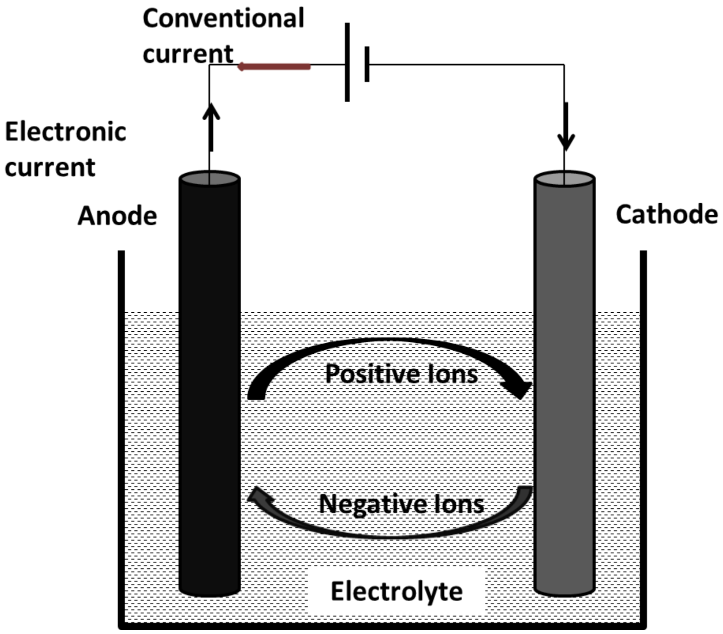

Figure 1.2: Schematic of electrochemical cell for corrosion.

1.2.2 Requirements of Corrosion Cell

The main requirement for corrosion cells are anodes, cathodes, electrons and ions as depicted in figure 1.3a. The anodes and cathodes may not be necessarily physically apart. They can be present on the metal surface in contact with electrolyte as shown in figure 1.3 b [3]. In the solution these electrodes are connected by ionic path whereas through the metal they are connected by electronic path.

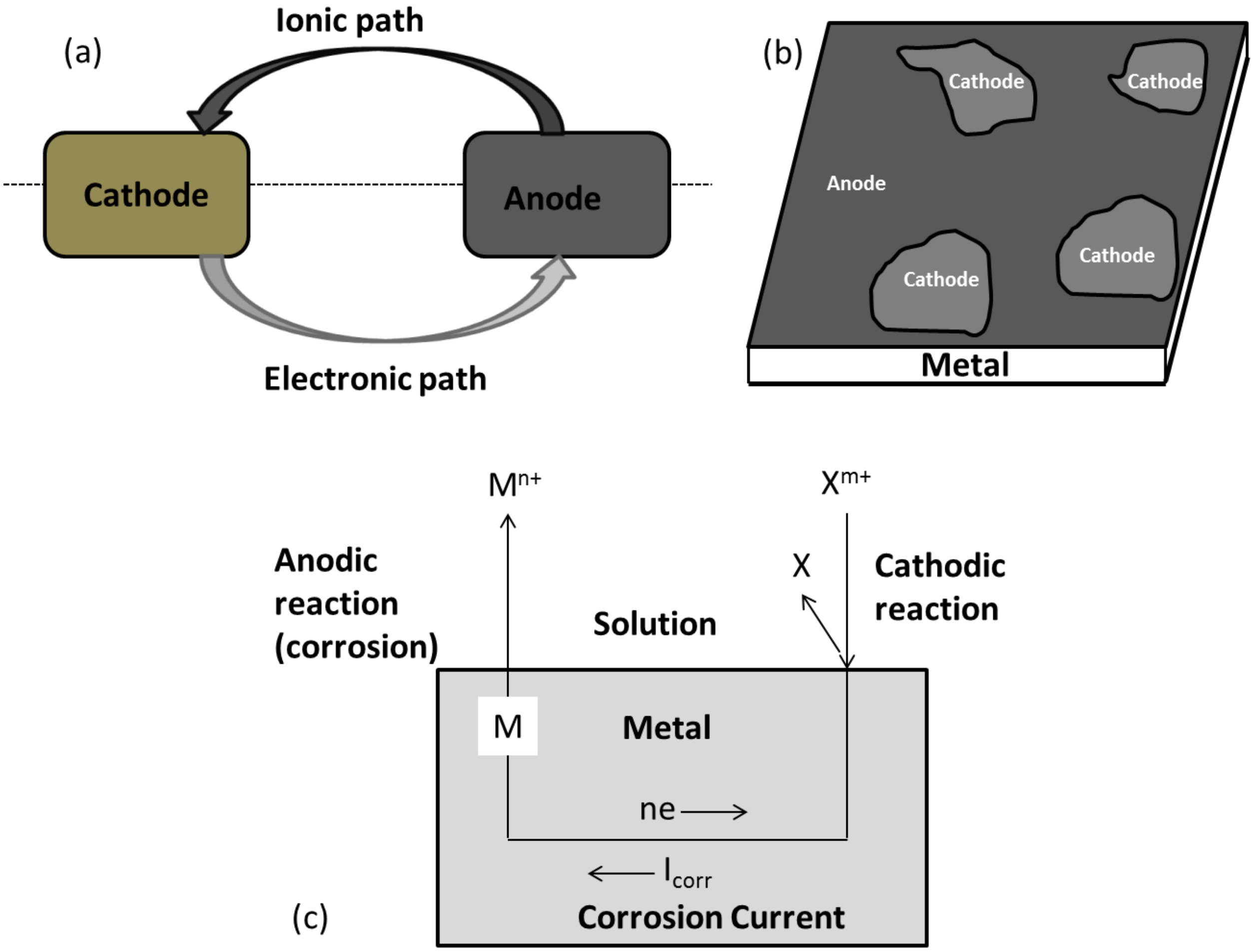

Figure 1.3: (a) Requirements of electrochemical cell. The electronic path direction is the conventional current path. (b) Schematic of local action cells on an enlarged metal surface. (c) Schematic of anodic and cathodic reaction on the metal immersed in electrolytic solution [4].

Corrosion depends on physical and chemical process occurring at the interface between the solid and electrolyte. The composition of bulk of a solid is also important factor playing role in the corrosion process. In general, the solid may have alloying elements with their own chemical and electrochemical properties, composites with inclusions, multiphase solids, solids with grain boundaries and segregation along grain boundaries. Also, solids have various types of defects and dislocations, stress distribution and these factors affect lead to formation of local electrochemical cells [5].

1.2.3 The Electric Double Layer Formation and Electrode Potential

Every material has a net negative charge when viewed from outside (vacuum) since the valence electrons even though mobile are not shared beyond the surface [6]. Nearest the surface within the metal net positive charge arises due to the presence of positive nuclei and requirement of charge neutrality and this situation is depicted in figure 1.4.

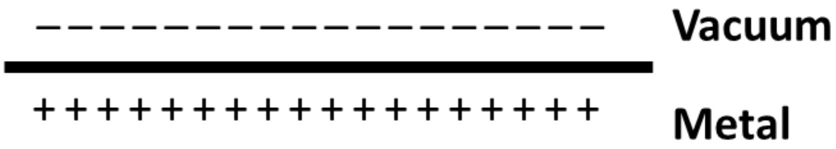

Figure 1.4: The charged interface of metal surface in vacuum [6].

The electric field emanating from the charged surface extends in the vacuum. Once the surface is introduced in a medium like air or water the electric field extends to a very short distance into the environment. Water molecules being polar and asymmetric in structure, the positive end gets attracted to the negative charged surface. The negative end points away from the surface. If any cation of any chemical species is present in the solution, it gets attached to the negative end of the water dipole. These cations on account of their strong electric field attract other water molecules from all direction such that the positive pole points away from the cation. Hence, the cations approach the metal surface surrounded by water molecules. Since the charged metal surface is already covered by monolayer of water molecules, the solvated cations reside at a finite distance from the surface. The imaginary plane passing through this closest cations and parallel to the metal surface is referred as the outer Helmholtz Plane (OHP). Sometimes chemical gradients can result in the adsorption of ions at the charged interface. These ions loose solvation and can have charge same or opposite of the electrode. Hence, the monolayer adjacent to the metal surface contains adsorbed anions and water molecule. The imaginary plane passing through the hydrating monolayer sheath is referred as inner Helmholtz Plane (IHP). The metal surface has large number of electrons compared to the adsorbed water molecules and thereby excess charge density is present at the interface. Consequently to maintain charge neutrality positive charges (cation) accumulate in the OHP. Hence these two layers formed is called *electric double layer* and is of immense importance to corrosion phenomena. The interaction of the cations in OHP with the metal surface is long range electrostatic force and is independent of the chemical properties of the cations [6.7].

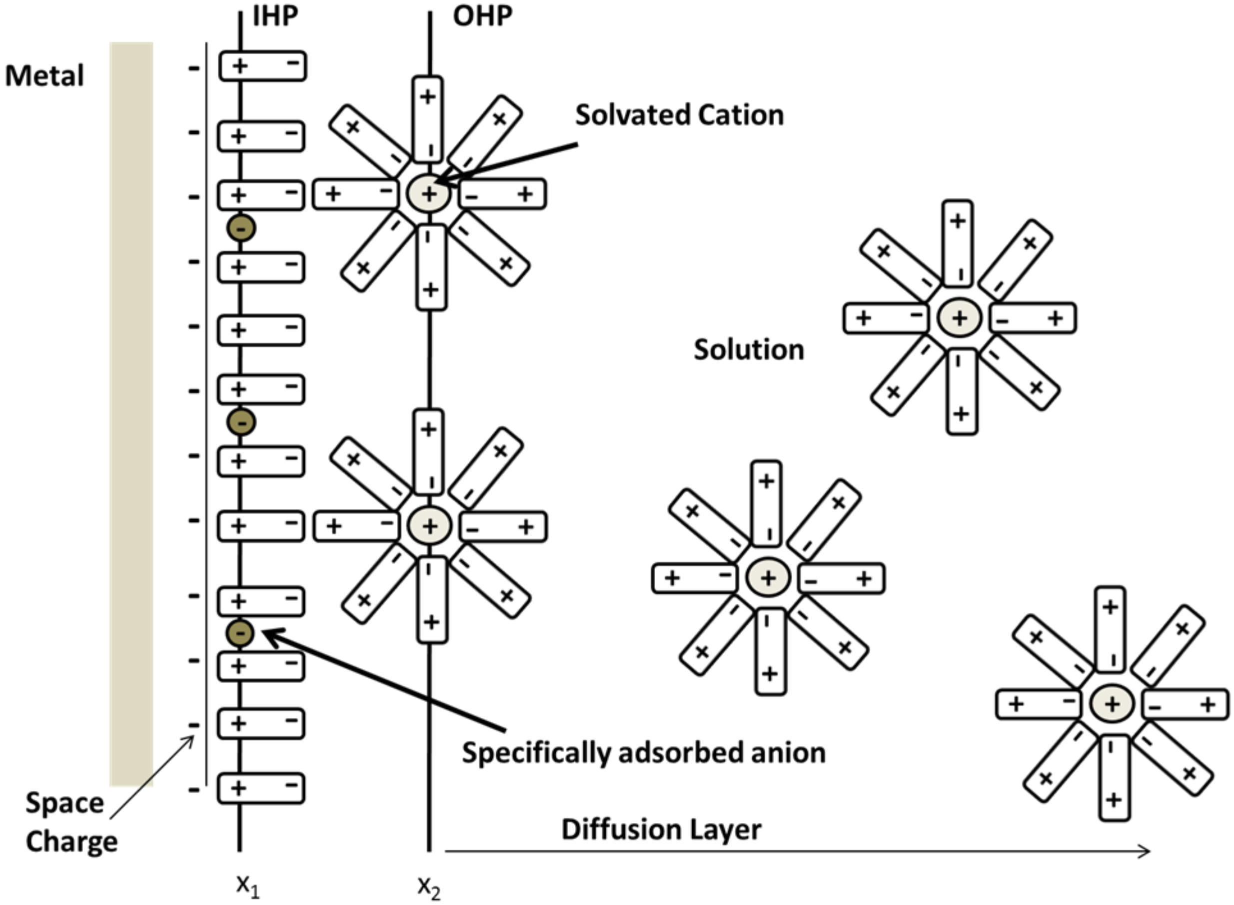

Figure 1.5: Proposed model for electric double layer showing position of IHP and OHP showing specifically adsorbed anion. X1 and x2 are the distances from the metal surface. The distance x2 signifies transition from compact to diffuse layer [7].

The electric double layer mimics a capacitor with parallel plates and carrying opposite charges separated by small distance. The presence of charges similar to capacitor produces potential from negative to positive as the distance is swept from metal surface to OHP. These potential creates electric field (~1E8 V/m) across the double layer and is characteristics of the electrolyte and metal electrolyte solution combination. This double layer is a sub part of the total electric double layer. Beyond the Helmholtz layer, the ions on account of their thermal energy show 3-dimensional diffuse distribution from OHP to bulk of solution and this layer is called as diffuse layer whose thickness depends on ionic concentration. The layer on the metal side is called space charge layer. Figure 1.5 shows the proposed model of an electric double layer combining Helmoltz and Guouy Chapman views which is commonly called as Grahamm model [7].

The electric double layer can form if a piece of metal is introduced in a solution containing ions of the metal or if due to interaction with the electrolyte ions of the metal goes in to the solution. An equilibrium is reached for the reaction taking place at the metal surface as

$$Me^{n+} + ne^{-} = Me \qquad (1.2)$$

Due to the formation of double layer the electrode has potential φ_m different from solution potential φ_s. Figure 1.6 shows the potential profile variation from electrode to solution across the double layer. The difference in Galvanic potential φ_m- φ_s , cannot be determined by direct measurement but a relative comparison with the Galvani potential difference of a reference electrode.

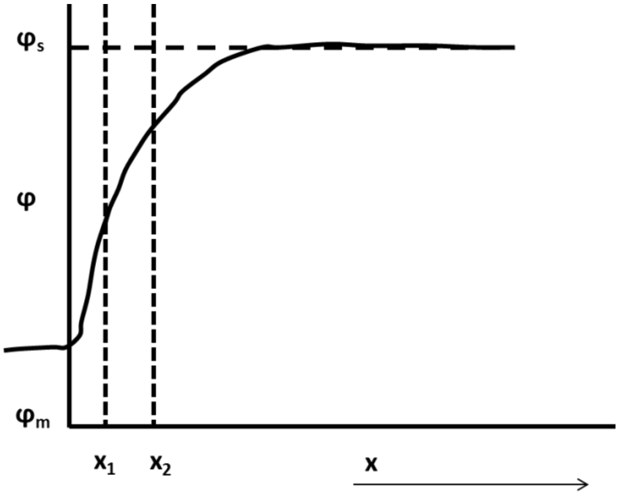

Figure 1.6: Potential variation profile across the double layer. Potential inside metal is constant [7].

A metal introduced in a solution attains the equilibrium potential when the two reactions anodic and cathodic reactions balance each other. The two reactions can take place on the same metal or on two dissimilar metals (or metal sites) that are electrically connected. Figure 1.7 describes this process [8].

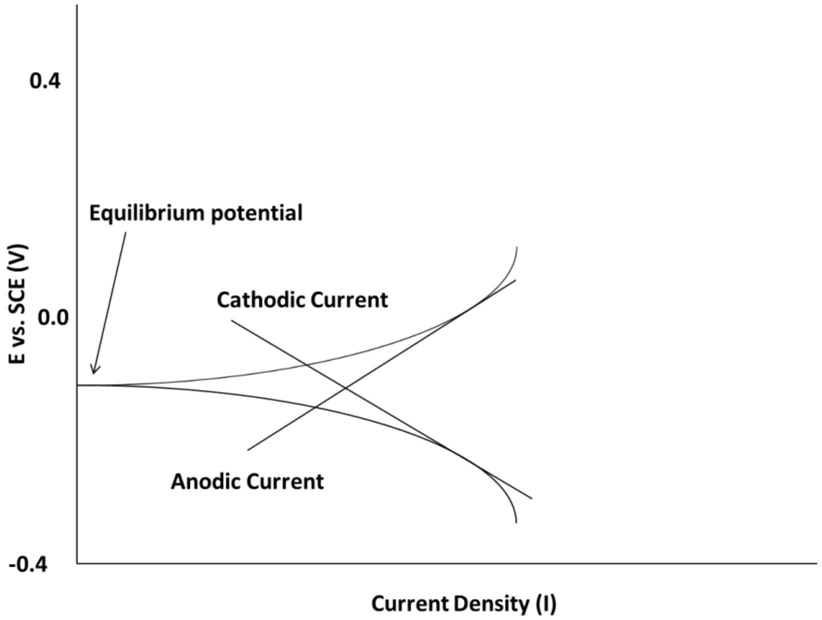

Figure 1.7: Corrosion process showing anodic and cathodic reactions [8].

The equilibrium potential of the metal maintains balance between anodic and cathodic reactions. If in an anodic reaction too many electrons are released in the metal, then these electrons shift the potential of the metal towards more negative end which slows the anodic reaction and speeds up the cathodic reaction [8]. It should be noted that as the metal continues to dissolve, more and more electrons are left back on the electrode and positive ions align in the adjacent solution as shown in figure 1.8 which is simplification view of figure 1.5. This opposing electric layer discourages further dissolution of the metal. Soon a dynamic equilibrium is reached where no net flow of ions into the solution. Sometimes if an oxide layer starts forming then electrons may be utilized for the oxide formation and potential seem to rise towards positive end.

The electron exchange depends on the electron affinities of the species and transfer occurs from metal to solution or vice versa till the electron affinities are equal. Sometimes the potential development across double layer can be without excess charges on either phase. When a metal is introduced in an aqueous solvent, water dipole aligns with preferential orientation. This situation is equivalent to charge separation across the interface and a constant potential exists. This potential will not be zero since energy will be spend on moving charges across the interface.

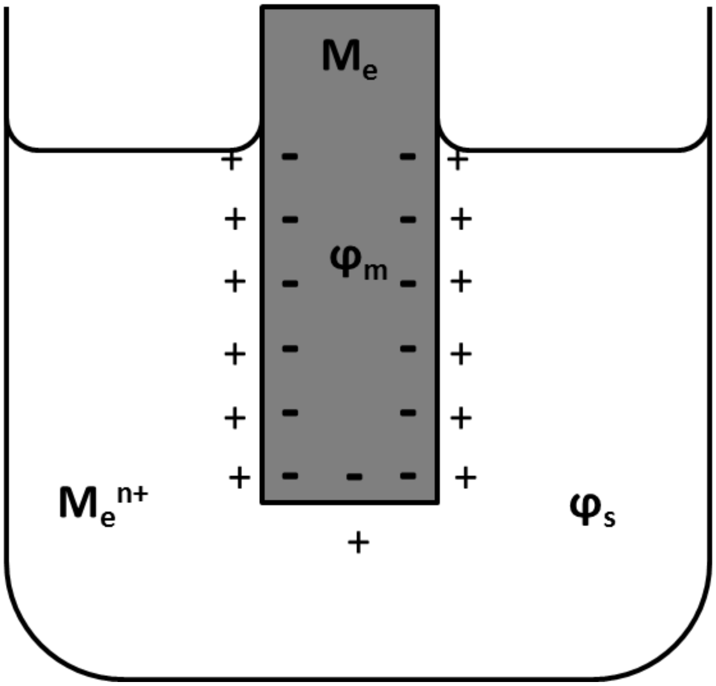

Figure 1.8: Metal in an aqueous solution in equilibrium with its ions. Double layer formed between the negative and positive charges [2].

1.2.4 Thermodynamics of Corrosion

Corrosion of metals takes place to return them to native state and reduce the free energy. The tendency for the interaction of the metal with its environment is measured by the changes in Gibbs free energy (ΔG). The more negative is ΔG, the greater is the tendency for the reaction to proceed. In the view of electrochemical mechanism of corrosion, the corrosion tendency of a metal is expressed in terms of EMF (E) of corrosion cells which are fundamental part of corrosion process. The relation between ΔG and E can be expressed by the relation

$$\Delta G = - nFE \qquad (1.3)$$

Where F is Faraday constant (96,500C/mole of e^-) and n is number of electrons taking part in the reaction. It is to be noted that ΔG is expressed in Joules if E is in volts. Hence, greater the value of E, greater is tendency of the metal to corrode.

Through the measurement and control of E, free energy can be measured and controlled. Through the control of electrode potential by external source the reaction shown in equation 1.2 can be driven left or right side and vice versa.

The electrode potential can deviate from equilibrium in a solution where the ionic concentration of the metal deviates from unity. Due to changes in potential either stable oxidized or stable reduced species can form. The Nernst equation relates the potential of electrode to the concentration of redox or oxidized species and temperature as follows

$$E = E^o – (RT/ nF) \ln (Red/Ox) \qquad (1.4)$$

Thus for a metal introduced in a solution of its ion the potential is given as

$$E = E^o – (RT/ nF) \ln (M/M^+) \qquad (1.5)$$

M^+ is concentration of ion in solution and M is concentration of metal in electrode.

1.2.5 Kinetics of Corrosion

Corrosion potential shows the tendency of the system to corrode in a given environment. Corrosion potential shows the equilibrium between anodic and cathodic reactions. Once this equilibrium is disturbed the system may undergo corrosion. The electrode is no longer in equilibrium if net current flows out or in from its surface. The amount of change of the potential depends on the magnitude and direction of the external current. The direction of potential change always tries to oppose the shift from equilibrium and flow of current which is either galvanic in origin or externally supplied. In the galvanic cell as the current flows anode becomes more cathodic and cathode becomes more anodic so that the potential difference between the electrodes becomes smaller.

Generally, it is assumed that in corrosion reactions anodic and cathodic processes are controlled by the kinetics of electron transfer mechanism at the metal surface. In the realm of the kinetic model, electrochemical reactions obey the Tafel equation [8].

$$I = I^{\circ}\, e^{(2.303(E-E^{\circ}/\beta)} \qquad 1.6$$

Where,

I = Current resulting from the reaction

I°= Exchange current which is reaction dependent constant

E= Electrode potential

E°= Equilibrium potential constant for a reaction

β = Tafel constant for a reaction (Units: volts/ decade)

The above equation describes the behavior of one reaction. However, corrosion involves two opposing reactions, cathodic and anodic, for which the modified equation commonly called as Buttler- Volmer equation is

$$I = I_{corr}\, e^{(2.303(E-E_{corr}/\beta_a)} - I_{corr}\, e\text{-}^{(2.303(E-E_{corr}/\beta_c)} \qquad 1.7$$

Where,

I = measured cell current in amperes

I_{corr} = corrosion current in amperes

E_{corr} = corrosion potential in volts

β_a = anodic Tafel constant (Units: volts/ decade)

β_c = cathodic Tafel constant (Units: volts/ decade)

From equation 1.7, it can be observed that near E_{corr}, cell current is zero as both the reactions contribute in equal amount. For potential far away from E_{corr}, the plot of potential vs. log I is straight line. The presence of linear curve on either side of Ecorr indicates that the system is kinetically controlled.

Concentration Polarization: In this case rate of reaction is controlled by the rate at which reactants reach the metal surface. At higher currents when diffusion of oxygen and hydrogen is not fast enough to maintain kinetically controlled rate cathodic reactions exhibit concentration polarization.

Oxide Formation: Oxide formation generally alters the surface of the metal which may lead to difference in Tafel constants compared to metal surface.

Mixed Control Process: In this case polarization ocurrs to certain extent at both anodes and cathodes.

Experimentally I_{corr} is found by the intersection of extrapolated cathodic or anodic linear curve with E_{corr}. However, in the modern electrochemical test simulation utilizing Buttler-Volmer equation is used where the fitting parameters are E_{corr}, I_{corr} and Tafel constants. A correct initial seed value helps in converging the experimental and simulated curve with low residues.

For current values near to Ecorr, Taylor series expansion of exponential terms in equation 1.7 gives Stern Geary equation

$$I_{corr} = (1/R_p)(\beta_a\beta_c/2.303\ (\beta_a+\beta_c) \qquad (1.8)$$

Where, R_p is polarization resistance.

For the dissolution of metal as expressed in equation 1.2 and using Faradays Law enables to calculate corrosion rate given by the equation

$$CR = I_{corr}\ KE_W/\rho A \qquad (1.9)$$

Where,

CR= Corrosion rate

K= Constant defining units of corrosion rate

E_w = Equivalent weight

A= Area of the sample under investigation in CGS units

P = density in CGS units

I_{corr}= Corrosion current in Amperes.

1.2.6 Classification of Corrosion

Nature of corrodent**:** Corrosion is classified as wet or dry depending on the availability of liquid generally moisture. In wet corrosion moisture or liquid is involved whereas dry corrosion involves reaction with high temperature gases.

Mechanism of corrosion**:** This type of corrosion involves either direct chemical or electrochemical reactions.

Appearance of corrosion**:** Corrosion can be either uniform where corrosion occurs over entire surface or localized where a small region is affected. In this type of corrosion morphology of attack is used and the common form of corrosion is shown in figure 2. Based on appearance of corroded metal eight forms of corrosion are identified. They are:

1) Uniform or general corrosion
2) Pitting corrosion
3) Crevice corrosion including corrosion under tubercles and deposits, filiform corrosion and poultice corrosion
4) Galvanic corrosion
5) Erosion- corrosion, including cavitation erosion and fretting corrosion
6) Intergranular corrosion, including sensitization and exfoliation
7) Dealloying, including dezincification and graphitic corrosion
8) Environmentally assisted cracking, including stress corrosion cracking and corrosion fatigue and hydrogen embrittlement
9) The eight different forms of corrosion are depicted in figure 1.9. In practice, there are corrosion cases where they fit in more than one category. Sometimes it is difficult to categorize a corrosion case in the above eight category.

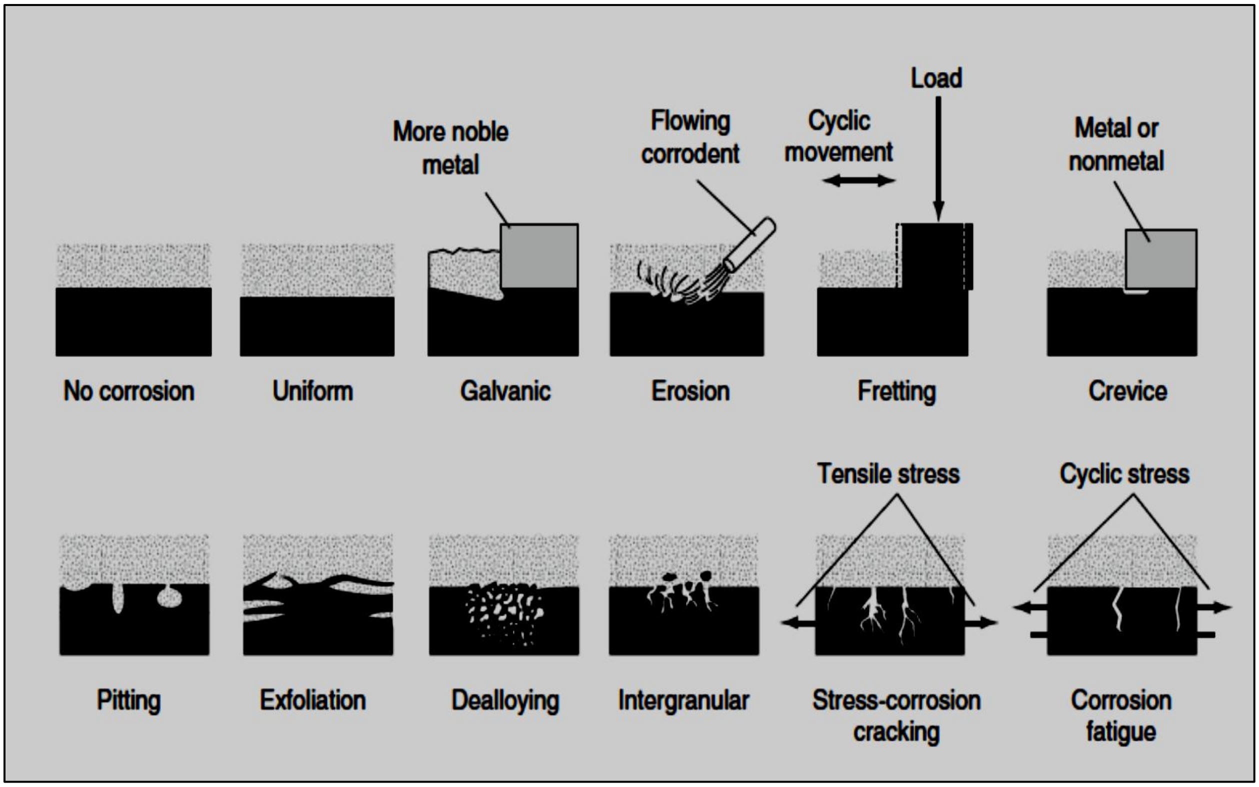

Figure 1.9: Schematic of different types of corrosion [1].

Depending on the dimension of corrosion attack, corrosion can be further distinguished into macroscopic localized corrosion attack or microscopic corrosion. The above eight corrosion can be categorized in to macroscopic or microscopic as shown in figure 1.10. Macroscopic corrosion attach can be visualized by naked eyes whereas microscopic corrosion takes place at atomic level and is very much insidious.

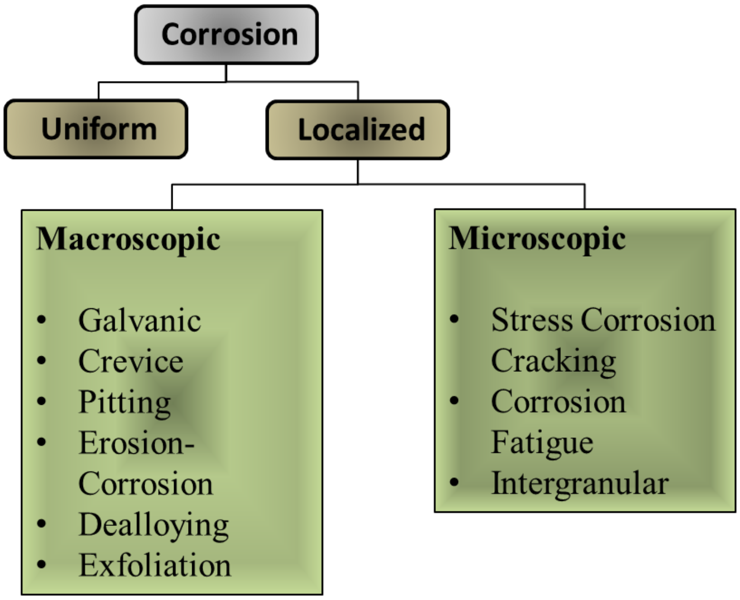

Figure 1.10: Corrosion classification based on dimension of corrosion attack [1].

1.3 Methods to Control Corrosion

Corrosion is inevitable! However, the kinetics of corrosion can be slowed down. The following four strategies have been employed to combat corrosion: design, mitigation, detection & prediction [9]. Of all these four techniques mitigation is widely used. It can be classified into active or passive. In active control prevention of corrosion is done using utilizing counter chemical reaction involving sacrificial anode, cathodic protection and inhibitors. Whereas, passive method includes use of metal coatings, organic or inorganic coatings which provide physical barrier between reactive substrate and environment.

Generally, corrosion proceeds from the surface to within the bulk of a material [10]. Hence protecting the surface of structural material from corrosion is of prime importance. Consequently, surface engineering plays a dominant role in controlling corrosion of a structural material. Over the past decades different techniques and methodologies have evolved to control corrosion. Nickel and chromium are important elements incorporated into corrosion resistant materials solutions. Electroplating is a common practice for coating the surface of component to give corrosion resistance. In particular, hard chrome is used for wear and corrosion resistant applications. Figure 1.11 shows the different metallic coating techniques used for surface protection [11].

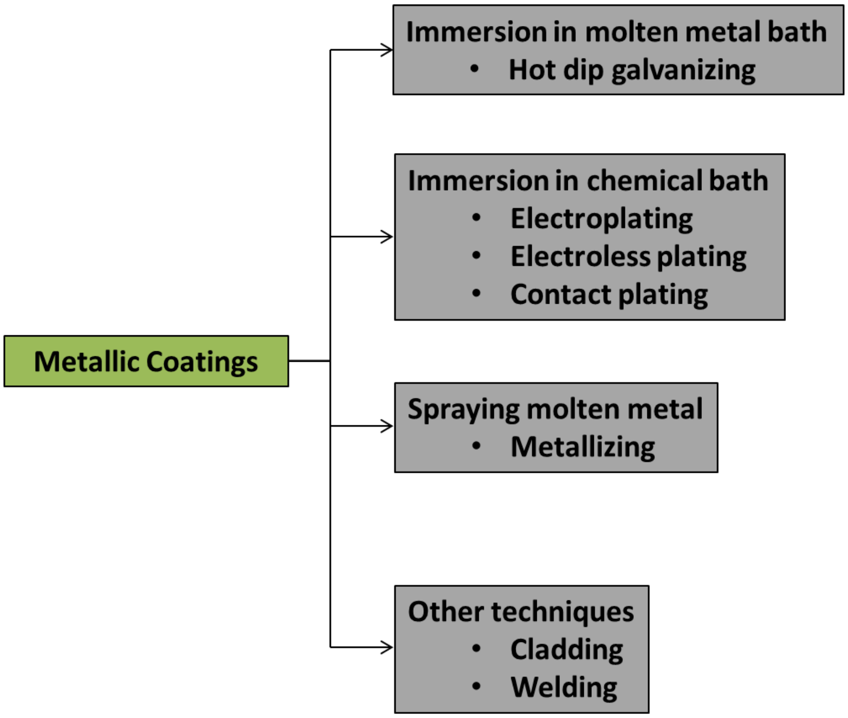

Figure 1.11: Different metallic coating applications [11].

With the advancement of technology, alternate techniques and materials are being adopted in industries in view of protecting the environment and, development of novel corrosion and wear resistant materials [12]. Vacuum chemical vapor deposition (CVD) techniques like sputtering and plasma, thermal spray (TS), and electro deposition processes are widely utilized for corrosion protection. Figure 1.12 shows the novel surface technologies adopted in the industries for anticorrosion and wear resistance coating applications. All the novel coating technologies have their range of processing parameter and coating characteristics. Figure 1.13 shows the range of deposition temperature and coating thickness for the different coating technologies [12, 13]. It is seen that thermal spray gives the opportunity to produce thick coatings at reasonably low temperature compared to other deposition techniques like CVD, PVD, ion implantation which have relatively low growth rate. In the present study, thermal spray deposition has been used for coating several metallic systems in order to study their corrosion behavior.

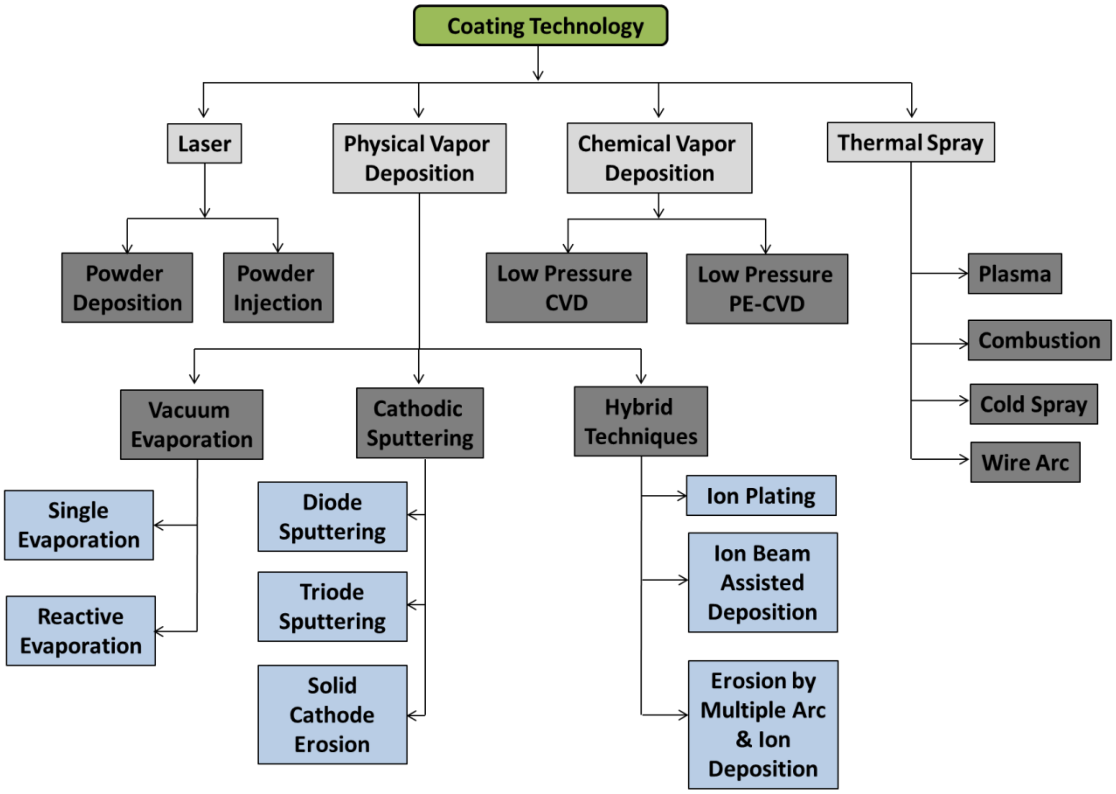

Figure 1.12: New coating technologies adopted by industries [11].

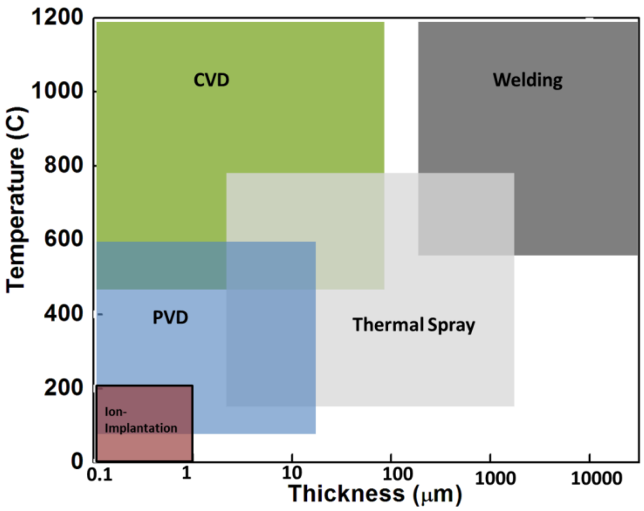

Figure 1.13: Various coating technologies shown according to process parameter and coating characteristics [12].

1.4 Thermal Spray

Coating by thermal spray (TS) offers the capability to coat a large substrate in normal atmospheric conditions. As shown in figure 1.14, in the thermal spray process solid feedstock (metallic or non metallic) in the form of particles, rods or wire are continuously fed and rapidly heated by arc, plasma jet or combustion flame, melted and accelerated towards the substrate to be coated [14]. The molten or semi molten particles due to their high velocity undergo flattening when they impinge against the substrate and rapidly cool down. Rapid solidification of the molten particles in the form of lamellae or splats builds up the coating by successive impingement of the particles [15, 16]. The splats are stacked on top of one another on every successive torch passes and the coating microstructure has the appearance of a brick wall. TS coatings differ from other coating processes in which coating formation takes place with the aide of atoms, ions, molecules or radicals. Instead, the fundamental coating structure is built particle by particle. Thermal spray coatings have various applications in optical, tribological, mechanical and electrical. Furthermore, TS coatings are utilized to protect the substrate from wear, corrosion, erosion chemical attack or heat. A major advantage of TS is that a wide variety of materials can be used for coatings and most all substrates can be coated [17]. Application of thermal spray technology for surface engineering has been carried out since the last century [18].

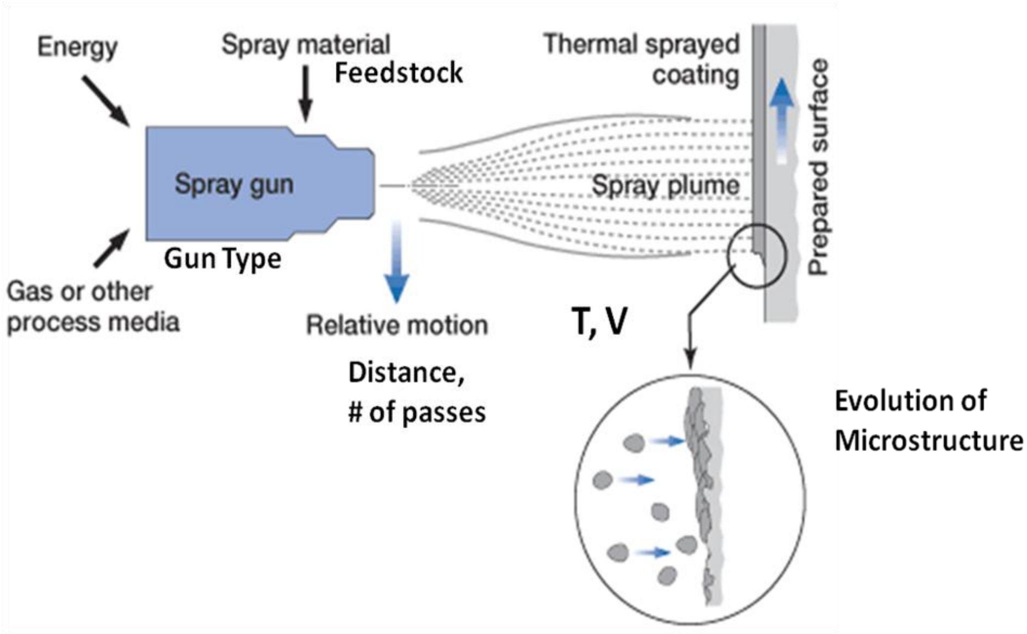

Figure 1.14: Schematic of thermal spray process [19].

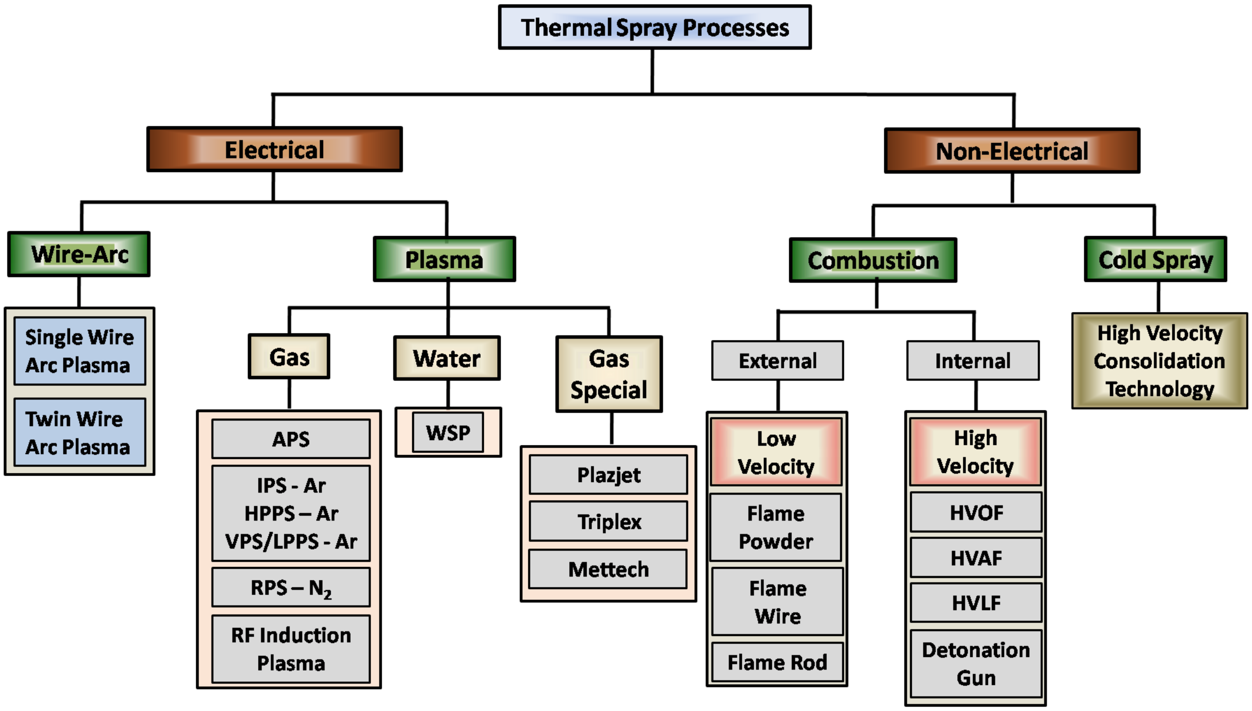

Figure 1.15: Classification of Thermal Spray Process [20].

Thermal spray consists of a suite of processes allowing for deposition of a variety of materials (Figure 1.15). Selection of a process depends on the starting material properties as well as the desired properties of the resultant coatings. In general, thermal spray coatings have a large number of defects including globular voids, inter-layer pores, splat boundaries, un-melted or partially melted particles, pores (0 – 10%), micro- and macro-cracks, metastable phases, oxide particle inclusions, etc [21,22,23]. Figure 1.16 shows the presence of defects in a typical TS coating [24, 25]. Furthermore, there are around 50 parameters in thermal spray influencing the defect levels in the coatings [23]. Due to the presence of these defects in various proportions the coatings exhibit a wide range of physical and chemical properties which are different from the bulk counterpart. Therefore, corrosion behavior of TS materials is quite complex and different from bulk materials. The present work aims at studying the corrosion behavior of several thermally sprayed materials.

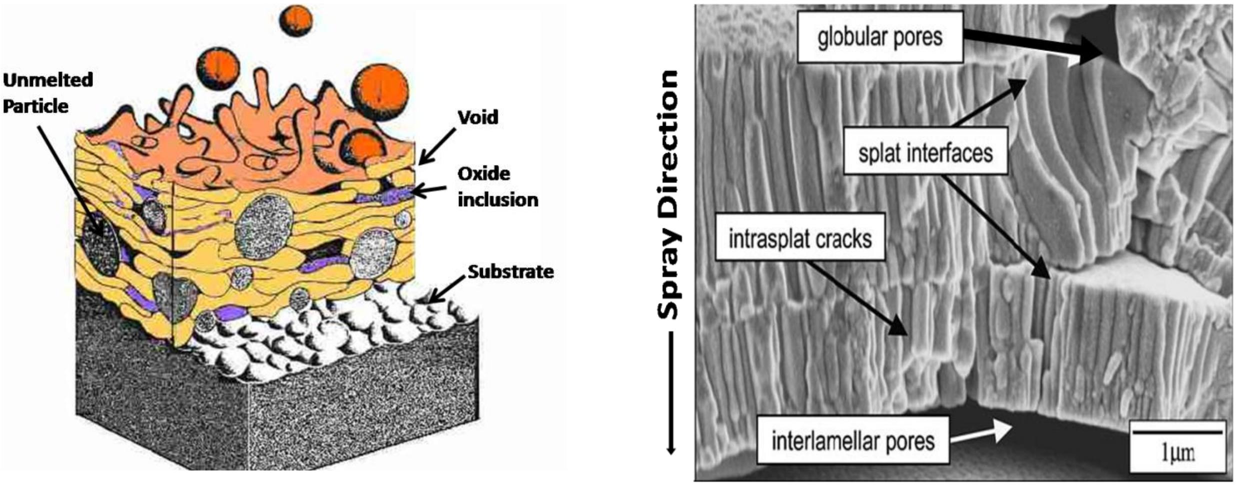

(a) (b)

Figure 1.16: (a) Schematic of a typical TS coating showing various defects [25]. (b) Cross-sectional SEM image of partially stabilized zirconia (PSZ) coating sprayed by APS exhibiting different types of defects [24].

In the past couple of years industries have stretched the operational limit conditions of equipment used for various market segments like structural components, automotive, turbines, earth moving machinery, etc in which steel, super alloys are used as structural materials [26]. With the advancement of ceramics and composite materials there has been metamorphosis of the traditional material processing and surface treatment and new techniques mentioned in section 1.7 are used along with the traditional approach. With the application of these techniques the multifunctional characteristics like corrosion-oxidation and wear resistance, thermal load bearing capacity, mechanical properties environmentally friendliness have achieved a new dimension. In this market thermal spray is successful in making its own niche position. With the integration of thermal spray coating with the structural material and better control of thermal spray process, coating properties, TS coatings are being viewed as prime reliant coatings. Due to multifunctional demand from the coating and longevity of the engineering components it is necessary to establish the reproducibility and reliability of the coating characteristics. In the present research reproducibility and reliability of corrosion measurement has been addressed [26].

1.4.1 Steps in TS Coating

TS process is very complex coating process and as shown in figure 1.16 it involves formation of coating splat by splat with the interaction of particle and energetic gases. The development of the coating can be divided into following stages [26]:

1) Introduction of feedstock into the combustion flame.

2) Particle flame interaction.

3) Coating built up splat by splat.

4) Post coating phenomenon like development of residual stresses.

FeedStock: The size and shape of feedstock is very important while considering coating formation. The dimension of the splats in the coating affects the performance of the coatings like corrosion. Small particles owing to their large surface to volume ration are susceptible to overheating which can lead to excessive oxidation or decomposition. On the other hand large particles may not get sufficiently heated during the flight due to which they are often un melted. This results into porous microstructure and poor corrosion performance. Also, the larger particle remaining improperly melted may exhibit rebounding resulting in to poor deposition efficiency. Especially for cermets in which carbides are embedded in the metallic matrix, the size of carbide is crucial. Large carbides may fracture during impact whereas smaller carbide size may show decarburization which implies that optimized size is important for good coating formation. The morphology or shape is important from the point of view of flowability of the powder. Otherwise clogging of the feeder will be issue leading to increased deposition time.

Particle Flame Interaction: Besides the composition of the particle, the particle interaction with the flame depends on various factors like flame characteristics (physical dimension, thermal energy distribution) which is dependent on gas flows, gas flow ratios, nozzle dimension, barrel length, etc. All these factors affect the chemistry, heat transfer, kinematics and dynamics of the particle in the flame. Furthermore, particles are injected in the flame (radial or axial) with the help of carrier gas and it is expected that the carrier gas should not modify the flame characteristics. Hence, gases like argon or nitrogen having low enthalpy are used. As the particles are introduced in the flame, they will absorb the energy and melting process will start. However, the feed rate affects melting due to quenching the plume and with higher feed rate the heat energy is absorbed in the plume resulting into inefficient heating of the particles. This causes many particles to be in un-molten state. Low feed rate may result into overheating of particles and oxidation. Hence there is optimum feed rate where there is efficient transfer of energy to the particles and development of the coating. In addition to the flame particle interaction, the surrounding environment also plays critical role in the development of the coating microstructure. The inflight oxidation/ decarburization due to longer residence time, oxidizing atmosphere affects the particle chemical state and thereby the microstructure. This inflight chemical transformation should be avoided. Furthermore the flame stoichiometry like oxidizing or fuel rich flame affects particle heating and chemistry which ultimately affects microstructure. With fuel rich flame the flame length is longer which residence time in flame is increased and efficient heating of particle occurs. Extra fuel consumes surrounding oxygen which reduces oxidation of particles.

The trajectory of the particles in the flame is another important factor affecting coating formation. A proper trajectory enables efficient heat transfer to the particles. Particularly in APS the injection optimization is an important procedure to ensure efficient melting & melting state of the particles. If there is erosion of anode power dissipation may change and which can affect particle trajectory. In HVOF the injection is done in such a manner that the particles gets highly accelerated with narrow distribution of velocity so that most of the splats formed are flattened to same extent. The injection conditions must be stable for ensuring reproducible coatings.

Coating Formation: Coating formation takes place on successive impingement of the semi-melted or melted particles on the substrate. As the particles collide with the substrate there is flattening of the particle, bonding with substrate, rapid solidification and mechanical anchoring to the substrate. The coating formation will depend on substrate condition and particle state.

The substrate conditions which affect the coating build up include preheating, substrate hardness, substrate temperature, substrate roughness, substrate wettability, heat conduction, plane projected to incoming particles, substrate oxide layer and cleanliness. For smooth surface, if the temperature is above critical preheating temperature disc shaped splats are formed and below the temperature results into fingering which reduces adhesion. Fingering can occur for cold substrate covered with organic materials. The flame temperature enables the removal of organic adsorbates or condensates. Depending on chemistry of the particles oxidation can occur on solidification. Oxidation of splats can reduce adhesion. Since the coating is built up of splat, interfaces, interconnected pores and voids are inherent in the microstructure. Many of the properties including electrical, mechanical, thermal and performance including wear, corrosion are dependent on the microstructure.

The particle state governing the splat formation involves momentum/ kinetic energy and temperature/thermal energy. Thermal energy gives the atoms of the particles energy to overcome the potential energy barrier and influences flowability during spreading of particles. As the particles impinge on the substrate kinetic energy is transformed in the plastic strain energy. Some part of kinetic energy goes in deforming the substrate. Generally it is accepted that the higher the particle energy, the higher the flattening of the particle, leading to better coating bonds and coating density. Most of the time during deposition of HVOF coatings there is no intermixing of the coating and substrate and no metallurgical bond is formed. Only mechanical anchorage enables the coating to stick to the substrate. However with plasma spray intermetallic compound formatted has been reported which is due to melting of substrate by the impinging particles. Metallurgical bonding improves adhesion of the coating with the substrate and coating rupture can be minimized under adverse tribological conditions.

By controlling the particle state and substrate condition properties and performance of the coatings can be controlled. The control of the particle state is carried during the feedstock introduction and particle flame interaction.

Post Coating Treatments: Post TS coating treatments are necessary for wear and corrosion performance applications. As- sprayed coatings have appreciable surface roughness and porosity to a certain extent. Surface roughness is one of the important factors influencing wear behave coatings are polished to reduce the roughness. Furthermore, the coatings are grinded to establish required precise dimension required by applications in piston valves, gears, etc. Better corrosion performance demands low interconnected porosity. Sealants are sometimes used in conjunction with surface grinding and polishing to mitigate corrosion. Many engineering applications require low residual stresses which affect coating adhesion with the substrate. Heat treatment like annealing is done in open atmosphere or vacuum to relieve the stresses.

Thermal Spray Processing & Systems

From the initial development of thermal spray system by the Swiss scientist Dr. Max Schoop, there had been tremendous developments in the thermal spray technology in terms of reliability and reproducibility. With the latest development materials in metallic, non-metallic can be deposited. Thermal and kinetic energy of the flame is controlled by fuel/oxygen ratio or by electric power. Since, the coating is built up due to flattening of the particles impinging on the substrate, velocity plays dominant role in controlling the density of the coatings. Temperature is also an important variable which is necessary to be controlled depending on the particle. Ceramics particles require high temperature for deposition and plasma spray is suitable for ceramic particle deposition, whereas for deposition of cermets and metallic coatings low temperature system like HVOF or cold spray are suitable. Figure 1.17 shows the temperature and velocity for different TS deposition systems [27].

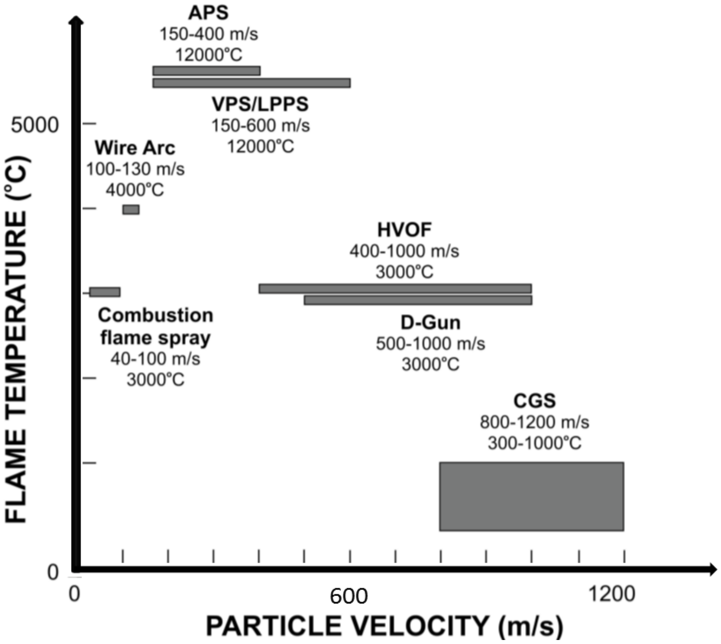

Figure 1.17: Typical temperature of flame and particle velocity of various TS systems [27].

TS coatings are increasingly used for corrosion and wear applications which demand low porosity, good adhesion and low coating degradation during deposition. For this reason HVOF is gaining momentum. In HVOF the flame is sustained by using mixture of oxygen and fuels like hydrogen, propylene, kerosene, propane, natural gas, acetylene or ethylene. The special design of nozzle enables ejection of gas at supersonic speed. Due to high velocity the residence time in flame is small. The attractive feature of HVOF is in their ability to produce dense coating with low oxidation, low porosity (<5%), chemical decomposition, phase transformation. In HVOF, fuel and oxygen is mixed in the combustion chamber where powder is introduced axially or radially. Due to exothermic reaction high temperature and pressure is produced and gas flows through nozzle with supersonic speed. The powder is heated in the combustion chamber and in the flame which results into molten or semi molten state.

Over the years, HVOF systems have been developed with different design and power capacity. All HVOF systems are based on same fundamental principle mentioned above. Till date based on design, control of temperature and pressure there are three generations of HVOF systems. The first generation of HVOF has large combustion chamber and straight nozzle. With this design velocities upto 1 Mach is possible. Second generation systems have ***De- Laval nozzle*** (convergent- divergent) as shown in figure 1.18 [28]. With each successive generation, the power handling capacity, combustion chamber pressure has increased. In the third generation HVOF temperature and velocity can be independently controlled. Table 1.1 shows the differences between the different generations of HVOF systems.

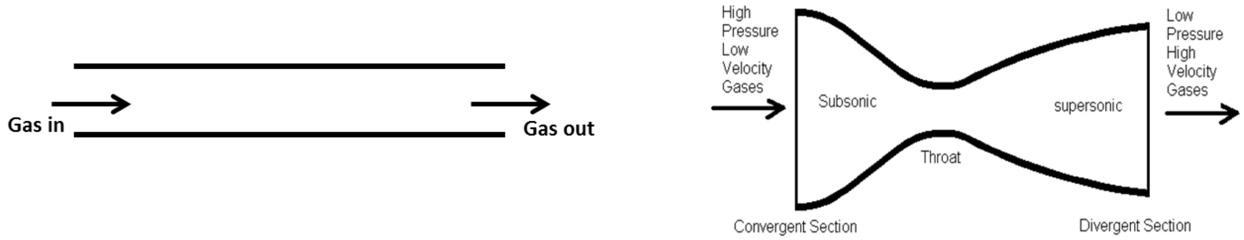

Straight Nozzle **De- Laval Nozzle**

Figure 1.18: Types of Nozzle used in HVOF systems [28].

Table 1.1: Differences between different generations of HVOF [27].

Generation	Nozzle type	Chamber Pressure (bar)	Power (kW)	Kg/hr of WCCo
First	Straight	3 - 5	80	2-6
Second	De-Laval	5-10	80-120	2-10
Third	De-Laval	8-25	100-300	10-12

1.4.2 Thermal Spray Gun Types

Over the years different guns have been designed with respect to powder injection in the flame and type of fuel. The following are the different guns in TS system:

1) Diamond Jet: In this gun mixture of fuel and oxygen is combusted in a central axial chamber. The powder is fed axially in the combusted gas with the help of carrier gas [26, 29]. This system was developed by Sulzer Metco Inc. Figure 1.19 shows the schematic of the gun.

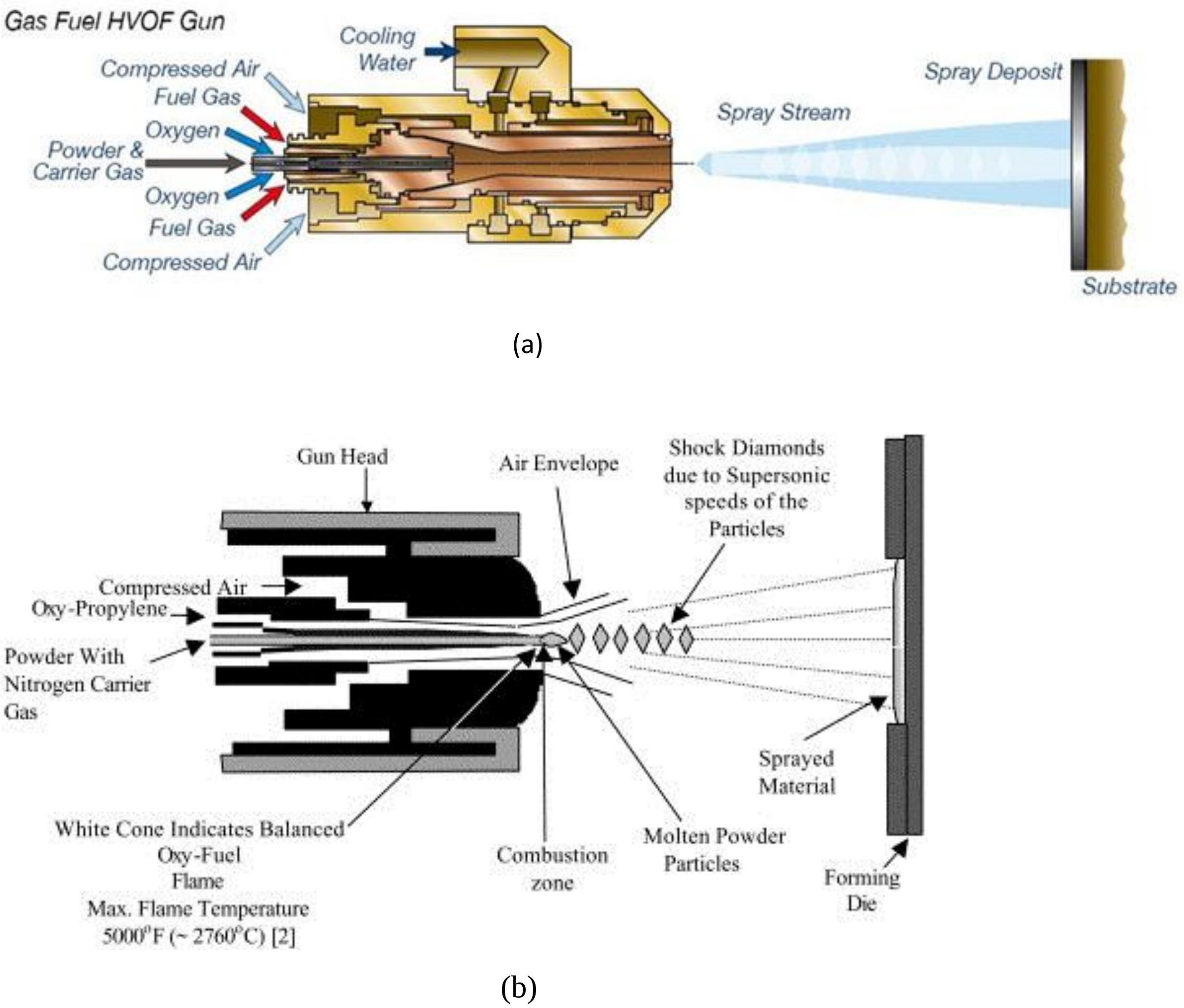

Figure 1.19: (a) and (b) are schematic cross sectional view of DJ HVOF gun [26, 29].

2) JP 5000: In this gun a mixture of fuel and oxygen is combusted in a chamber and the gas exits through the throat of the nozzle. Powder with the help of carrier gas is injected axially after the throat region. JP5000 was developed by TAFA-Praxair. Figure 1.20 shows the schematic of the gun [30].

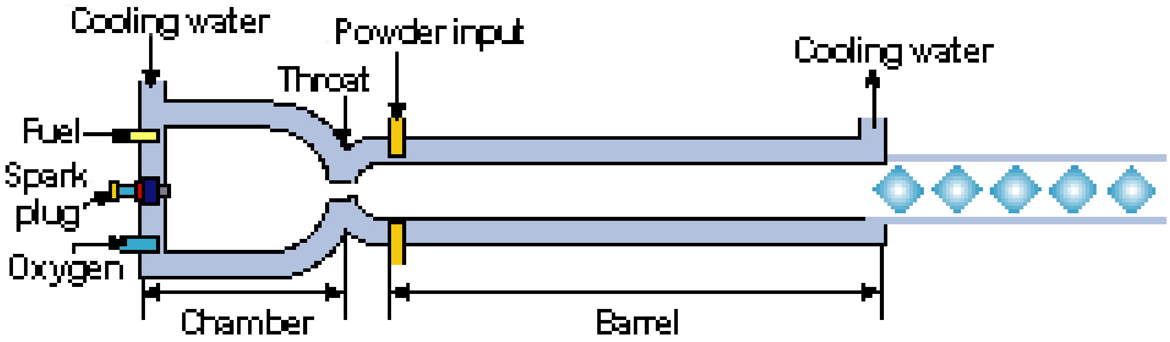

Figure 1.20: Cross section view of JP5000 HVOF gun schematic [30].

3) Jet Kote: In this gun a mixture of fuel and oxygen combusted in separate combustion chambers and leading to a mixing chamber where powder is injected axially. Jet Kote was developed by Deloro Stellite. Figure 1.21 shows the schematic of the gun [30].

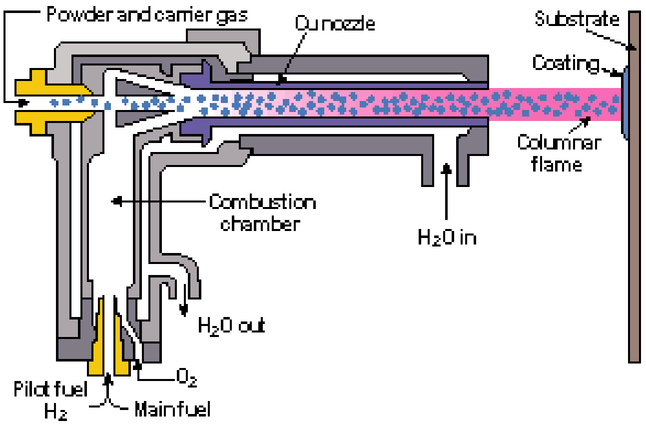

Figure 1.21: Cross –section view of Jet Kote HVOF schematic [30].

4) Top Gun: In this design of gun oxygen and fuel gas is brought in the mixing chamber and led to combustion chamber where the powder added to carrier gas is axially introduced from rear of the combustion chamber. This gun was developed by UTP , Schweißmaterial, Bad Krozingen, Germany. Figure 1.22 shows the schematic of the gun.

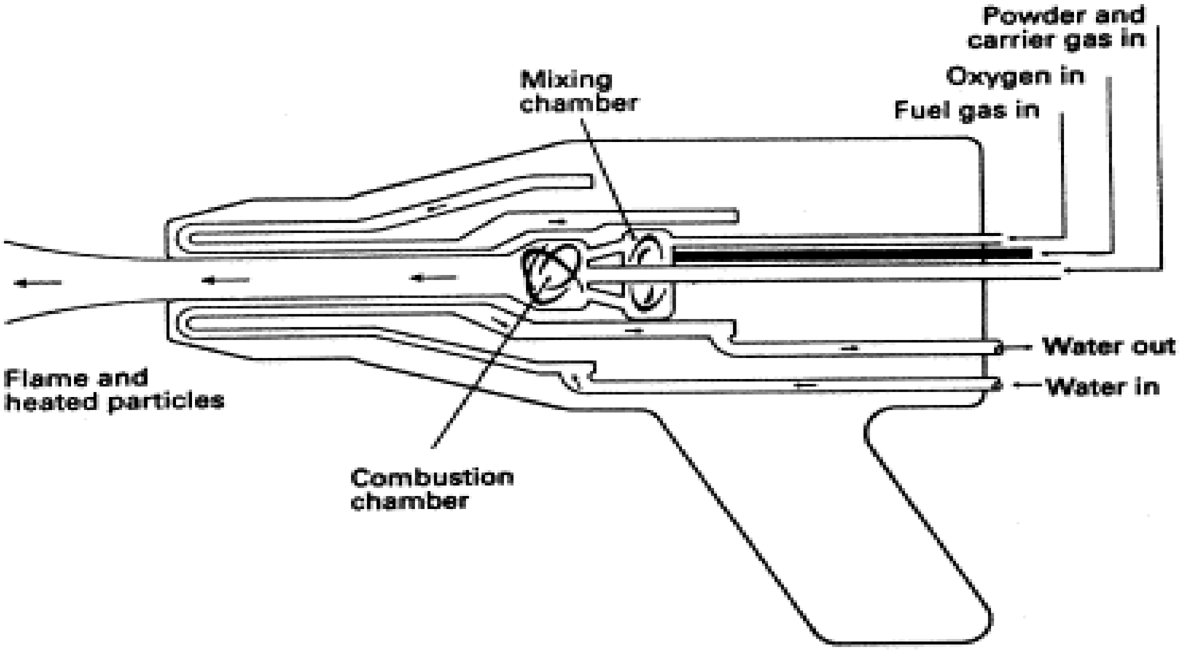

Figure 1.22: Cross section of TopGun HVOF schematic **[**31].

5) Detonation Gun: This gun consists of long water cooled barrel in which fuel and oxygen is introduced through inlet valves along with charge of particles. A controlled explosion of the mixture of fuel generally acetylene, oxygen by use of spark plug produces detonation or shock waves which melts the particles and propels them to the substrate. The enormous pressure closes the valves momentarily and once the pressure reduces the valves are again opened. Again the mixtures of gases are ignited and the cycle is repeated. In between each cycle nitrogen gas is used to purge the barrel. This gun was developed by Union Carbide Corporation. Figure 1.23 shows the schematic of the gun [32].

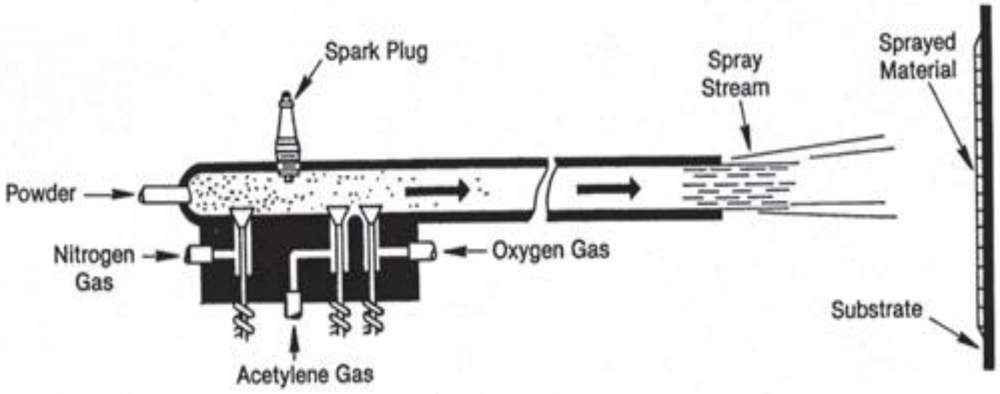

Figure 1.23: Schematic of Detonation gun [32].

6) Carbide jet: This is third generation gun was developed for spraying carbides and has independent control of temperature and velocity of the particles. The jet temperature is controlled by combination of kerosene and oxygen, while jet velocity is controlled by oxygen-hydrogen mixture. The design of CJ's gun consists of small combustion chamber volume in the high pressure region specifically for combustion of hydrogen and oxygen. High velocity is obtained by controlled combustion of hydrogen gas. The kerosene is burnt in another section of combustion chamber where the gas reaches supersonic velocity. To increase velocity hydrogen is combusted whereas to reduce temperature flow of kerosene is reduced. CJ's was developed by Thermico, Dortmund, Germany. Figure 1.24 shows the schematic of the gun [33].

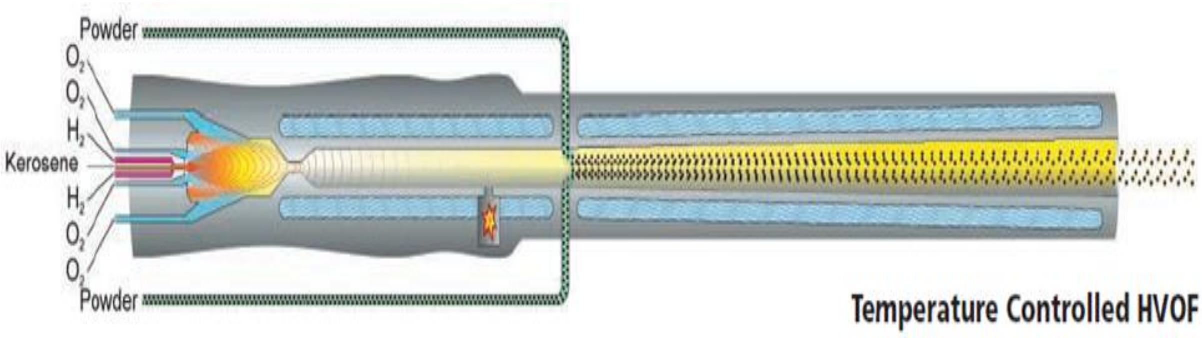

Figure 1.24: Schematic of carbide jet gun [33].

7) Cold Spray: It is a kinetic spray process which utilizes energy of supersonic jet of compressed gas particularly helium or nitrogen to accelerate particles to ultra- high velocities. The De-Laval nozzle is designed to achieve supersonic jet of the working gas. The particles impacting the substrate undergo plastic deformation and form coating on the substrate. Figure 1.25 shows the schematic of the gun [32].

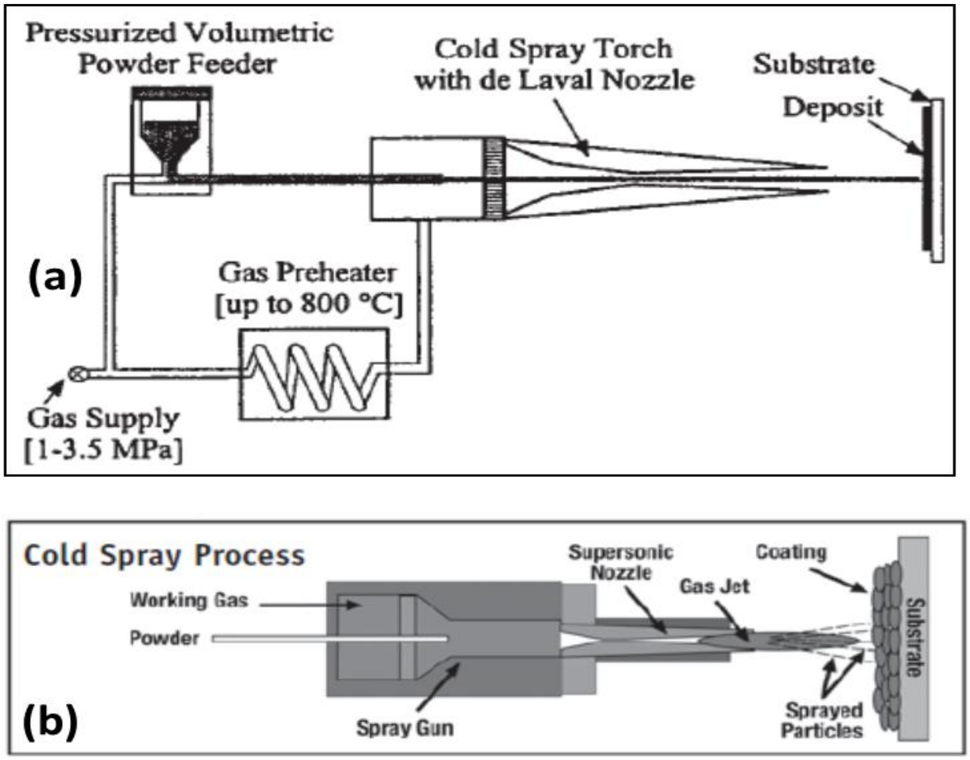

Figure 1.25: Schematic of cross sectional view of cold spray process [32].

8) **Atmospheric Plasma Spray (APS):** This system utilizes generation of plasma to melt the refractory particles and propelled to the substrate. APS gun in which electric arc is stabilized between tungsten cathode and water cooled copper anode. The Arc gas flowing in the gun maintains the plasma. Powder along with carrier gas is externally injected as shown in figure 1.26. In some APS guns three cathodes as shown in figure 1.27 are present like the one manufactured by Sulzer Metco and consequently has been named Triplex. Due to the presence of three cathodes deposition rate increases three times the conventional one- cathode APS. Cathodes are separately powered. The arcs remain axial due to presence of counter insulated neautrodes and tangential stability is maintained due to repulsion between the arcs. This configuration of the arcs ensures stability of the plasma [34].

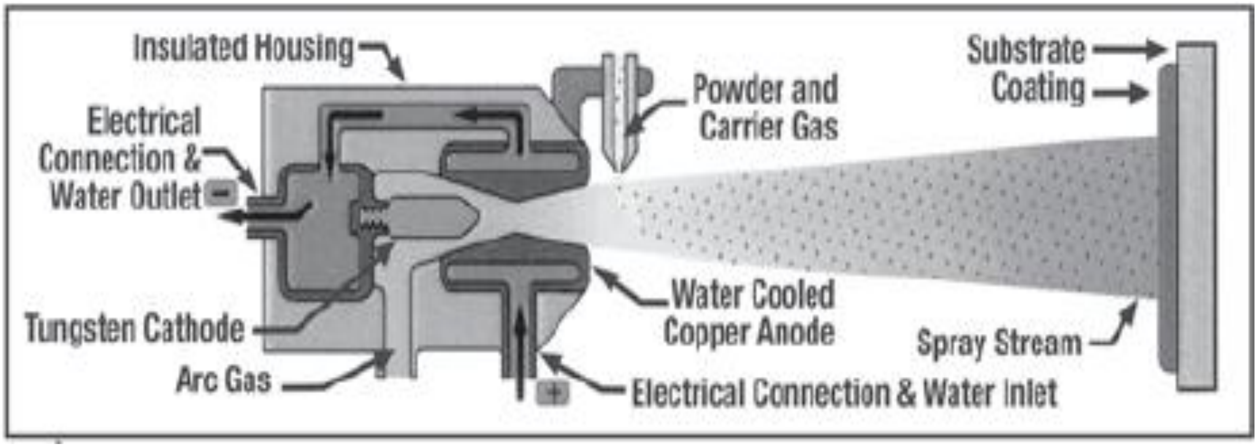

Figure 1.26: Schematic of cross sectional view of APS gun [33].

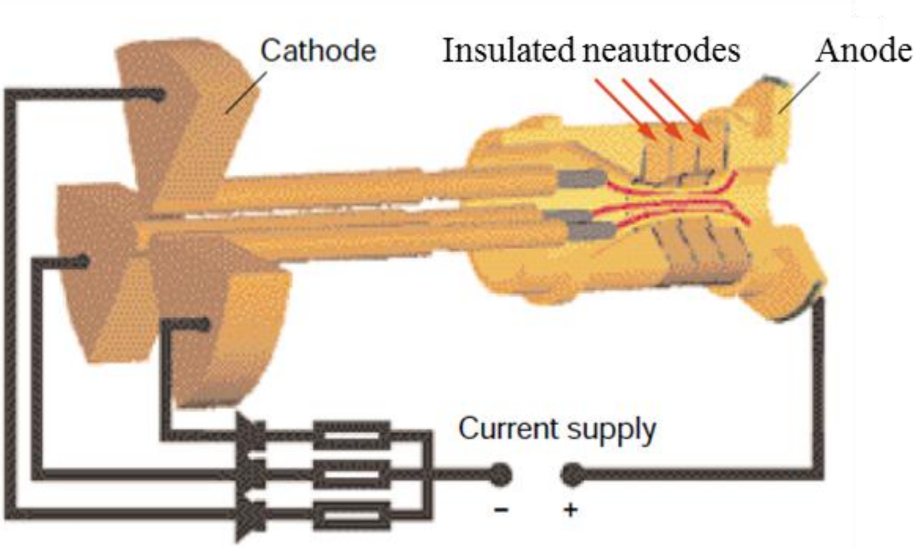

Figure 1.27: The Sulzer Metco Triplex system showing three cathodes [34]

In table 1.2, typical characteristics of the different thermal spray gun has been tabulated. Depending on application, choices are made to select a process.

Table 1.2: Details of the different types of thermal spray guns [27].

Thermal Spray	Manufacturer	Gases/Fuel	Powder feeding		Temperature	Velocity	Features
			Radial	Axial			
APS-Triplex	Sulzer Metco Inc.	Ar, N_2, He, H_2, Ar/H_2, Ar/He, N_2/H_2	External		20,000K	488 m/s	Three cathodes
Diamond Jet	Sulzer Metco Inc.	O_2, Air, H_2, C_3H_6, C_3H_8		In combustion chamber	1200 C-1900C	400-1000 m/s	De-Laval
JP 5000	TAFA-Praxair	Kerosene, O_2	In the barrel				
Jet Kote	Deloro Stellite	O_2/ H_2, C_3H_6, C_3H_8, CH_4, C_2H_2		In combustion chamber			Straight barrel
Top Gun	Miller Thermal/ UTP	C_3H_8, O_2, H_2, C_3H_6					
D-Gun	Praxair Surface Technologies	O_2, C_2H_2, N2, Ar, C_2H_2, C_3H_6		In combustion chamber			Straight barrel
Carbide Jet	Thermico Inc	H_2, N_2, kerosene, O_2	In the barrel		~800 C- 1800 C	500-1000 m/s	Independent T and V control
Cold Spray		He, N_2		In combustion chamber	600 C	550-1200 m/s	
CH_4- Methane, C_2H_2- Acetylene, C_3H_6- Propylene, C_3H_8- Propane							

1.5 Summary

In the present chapter, phenomenon of corrosion and corrosion mitigation by different technologies has been described. Thermal spray technology as a novel alternate technology with the view to coat large area and thick coating has been described. Various stages involved during the thermal spray process are discussed along with different thermal spray process. Thermal spray involves large number of variables which interact with each other and influence the coating properties and performances. The present dissertation will contain the motivation to pursue electrochemical studies on different thermally sprayed materials. Also, the effect of processing like feed rate, particle state on corrosion performance of the coatings will be discussed. As mentioned earlier for actual application of coating reliability is one of the important factors. In this connection variability of corrosion potential is an important criterion which has not been stressed much in the literature. Variability of the coatings will be discussed in relation to microstructure and processing parameters.

Chapter 2

Statement of the Problem

2.1 Introduction

In this chapter, the global problem of the long used electroplated chromium for corrosion and wear resistance application is critically discussed from technological and environmental perspectives providing the impetus to seek for alternative solution. As an alternative technology-thermal spray has been recognized. Understanding how processing parameters affect the corrosion performances is important in validation of the process for chrome replacement.

2.2 Chromium Electroplating and Problem with Cr

Electrochemical hard chrome is deposited from chromic acid solutions which contain sulphates, chromates, fluorides and carbonates. The substrates is made the cathode and Pb-Sn is used as anode which is insoluble in the solution [35].

EHC under normal condition has micro cracks as shown in figure 2.1. As the coating develops layer by layer cracks are partially bridged and new cracks develop. However the microcracks don’t line up and are randomized. In general about 0.00015 inches of the coating is sufficient for complete randomization of the path. Also, sometimes in addition to microcracks there are macrocracks which are rare but when present are long, running from top till the interface and can affect corrosion performances [35].

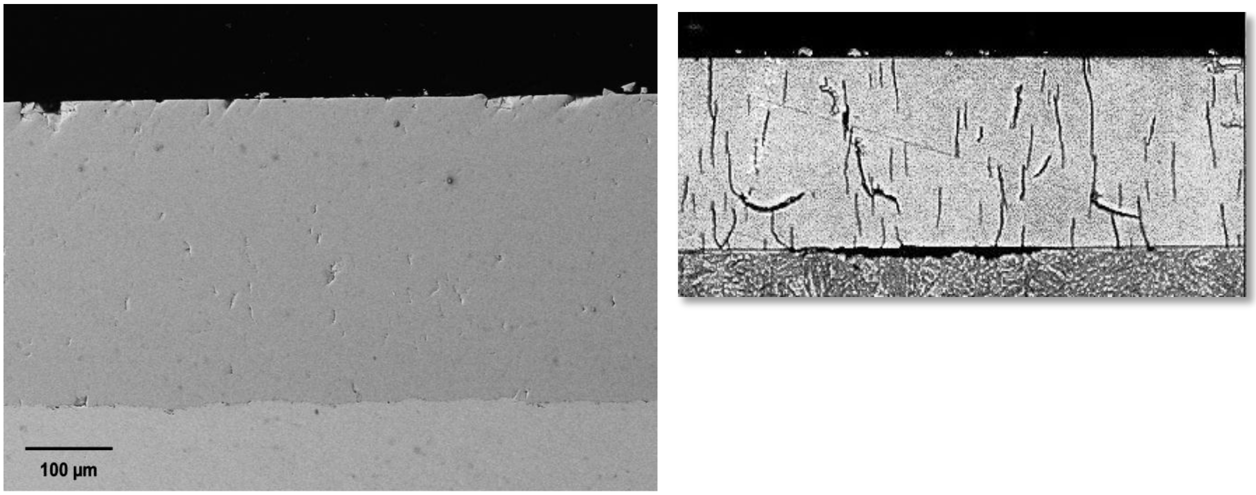

(a) (b)

Figure 2.1: SEM image of electroplated hard chromium on steel. Microcracks are visible throughout the microstructure. Figure a shows micro cracks but are discontinuous whereas figure b shows the macro cracks running across the coating [36].

In the recent years, the drive for hexavalent chromium (hex-Cr) replacement is going on every part of the world for environmental protection. Trivalent Cr [Cr^{3+}] is essential to human body for metabolic activities like glucose and lipid metabolism. In contrast, hex- Cr is *highly carcinogenic* to the human body and is known to cause varieties of ailments in living being like acute and chronic toxicity, kidney failure, genotoxicity like DNA lesions, DNA strand break, DNA inter-strand cross links, DNA protein crosslinks [37], lung cancer, chronic ulcers, skin irritation, respiratory tract irritation [38], nasal septum perforation [39].

Apart from environmental issues with EHC, the interest to seek alternative technologies is due to technological problems associated with EHC. There are various reasons to seek Cr replacement as discussed below.

EHC requires lengthy processing time because Cr plating is a slow process and the deposition rate is 0.001 inches/hr. For deposition of a defect-free, thick coating it is necessary to maintain the processing parameters constant for long time which is difficult task.

EHC provides inconsistent corrosion protection. This property is attributed to the macrocracks and microcracks, defects that expose substrate, flaking, nodule formation, etc.

These defects depend on various factors like pre cleaning, pre-plating, temperature, bath chemistry and current density. These process details differ from one plating house to another and in the same house due to process change to lower cost.

Thus, the technological and biological concern with the use of hexavalent Cr necessitates seeking alternative solution. It is necessary to replace hex-Cr by more environmental friendly materials as soon as possible.

2.3 Alternatives to EHC

Over the recent years different technologies are being scrutinized and validated for EHC. Compared to chrome electroplating, the HVOF process is clean, competitive and economical [41]. HVOF is very useful particularly to OEM, reclamation of worn out parts due to high deposition efficiency.

As an alternative to hexavalent chrome plating, thermally sprayed transition metals carbides (WC, TiC, Mo_2C, TaC, NbC, Cr_3C_2), hard oxides (Al_2O_3, TiO_2, Cr_2O_3), metals (W, Mo, Ti, Ta) and their alloys (NiCr, NiCoCr, AlY) are routinely used for simultaneous corrosion and wear resistance applications [42]. For the pure carbides of the transition metals, decarburization, oxidation, thermal decomposition or phase changes due to their high melting temperature can occur at elevated temperature. Instead of depositing pure carbides, the hard carbides are embedded in easily melted and ductile metals like Co, Cr, Ni or their mixtures [42, 43].

The combination of high hardness, wear and corrosion resistance of WC and the ductility, toughness, low melting temperature of Co makes the cermet WC/Co an attractive candidate to replace hex-Cr. Convincing experiments have been conducted to validate the use of WC/Co [44]. However, degradation of WC/Co during the deposition process is observed due to decarburization of WC, W_2C, complex Co-W-C and occurrence of metallic W. This degradation has a marked effect on wear and corrosion performance and is found to be greater in the coatings deposited by APS as compared to HVOF due to their inherent flame temperature characteristics [45].

The corrosion performance of WC/Co is quite complex due to interconnected pores leading to solution penetration to the substrate and direct attack [46]. Pore architecture is one of the influential factors in controlling corrosion and it is dependent on process parameters [47]. The interconnected porosity leads to galvanic coupling between the nobler coating to the substrate which acts as an anode in this situation [43, 46]. Furthermore, in WC/Co cermets under a corrosive environment particularly acidic or static saline medium Co shows preferential oxidation and dissolution in the electrolyte [43, 48, 49]. Also, investigators have reported the galvanic interaction between hard WC phase and Co where Co behaves anodically. Eventually, due to the removal of the binder near the carbide phase, the skeletal network of WC is exposed and can be removed during wear [48, 50].

To improve the corrosion and wear performance of cermet coatings apart from minimizing the pore interconnectivity, the corrosion performance of binder phase is of prime importance [48]. Consequently, many investigators have replaced Co in WC/Co with Co-Cr, Ni, NiCr, Co-Ni-Cr to investigate the corrosion résistance of the coating as a whole [49, 50]. Typically, Cr addition has a marked effect in reducing the corrosion current density by forming protective surface oxide which is predominantly Cr_2O_3 layer over the coating [49].

Thermal spraying is an economical, versatile, practical set of processing techniques for deposition of wide varieties of metallic, non-metallic coatings on different types of substrates in ambient, inert or vacuum conditions. It is extensively used in several industries like electronics, oil pipeline, gas and petroleum, defense, landing gears, aeronautical, medical implants, marine, automotive, etc. [51, 52]. TS coatings can have the ability to protect structural materials up to 20 years and have low maintenance costs [53].

2.4 Processing Effect on Corrosion Performance

Thermal spray has more than 50 parameters and is a highly stochastic process. The process parameters individually or in combination affect the microstructure of the TS coatings and their performance. Figure 2.2 shows the causal relationship between various parameters and the fundamental phenomena in the process of thermal spraying. The process parameters determine the flame-particles interactions which affect properties and performance of the coatings [54]. A. Vaidya et. al [55] have mentioned that particle temperature (T) and velocity (V) are the important key parameters amongst other parameters controlling the microstructure of the coating. The influence of T and V on microstructure can be seen in the coatings deposited by HVOF and APS. In APS, the plasma temperature is ~ 10000 K and particle velocity is ~50 m/s – 300 m/s. Due to the high temperature the particles are likely to get oxidized. In general, coatings by APS process are porous [56]. In comparison, the HVOF process produces coatings which have very low porosity due to the low peak process temperature ~ 3000 K and high velocity ~ 500 m/s to 800 m/s. Consequently, the splats flatten on impact to a higher degree than APS making the coatings denser [56] which provides better anti-corrosion performance [57].

The reliability of the TS coatings for anticorrosion application is of prime concern and subjected to investigation due to presence of various types of defects as mentioned in the previous section. The presence of interconnected pores in TS coatings plays an important role in corrosion performance. Due to this feature there can be galvanic corrosion between the coating that is more noble than the substrate. Furthermore, in the case of cermet coatings for wear and anticorrosion applications there can be galvanic coupling between the ceramic and metallic binder phase [58]. In addition, TS coatings have different level of oxide, which in general may enhance coating hardness, wear resistance, passivity and lubricity. However, excessive and continuous oxide networks can be deleterious hampering the corrosion performance of the coatings [57]. Due to oxide content in the coating, passivation is lowered [59]. Consequently, microstructure plays a very important role in the corrosion performance of TS coatings. The complex microstructure of TS is related to different variables like type of device, feedstock, process and deposition variables [55].

In addition to process parameters, it is worth understanding the effect of coating properties like porosity, thickness, surface roughness on corrosion performance and variability. Furthermore, it is interesting to study how corrosion performance relates to different properties. In the present thesis effect of different processing parameters like feed rate, temperature, velocity, guns, etc on corrosion performances of different thermally sprayed materials has been investigated.

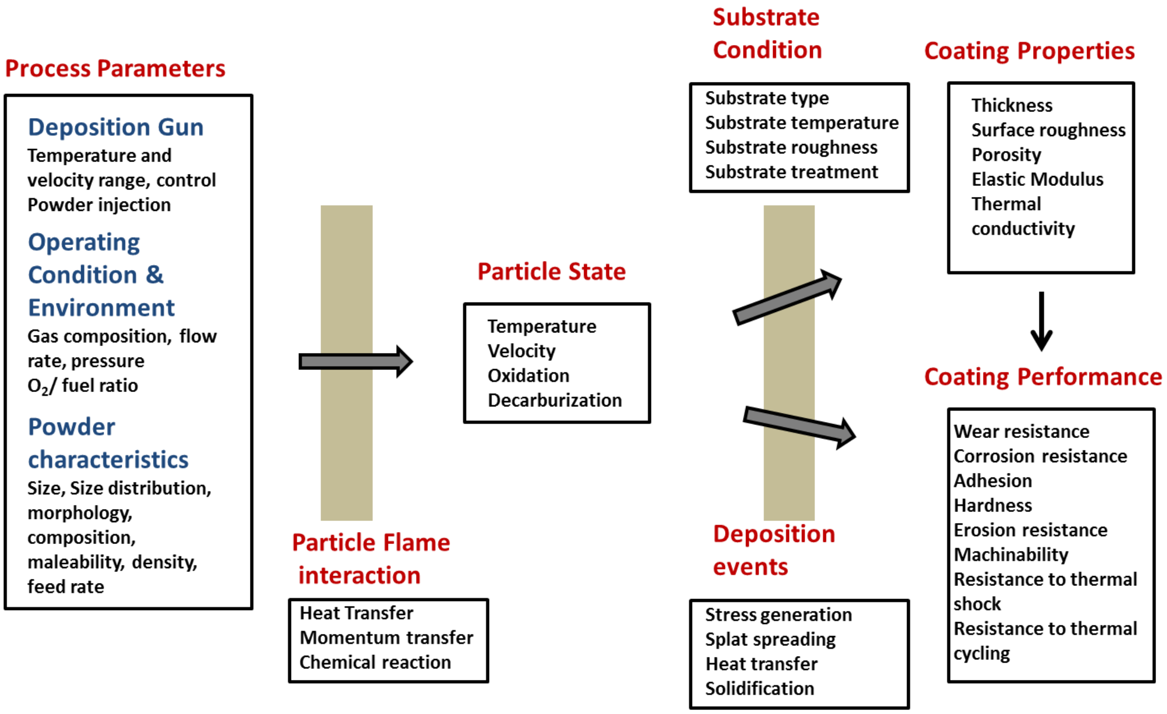

Figure 2.2: Cause- effect relation between various deposition parameters and physical phenomenon for thermal spray [54].

Chapter 3

Experimental Techniques

3.1 Introduction

In the present chapter different experimental techniques used for corrosion investigation aredescribed. The experimental techniques included substrate preparation, sample mounting for electrochemical experiments. For corrosion characterization of the coatings, a potentiostat was used. Also, the details of the electrochemical experiments and SEM are described.

3.2 Substrate Preparation for Thermal Spray

The thermally sprayed coatings were deposited on 1018 carbon steel substrate with dimensions of 223 mm x 25.4 mm x 1.4 mm. Prior to spray, all the substrate were cleaned by acetone and then grit blasted using 60 micron alumina grit with pressure of 55 – 60 psi.

3.3 Electrochemical Studies

Electrochemical studies were conducted using a Gamry 3000 potentiostat. Neutral NaCl with 3.5% by weight was prepared in deionized water. Prior to the electrochemical studies, samples were thoroughly washed in isopropyl alcohol in ultra sonic bath for 10 minutes. For each sample, a freshly prepared NaCl solution was prepared.

3.3.1 Open Circuit Potential (OCP) measurements were conducted on the bulk and electroplated nickel for 30- 45 minutes to allow the system to stabilize. However, for thermally sprayed samples of Ni, Ni-20%Cr and WC/Co, WC/Co-Cr, Cr_3C_2-NiCr OCP measurement was carried out for duration of ~ 10 hours.

3.3.2 Potentiodynamic (PD) measurements were carried at the rate 0.5 mV/sec and between -0.3 to 1 V with respect to the open circuit voltage. Standard saturated calomel electrode (SCE) was chosen as reference electrode. Here the sample area is 1 cm^2. Potentiodynamic measurements were conducted repeatedly at different parts of the sample to examine coating reproducibility. The experimental set up is shown in figure 3.1a. The set up consists of a glass cell capable to support three electrodes. The sample acts as working electrode, platinum mesh with surface area bigger than the working electrode is the counter electrode and the third electrode is the reference electrode. Controlled voltage is applied between the working and reference electrode with the help of potentiostat.

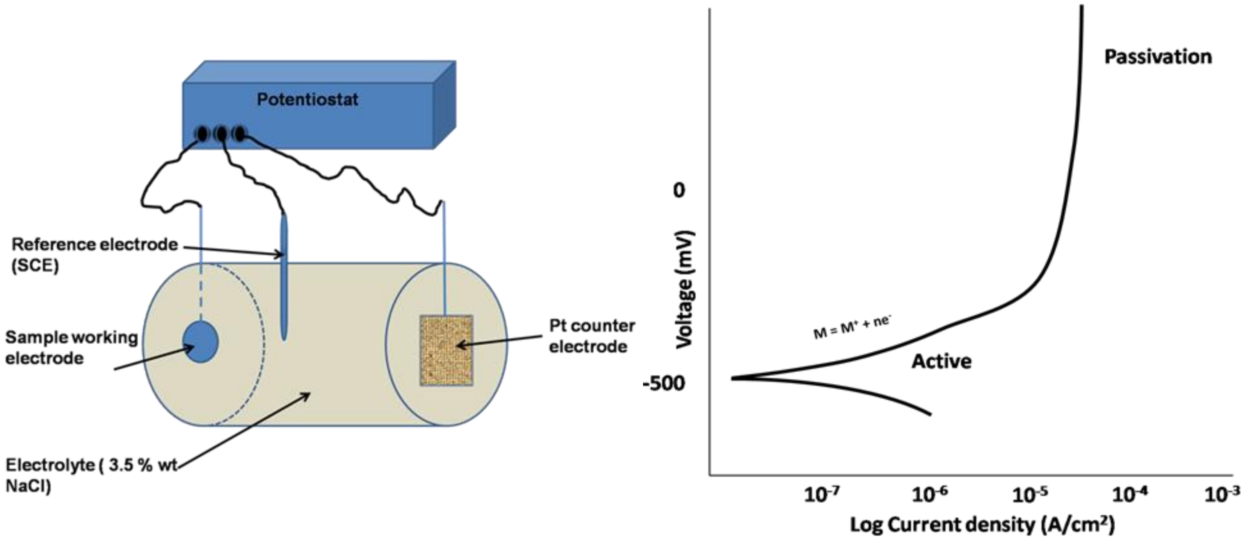

(a) (b)

Figure 3.1: (a) Schematic of the experimental set up for electrochemical studies of different samples. (b) Characteristic polarization curve from potentiodynamic experiment.

In a **potentiodynamic** experiment voltage is swept from negative to positive value between the working electrode and reference electrode. The response of the system in the form of current density is measured at each voltage. A characteristic curve is obtained for the corroding system as shown in Figure 3.1 b. As the voltage is made positive it is seen that the current decreases. At a characteristic voltage for a system called as corrosion potential negligible current flows through the circuit. Corrosion potential signifies the susceptibility of a metallic substrate to corrosion. As E_{corr} becomes more positive; the material is more resistant to corrosion. With further increase in voltage beyond corrosion potential the current starts increasing. This branch of the curve is the active region and signifies dissolution/ oxidation of the metal. Also it can be seen from Figure 3.1b that beyond certain potential the current remains constant. This current is known as passivation current. The passivation current signifies formation of passive layer protecting the surface from further corrosion.

The nature of the passive layer on metals was studied at great detail in 1960's and it was found that the passive layer is mostly oxide layer about nanometers in thickness. Figure 3.2 shows the dissolution behavior of Cr, Fe and Ni in H_2SO_4. Nanometer thick oxide layer called as passive film is formed in the voltage range of passivity whose thickness increase with increase in potential at the rate 1-3 nm/V. In the potential region of stable passive layer, small potential independent current flows through the anode and marks the dissolution current of the passive film. In the passive region, the potential between passive oxide film and solution is constant and independent of the anode potential [60].

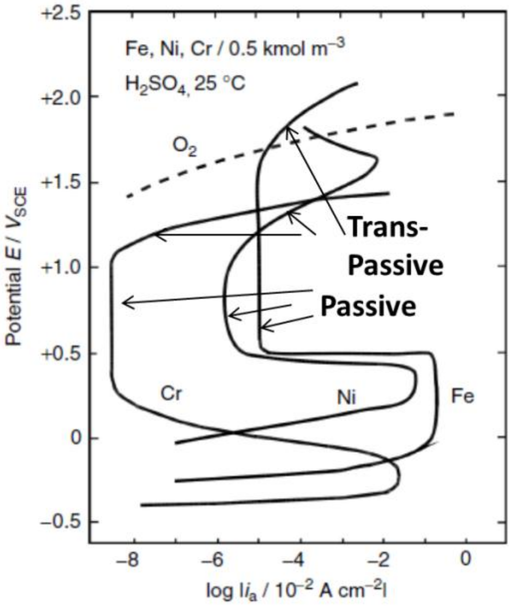

Figure 3.2: Tafel plot for anodic dissolution of Fe, Cr and Ni in 0.5 kmol/m^3 H_2SO_4. Dashed line shows the oxygen anodic dissolution current [60].

The passive film can breakdown in presence of aggressive ions such as Cl- in solutions. The localized breakdown of the film leads to infiltration of the electrolyte to the underlying metal and thereby promoting localized corrosion. In general, the breakdown of the film occurs after certain potential called as breakdown potential (E_b). After breakdown either repassivation or pitting may take place at the breakdown site. Figure 3.3 shows the different states of corrosion. It can be seen that pitting corrosion occurs after threshold potential called as pitting potential E_{pit}. Above pitting potential pits grow and below it pits ceases to grow. Pitting is insidious form of corrosion and leads to catastrophic failure of components. E_b and E_{pit} are influenced by Cl ion and H_2 concentration in the solution. Depending on relative magnitude of E_{pit} to E_b repassivation or pitting can occur. If E_{pit} is lesser (slightly cathodic) than E_b then pits will grow. Whereas if E_{pit} is higher than E_b then pits will cease to grow and repassivation will take place. At the pitting site chemistry is different leading to metallic dissolution.

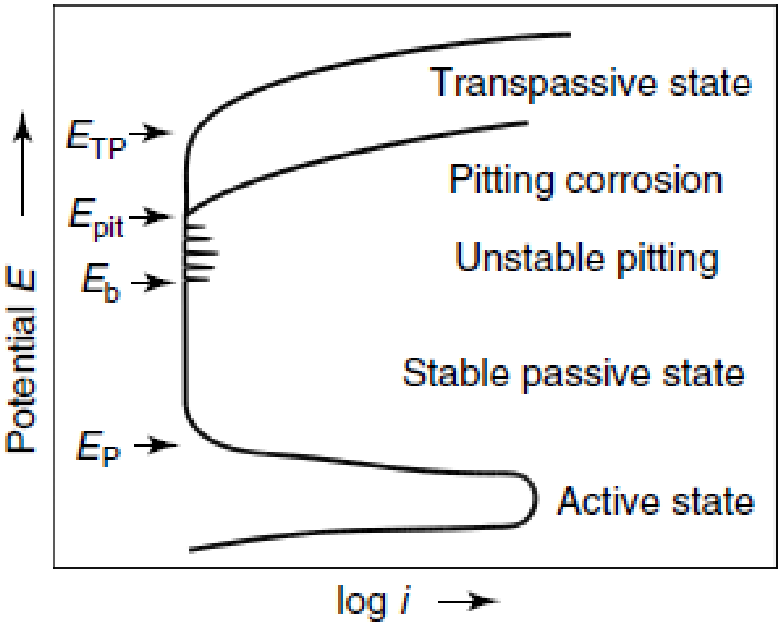

Figure 3.3: Schematic of potential vs current graph showing passivation potential (E_p), breakdown potential (E_b), pitting potential (E_{pit}) and transpassive potential (E_{tp}). For $E_b < E_{pit}$ breakdown sites repassivates, and for Eb>Epit, pitting corrosion proceeds [60].

The information about pit repassivation can be obtained from **cyclic polarization**. In this experiment potential is changed from negative to positive potential with respect to SCE similar to potentiodynamic experiment. However after certain positive voltage, potential direction is reversed. As the potential is reversed, a potential called re-passivation is reached where the pitting metal dissolution ceases to occur resulting into repassivation. Figure 3.4 shows the pitting and repassivation potential. For larger pits the pit repassivation potential is more negative relative to the pitting potential.

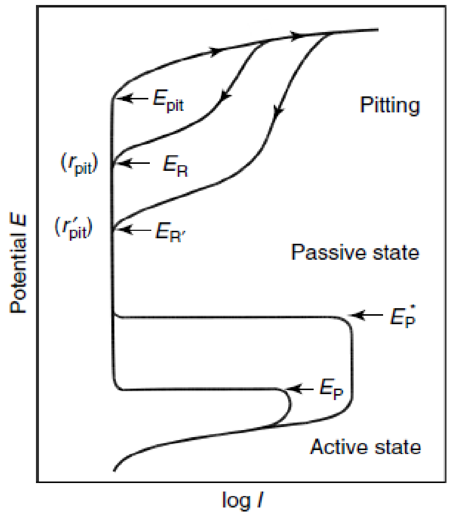

Figure 3.4: Schematic of cyclic polarization for metallic dissolution showing passivation – depassivation potential (E_p) outside pit, passivation –depassivation potential (E_p^*) for critical pit solution, pitting potential (E_{pit}), pit-repassivation potential (E_R), pit radium (r_{pit} and r'_{pit}); $r_{pit} < r'_{pit}$ [60].

NaCl is ubiquitous and is present in the dissolved state in sea water. As shown in Figure 3.5, carbon steel shows maximum corrosion rate around 3 wt. % NaCl solution which is coincidentally the sea and ocean water salt content [61]. At 3.5 wt.% oxygen is dissolved in maximum quantity. Also, previously described oxygen takes part in cathodic reaction. Hence, in the present investigation the corrosion experiments are conducted at 3.5% wt NaCl solution.

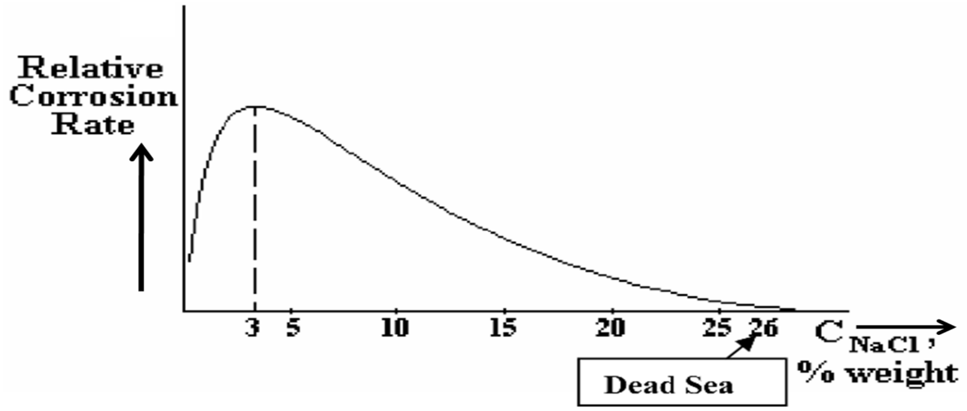

Figure 3.5: Variation of corrosion rate of carbon steel with the concentration of NaCl in water [61].

To investigate microstructural effects the samples were cut across the region where PD measurements were conducted. The samples were mounted in epoxy resin and were polished according to the standard procedure. Ni and NiCr samples were etched for about 30 minutes by glycergia [62]. Optical microscopy was used to determine as- sprayed and post- corrosion test microstructures.

3.3.3 IR compensation

Due to finite electrical resistance of the electrolyte, the potential differs from point to point in the solution. Whenever, voltage is applied between the working electrode and reference electrode some voltage difference exists near to the sample. The current flowing through the solution also contributes to the potential gradient. Furthermore, ions are concentrated near the sample as described in chapter 1 which adds to the potential drop. To reduce the error associated with the potential drop the reference electrode is placed close to the sample. However, the geometrical constraint due to finite size of the reference electrode, there is always some uncompensated resistance which leads to IR drop [63, 64].

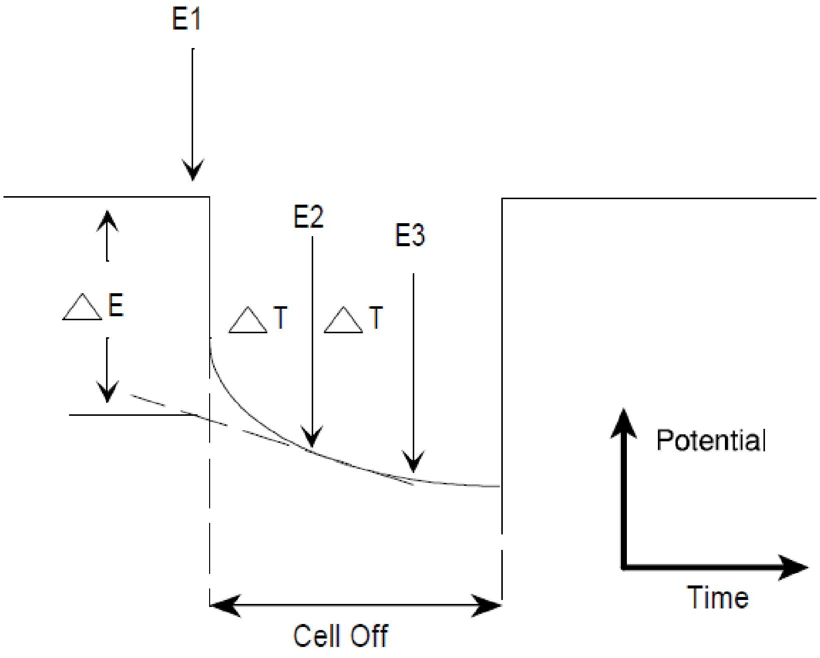

Figure 3.6: Concept of current interrupt method with graph of potential Vs time [64].

In the present potentiostat IR compensation is done by dynamic current interruption method as shown in figure 3.6. The uncompensated resistance is measured after each applied voltage level and applied to next voltage point. In this technique current is periodically turned off for a very short duration. As the current is in off state, IR drop vanishes. On the rapid time scale, potential drop remains constant. The difference in potential with the current in on and off state is a measure of the uncompensated IR drop. This instrument takes three potential reading at a ΔT time difference. The first measurement (E_1) is done just before the current is turned off and the rest two measurements (E_2 and E_3) are done in the current off state. With the help of E_2 and E_3 extrapolation is done backward in time when current is turned off to calculate the potential drop that would have been present without the uncompensated resistance. Thus, ΔE calculated is the uncompensated IR drop which is applied to correct the voltage that is to be applied at next point.

3.4 Scanning Electron Microscopy (SEM)

SEM is the most widely used technique to study surface morphology by electrons [65]. In this technique a beam of focused electrons raster scans the surface to be examined and the resulting signals include secondary electrons, backscattered electrons, x-rays, auger electrons, cathode luminescence.

With SEM there are two analytical possibilities:

1) The image of the surface involving secondary electron emission or backscattered electrons. The image further gives information about A) **Topography:** The surface features of an object or "how it looks", its texture; detectable features limited to a few nanometers and B) **Morphology:** The shape, size and arrangement of the particles making up the object that are lying on the surface of the sample or have been exposed by grinding or chemical etching; detectable features limited to a few nanometers

2) Identification of impurity generated during growth process involving the generation of x-rays.

A typical simplified schematic diagram of scanning electron microscope is shown in figure 3.7 [65, 66].It consists of an electron source emitting electron on the application of high voltage of order of ~10 to 30 kV. The electrons are focused by system of magnetic lenses to a very small diameter of approximately 10 nm or less. The current constituted by the electrons is very small of the order of 10^{-8} to 10^{-7} A. The whole instrument is operated under high vacuum condition to prevent the damage to electron source and losing electron due to interaction with gases in air. The electron beam scans the specimen in raster scan mode. SEM has high magnification of 50-300000 X and resolution up to 50 nm. Due to interaction of electron with the specimen various signals are emitted as shown in figure 3.8. A further simulation study [67] on the interaction of electron with specimen shows the interaction volume to be pear shaped as shown in figure 3.9.The origin of the pear shaped volume can be understood from ***elastic*** and ***inelastic*** scattering of electrons inside the sample. In elastic scattering the energy of an electron is unchanged but the direction is altered. The *Rutherford cross section* [67], Q, for elastic scattering is given as

$$Q= 1.62\times10^{-20}\frac{Z^2}{E^2}cot^2\frac{\emptyset_0}{2} \qquad 3.1$$

where Z is atomic number of specimen, E is the energy of electrons and $\emptyset_0$ is the scattering angle of the electron.

The inelastic scattering of the electrons in the specimen occurs due to varieties of phenomena like Plasmon excitation, excitation of conduction electrons leading to secondary electron emission, ionization of inner shells, generation of continuous x-ray, and excitation of phonons. Each of these events has its own specific cross section. The continuous energy loss due to all inelastic events is described by *Bethe relation* [67]. The energy loss per unit of distance (dE/dx) travelled in the solid is given as

$$\frac{dE}{dx} = -7.85 \times 10^4 (Z\rho / AE_m) \ln(1.66E / J) \quad \text{keV / cm} \qquad 3.2$$

where Z is atomic number, A is atomic weight (gm / mole), ρ is density (gm/cm^3), E_m is the mean electron energy (keV) along the path and J is the mean ionization potential (keV).

For a low atomic number specimen inelastic scattering is more probable than elastic scattering. Hence the electron initially have tendency for less lateral scattering and more penetration resulting in the neck of the pear shaped volume. As the electrons loose energy due to inelastic scattering, the cross section for elastic scattering as given by equation 3.1 increases for low energy. Due to increase in elastic scattering the lateral scattering increases and form the bulb region of the pear shaped volume. The depth and dimension of the pear shaped region is dependent on atomic number. For low Z materials the depth is more since inelastic scattering is more probable. In high Z materials the lateral scattering due to dominance in elastic scattering is more resulting in less penetration of the electrons. Consequently the pear shaped volume is small. With increase in beam energy of electrons, penetration increases and size of the interaction volume also increases.

To investigate microstructural effects by SEM samples were cut across the region where PD measurements were conducted. The samples were mounted in epoxy resin and were polished according to standard procedures mentioned in ASTM designation E3-01. Finally the cross-sectioned area for each sample was viewed using SEM of made Leo Zeiss open X 1550. SEM images were obtained with 19 kV accelerating voltage.

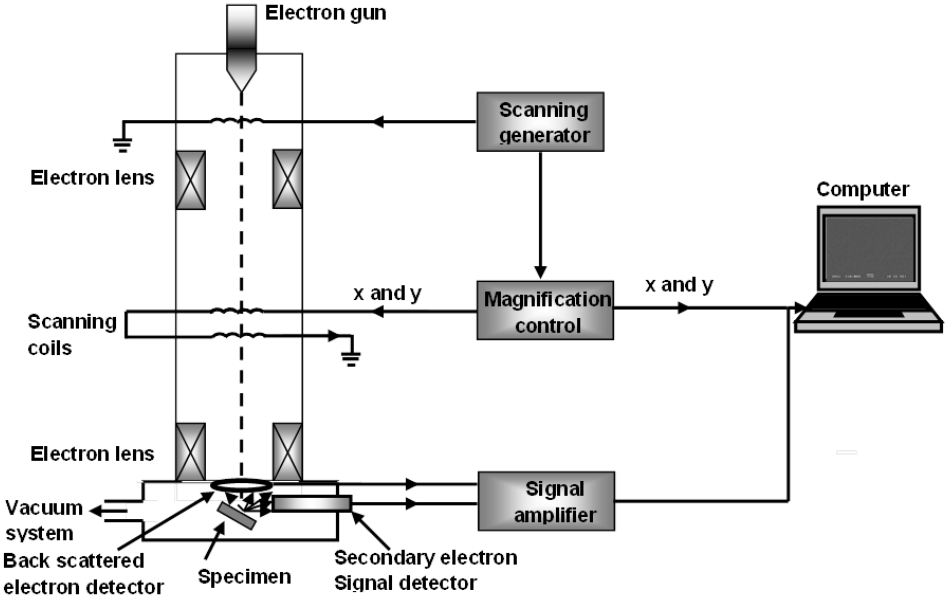

Figure 3.7: Schematic of SEM [Simplied from Ref. 65, 66]. Figure shows only two detectors i.e. back scattered and secondary electron detector.

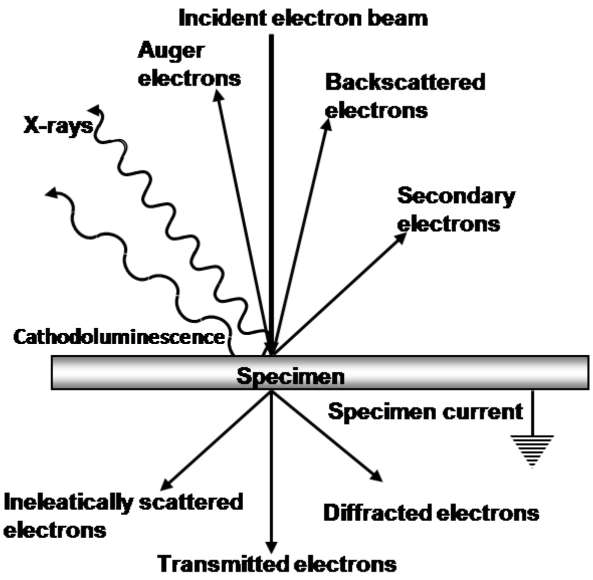

Figure 3.8: Interaction of electron beam with specimen [68].

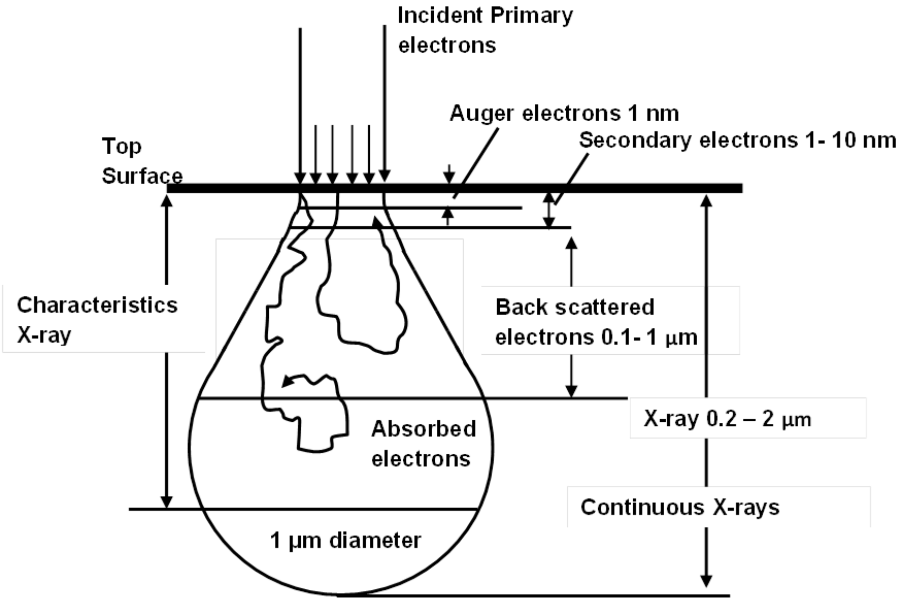

Figure 3.9: Types of electrons emitted due to electron beam interaction and region below the surface of specimen from which various signals are obtained [68].

Results and Discussion on

Electrochemical Studies of Thermal Sprayed Coatings

Chapter 4

Corrosion Studies of Bulk, Electroplated, Cold Spray, APS and HVOF Nickel

4.1 Introduction

In the present study nickel was chosen as a candidate to evaluate the influence of processing parameter because of its simple one element form. The information gained from such simple system is worth and lays a framework to better understand the corrosion behavior of complex thermal spray system like NiCr, cermets. With progresses and development of the HVOF systems many widespread applications will include Ni, NiCr and similar matrix in addition to WC-Co [69, 70]. Consequently, understanding the corrosion performance of the matrix is worth understanding [71]

4.2 Sample Description

Pure bulk nickel was obtained with 99.99% purity from McMaster Carr (Atlanta, Georgia, USA) and was used as a benchmark reference to compare corrosion performance. The thermally sprayed coatings were deposited on 1018 carbon steel substrates with dimensions of 223 mm x 25.4 mm x 1.4 mm. Prior to spraying, all substrates were cleaned by acetone and then grit blasted using 60 micron alumina grit with pressure of 55–60 psi . Ni coatings were deposited using HVOF Jetkote system (Deloro Stellite Group, Goshen, Indiana, USA) with the parameters given in Table 4.1 and table 4.2 with conditions designated as HVOF-A, HVOF-B and so on. Cold spray Ni was deposited using feedstock powder with size range below 25 µm. The gas temperature measured by Kinetics 3000 was around 550°C. The critical particle deposition as determined during cold spraying was determined to be 630-690 m/s. The detail of the experimental setup is described elsewhere [72]. The thickness of the cold sprayed coating was about 1 mm.

Table 4.1: Process parameters for HVOF JK Ni.

Torch Nozzle	**Gas flows**					**Spray Distance (inch)**
JK 9”1/4”	**Fuel SCFH**	**Oxygen SCFH**	**Carrier Air SCFH**	**Fuel/Oxy ratio**	**Total SCFH**	**7”**
	1250	**450**	**55**	**2.7**	**1755**	

Table 4.2: Process diagnostics parameters for HVOF JK Ni deposition.

Sample	**Description**	**σ_s(MPa)**	**T_s(C)**	**t_s(mm)**	**t_c(μm)**	**Passes**	**Feed rate (g/min)**	**Raster speed (mm/s)**	**V_p(m/sec)**	**T_p (c)**
HVOF-A	Low feed rate	-143	200	1.508	85	50	2	1000	683(8)	1381(24)
HVOF-B	Standard	-91	250	1.503	360	20	30	1000	651(4)	1594(13)
HVOF-C	High feed rate	-20	280	1.508	350	10	47	1000	628(4)	1576(14)
HVOF-D	Max. high feed rate	+18	300	1.503	662	14	58	1000	612(4)	1523(16)
HVOF-E	Max. Low Sub. Temp.	-99	200	1.506	331	20	30	1000	695(4)	1621(10)
HVOF-F	Med. Raster speed	-78	270	1.504	351	14	30	666	689(4)	1665(10)

σ_s-evolving stress; T_s –Substrate temperature; t_s- Substrate thickness; t_c- Coating thickness; T_p-Particle temperature ;V_p- Particle Velocity.

The APS-deposited Ni samples were obtained from a commercial source using proprietary conditions and are designated as APS-A, APS-B and so on. Cold spray Ni was deposited by accelerating Ni particles with nitrogen gas. For comparison, electroplated nickel coatings were produced using a Watts bath with nickel as the anode and 1018 carbon steel substrate as cathode. The electrolyte consisted of double salt of nickel (nickel (II) ammonium sulphate hexahydrate, 30 g in 500 ml distilled water). Nine volts were applied between the plates which were ~ 6 cm apart.

4.3 Results and Discussion

4.3.1 Electrochemical Studies of Bulk, Electroplated, APS, CS, HVOF Nickel

Open Circuit Potential Measurements

Figure 4.1 shows the open circuit potential (E_{oc}) measurements of bulk nickel, electroplated nickel, cold spray Ni and the carbon steel substrate. The samples were stabilized in approximately 30 minutes.

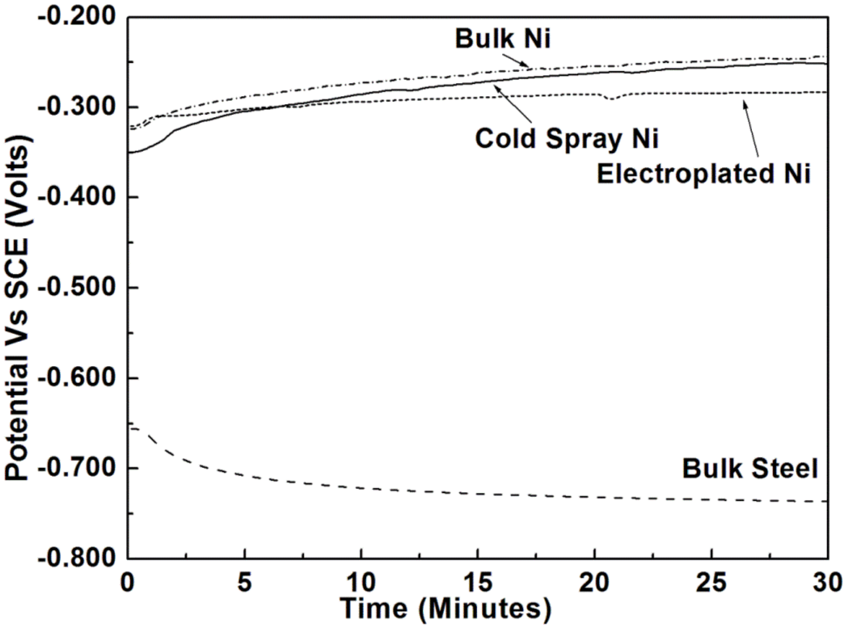

Figure 4.1: OCP results of Bulk Ni, cold spray, electroplated Ni, and carbon steel in static 3.5% neutral NaCl.

The E_{oc} of the bulk, cold spray and the electroplated Ni sample increase for a few initial minutes whereas for steel surface the E_{oc} decreases before stabilization. The E_{oc} for bulk Ni increases from -0.325V up to -0.250 V. The E_{oc} for electroplated Ni increases from -0.325 V up to -0.300 V and for cold spray Ni E_{oc} increases from -0.350 V up to -0.250 V. The increase in E_{oc}

for these samples may be attributed to the formation of nickel oxide in the aqueous medium similar to observations reported by Magnani et al. for an aluminum alloy system [73]. Also, Figure 4.1 shows that the E_{oc} for the steel substrate decreases from -0.650 V down to –0. 750 V which and may be due to attack of the Cl ions on the steel.

Figure 4.2 shows the open circuit potential (E_{oc}) measurement for the APS Ni commercial samples. A close observation of Figure 2.2 shows that the E_{oc} for all APS samples decreases over time. The E_{oc} for APS-A decreases from -0.410 V down to -0.525 V. The E_{oc} for APS- B, APS-C and APS-D show small change in the E_{oc} over the sampling time period.

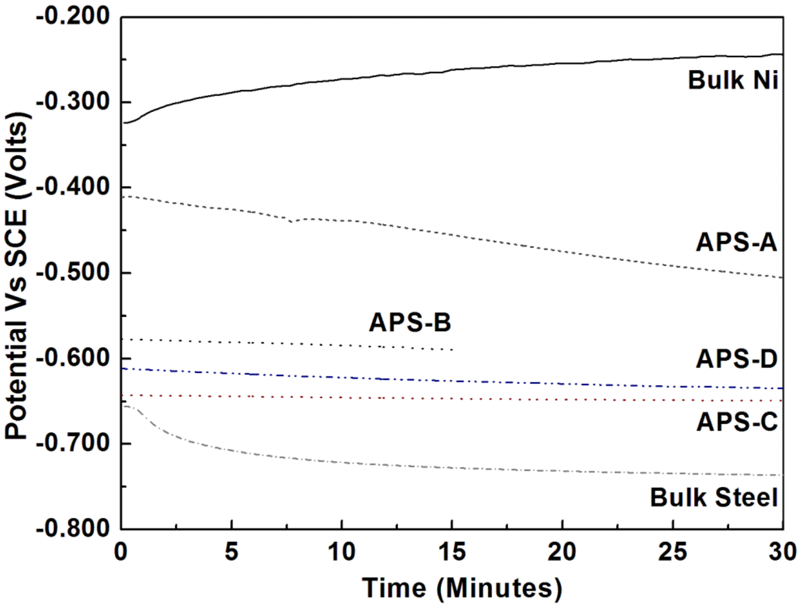

Figure 4.2: OCP results of bulk Ni, commercial sprayed APS Ni and steel substrate in static 3.5% neutral NaCl.

For APS- B, APS-C and APS-D the final E_{oc} attained are -0.588 V, -0.650 V and -0. 634 V, respectively. The E_{oc} for these samples are near to the E_{oc} for steel substrate which suggests that these samples have inter-connected porosity facilitating the passage of electrolyte to the steel substrate.

Figure 4.3 shows the open circuit potential measurement for the HVOF Ni samples. After an initial decrease in E_{oc}, the coatings are well stabilized after 12 hours. The E_{oc} for HVOF-A and HVOF-D is lower compared to the E_{oc} of the other HVOF samples. Compared to the APS, HVOF coatings take longer to stabilize suggesting that the electrolyte may have a tortuous path to through the coating.

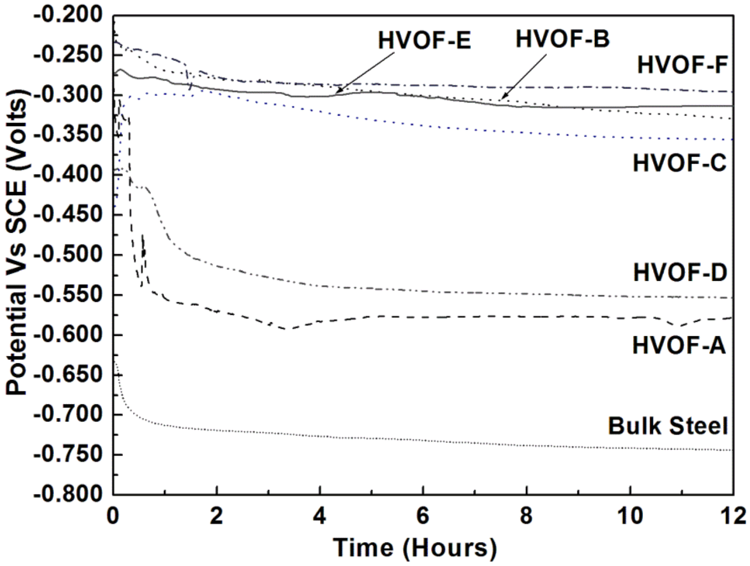

Figure 4.3: OCP scan for HVOF JK Ni coatings in static 3.5% neutral NaCl.

Potentiodynamic Measurements

Figure 4.4 shows the potentiodynamic scan performed on the bulk Ni, CS Ni, electroplated Ni and steel substrate. The E_{corr} for bulk Ni, CS Ni, electroplated Ni and steel substrate are -0.278 V,-0.308, -0.307 and -0.823 V, respectively. The E_{corr} for the electroplated Ni is at -0.307 V which is near to that of bulk Ni (-0.278 V). In terms of corrosion performance, the CS Ni sample showed similar behavior in the electrolyte as exhibited by bulk Ni. The E_{corr} of CS Ni (-0.308 V) is near to that of bulk Ni (-0.278 V). The excellent corrosion resistance behavior of CS is consistent with its dense microstructure and the presence of low porosity. Also, the corrosion current densities for bulk Ni, CS Ni and electroplated Ni are shifted towards lower values compared to the steel substrate which is indicative of lower corrosion rates for these samples. Also, it can be observed that CS sample shows kink in the tafel plot at ~0 V. This kink may be due to formation of oxide layer.

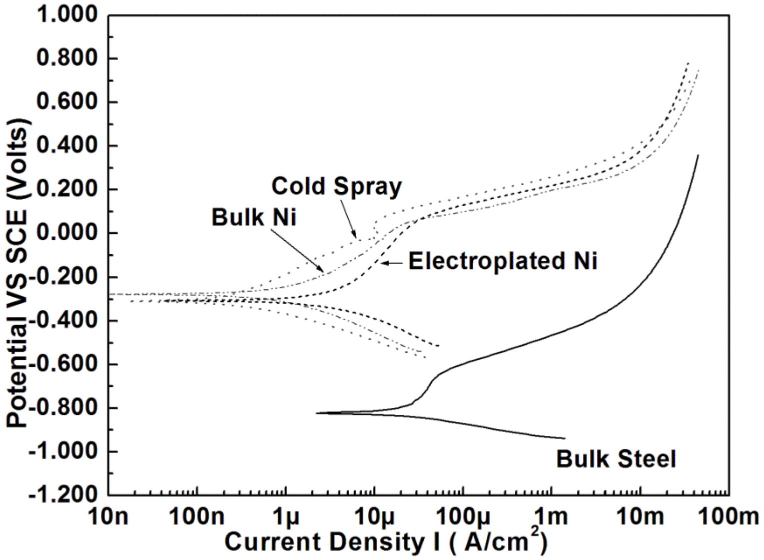

Figure 4.4: Potentiodynamic scan of bulk Ni, cold spray, electroplated Ni, and carbon steel in static 3.5% neutral NaCl.

In contrast to electroplated Ni and CS Ni, the E_{corr} for the APS samples are far below that of bulk Ni. From Figure 4.5 it can be seen that the E_{corr} for all samples except sample A are near to that of steel (E_{corr} = -0.823V). The low performance of these coatings suggests highly interconnected porosity present in the film which facilitates the easy passage for the electrolyte to the substrate. The trend in the performance of the samples under PD studies is similar to their OCP. Also it can be observed that the current in this coating increases monotonically for rise in voltage. The Tafel plot for the APS samples are shifted to the higher current density compared to bulk Ni which implies high corrosion rate and inefficacy of the APS coatings to protect the steel substrate from corrosion.

As shown in Figure 4.6 the HVOF coatings exhibit complex PD response with varied corrosion behavior in static 3.5% NaCl. The HVOF-A coating shows poor performance in the electrolyte. It has an E_{corr} near to that of steel substrate. Similarly, HVOF-D exhibits poor performance in the NaCl solution in contrast to the other HVOF coatings. Furthermore, it can be observed that the Tafel plot for HVOF-A and HVOF-B is shifted towards higher current density.

Also, these HVOF samples show kink at –0.100 V for HVOF-A and 0.100 V for HVOF-D showing that these samples are susceptible to pitting corrosion compared to the other HVOF coatings.

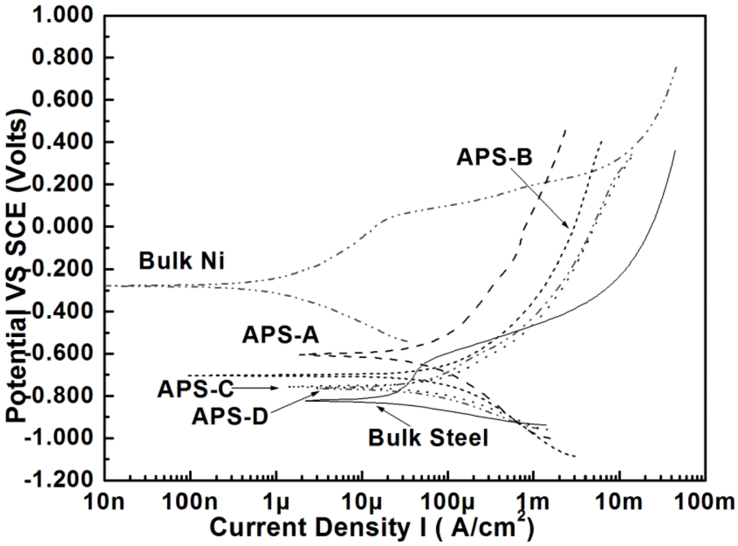

Figure 4.5: Potentiodynamic scan of bulk Ni, Commercial APS Ni and steel substrate in static 3.5% neutral NaCl.

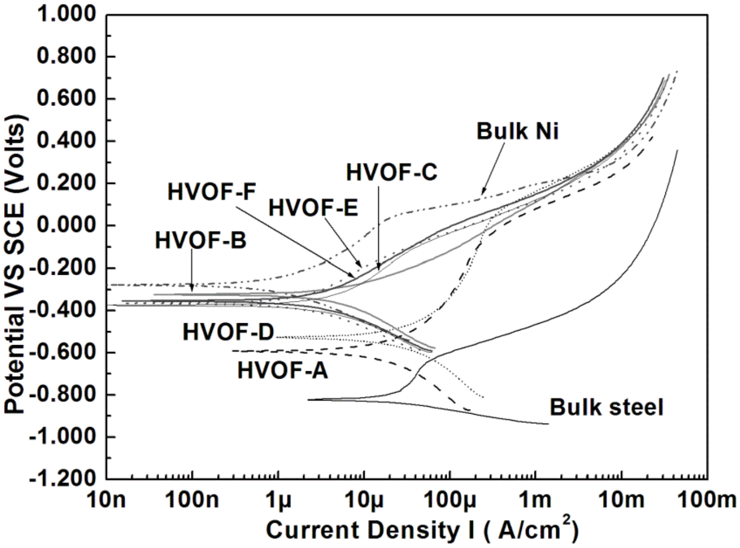

Figure 4.6: Potentiodynamic scan of HVOF JK Ni coatings in static 3.5% neutral NaCl.

Figure 4.7 shows the corrosion potential for each of the HVOF spray conditions investigated in this study along with the variability observed when potentiodynamic measurements were made on several locations on one sample. The coating HVOF-A shows greater variability compared to other coatings and has a wide spread in E_{corr}. The other samples show compact E_{corr} distributions. HVOF-A has the lowest thickness of 85 µm and low particle temperature (1381^{o}C). Furthermore, it was deposited with a low feed rate. Due to these conditions, a majority of the particles may be un-melted and the coating contains many interconnected pores. On the other hand, HVOF-B shows better corrosion performance with a compact distribution in E_{corr}. This sample has particle velocity of 659 m/sec and particle temperature 1594 ºC and due to this high temperature and velocity, the particles would be more molten leading to the formation of a dense coating. Furthermore, the coating has moderate thickness which may lead to a more tortuous path for the electrolyte to reach the substrate. The other coatings HVOF-C, HVOF-E, HVOF-F show better corrosion performance. Also, these coatings show lesser variability in E_{corr} compared to HVOF-A. From Table 1 it can be seen that these coatings have high particle velocity leading flattening of the splats to a large extent compared to HVOF-A. Due to this dense coating is formed and is described in next section.

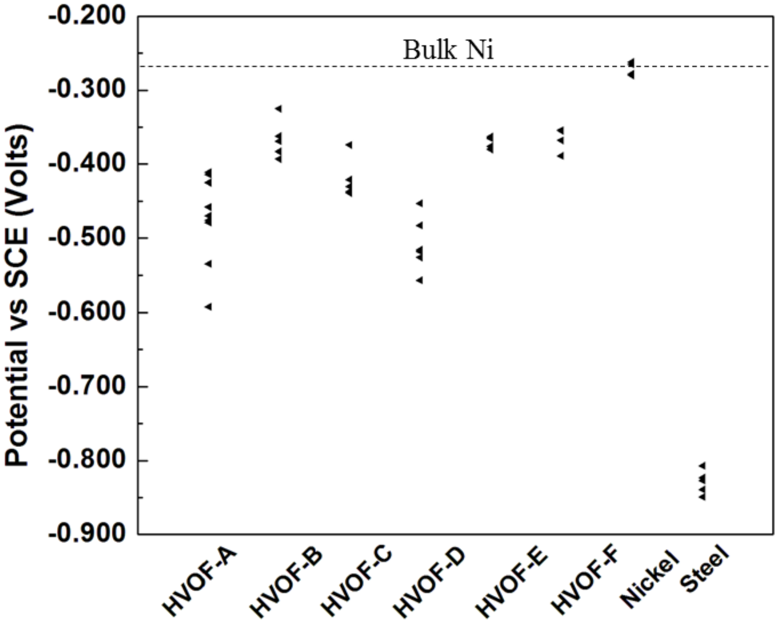

Figure 4.7: Variability in E_{corr} of the HVOF JK Ni in static 3.5 % neutral NaCl measured by potentiodynamic scan. Dotted line shows the Ecorr for bulk Ni.

4.3.2 Optical and Scanning Electron Microscopy

Figure 4.8 shows the microstructure for the etched cold spray Ni. Due to preferential etching the grain boundaries and inter-particle boundaries can be clearly observed. The microstructure is dense and deformations of the particles are clearly seen. Also, it can be seen that the inter-particle boundary is not continuous and smeared at many areas indicating the compactness of the coating. Due to the dense microstructure and thickness this coating showed corrosion potential close to bulk Ni.

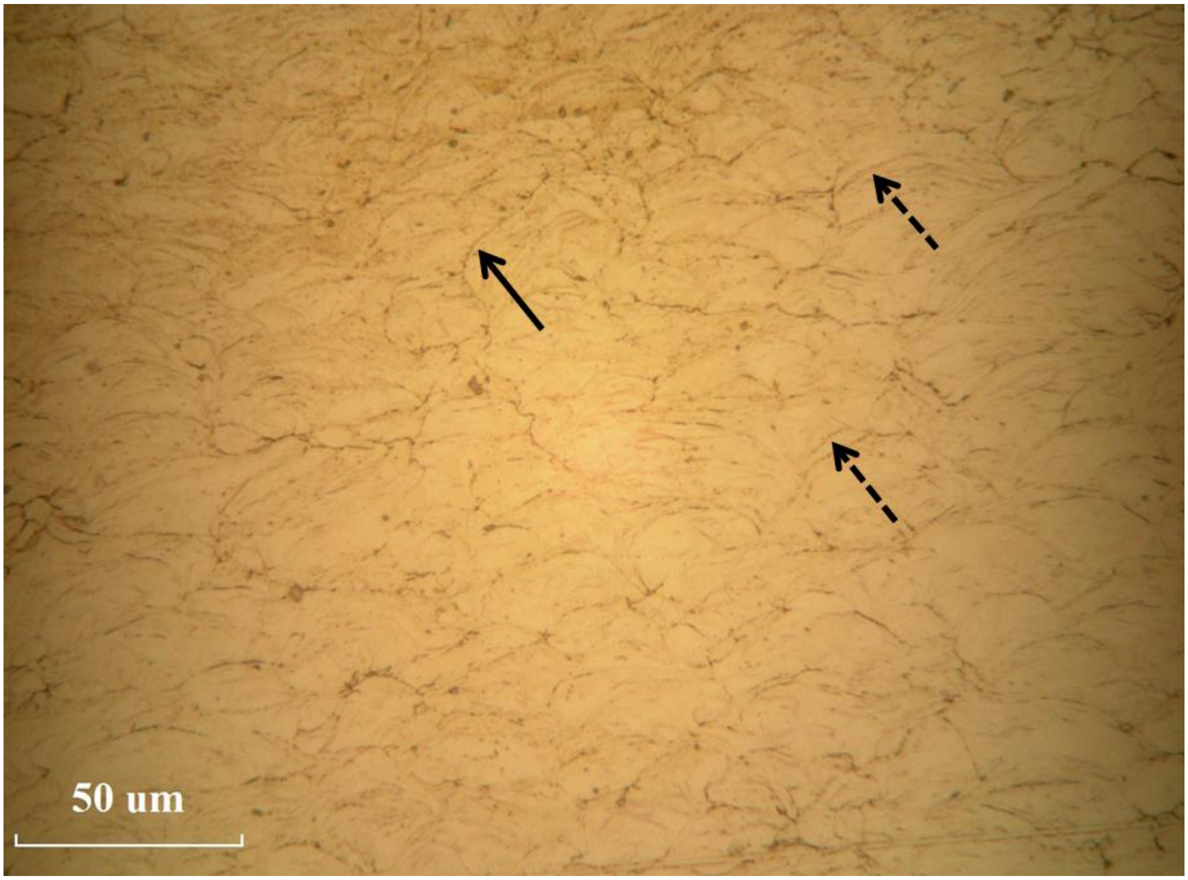

Figure 4.8: Cross- sectional optical micrograph for Glycelergia etched cold spray Ni. Continuous arrow indicates the inter-particle boundary whereas the dashed arrow indicates grain boundaries.

The surface image for the corroded APS samples shows the conspicuous corrosion as shown in figure 4.9. The cross-sectional optical micrographs for the corroded APS Ni samples are shown in Figure 4.10. The thickness of the coating from the different location is same and around ~95µm. The images show thick rust layers between coating and the substrate. Thus, the electrolyte in APS coating could reach the steel substrate and corrode it. These images support the observed E_{corr} for these coatings which are near the E_{corr} for steel substrate.

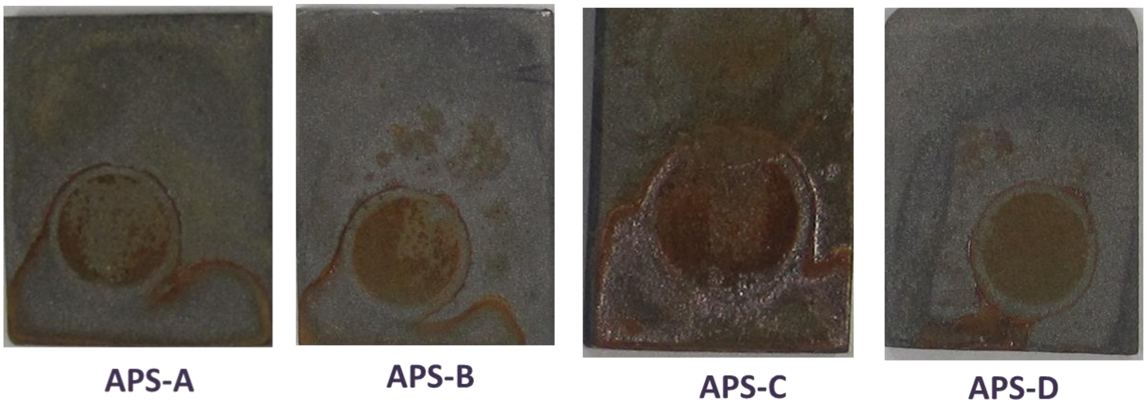

Figure 4.9: Surface image of the corroded APS samples. Corrosion is prominent at the test area.

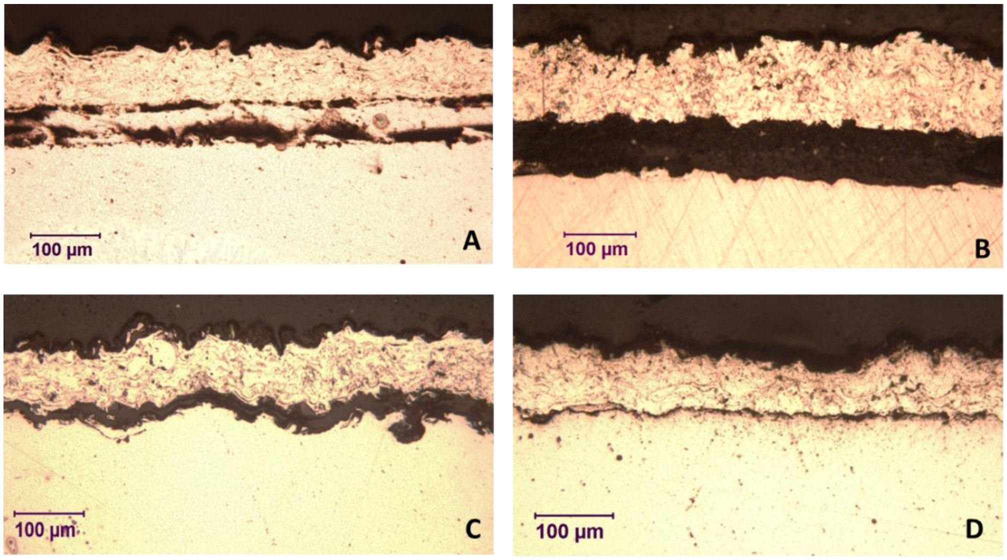

Figure 4.10: Cross- sectional optical micrograph for corroded commercial APS coating from different location.

Figure 4.11 shows the scanning electron micrographs for non-corroded HVOF Ni. HVOF-A is thin and has inhomogeneity which led to a wide variation in E_{corr}. In the corroded

HVOF-A coating as shown in figure 4.12, the pathways behaving as conduit for the electrolyte from the surface to substrate can be observed. Also, from figure of the corroded HVOF-A it can be observed that the bunching of electrolyte pathways shown inside the circles are not uniformly present throughout the microstructure and may be responsible for the wider variation in corrosion potential. In this coating the electrolyte pathways can be conspicuously observed to be continuously running across the coating. For this coating the successive passes with low feed rate of the particles were not enough to influence peening process which is one of the important factors causing densification of the coating especially near the interface with the substrate [74, 75]. The microstructure for other samples HVOF-B to HVOF-F are compact and uniform leading to reduced E_{corr} variation relative to HVOF-A. Furthermore, these coatings are thick and may have highly tortuous pore paths which delay the time for electrolyte to stabilize with the samples. For example, in HVOF-E and HVOF-F the microstructure is not uniform and there are regions in the coating which are relatively less dense especially near the surface as indicated by the circle. However, this coating is thick and has highly tortuous electrolyte path which are not continuous at many regions. Consequently, this coating has better corrosion performance compared to HVOF-A.

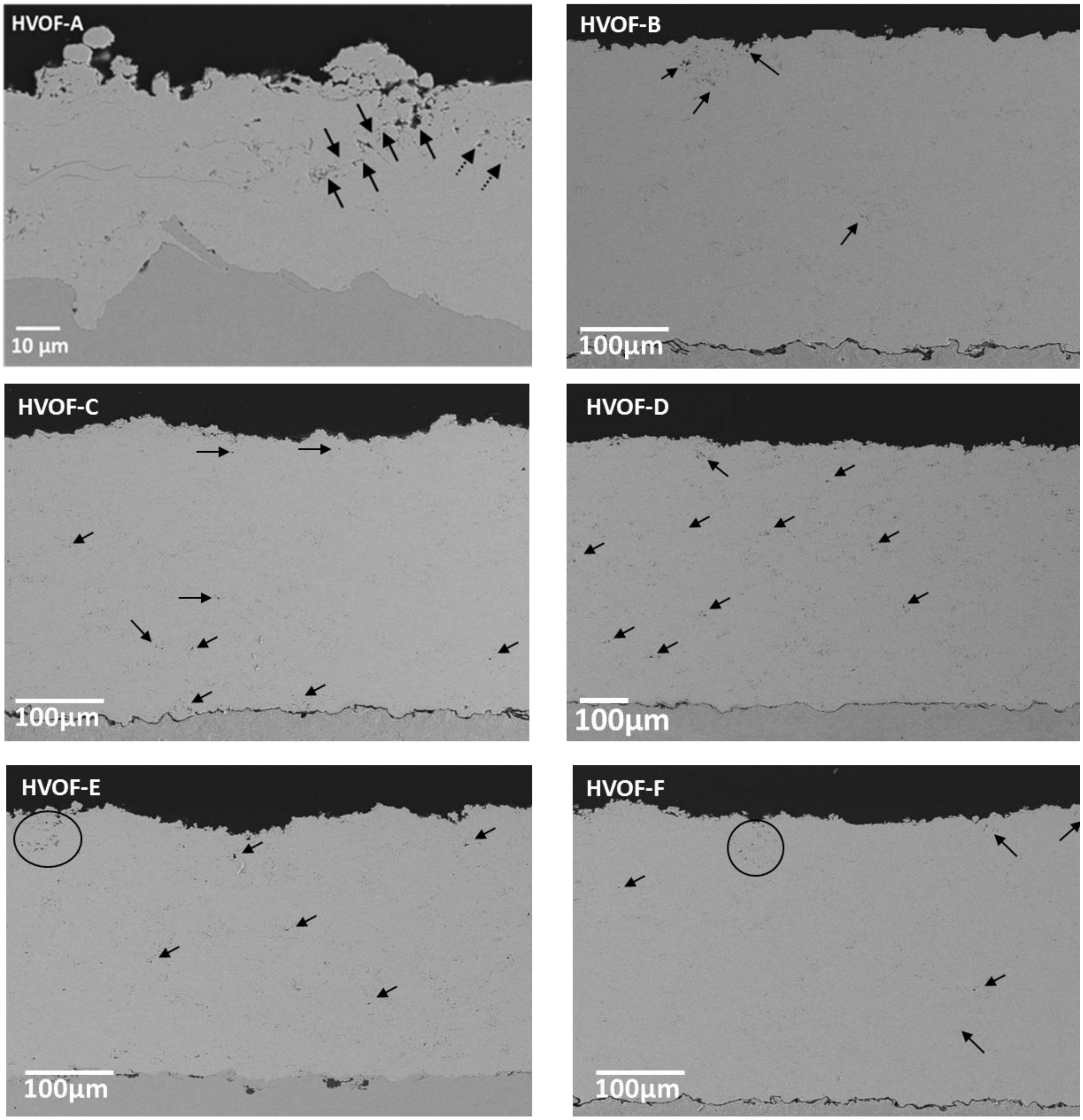

Figure 4.11: Cross- sectional scanning electron micrograph of non-corroded HVOF JK sprayed Ni. Arrows and circle are for visual aid for pointing to the pores.

However, it can be observed that HVOF-D which has highest thickness has corrosion performance similar to HVOF-A. The microstructure for HVOF-D shows presence of large number of pores compared to other coatings HVOF-B to HVOF- F. This coating was synthesized at high feed rate. Consequently, due to introduction of large number of particles the particles have to compete to absorb heat from the flame. Hence, there was local drop in temperature which may have contributed to less efficient heating of the particles. Also, the velocity of the particles is low for HVOF-D which lead to lowering of the kinetic energy. Therefore, peening is reduced in this coating which results in the presence of large number of pores in the coating.

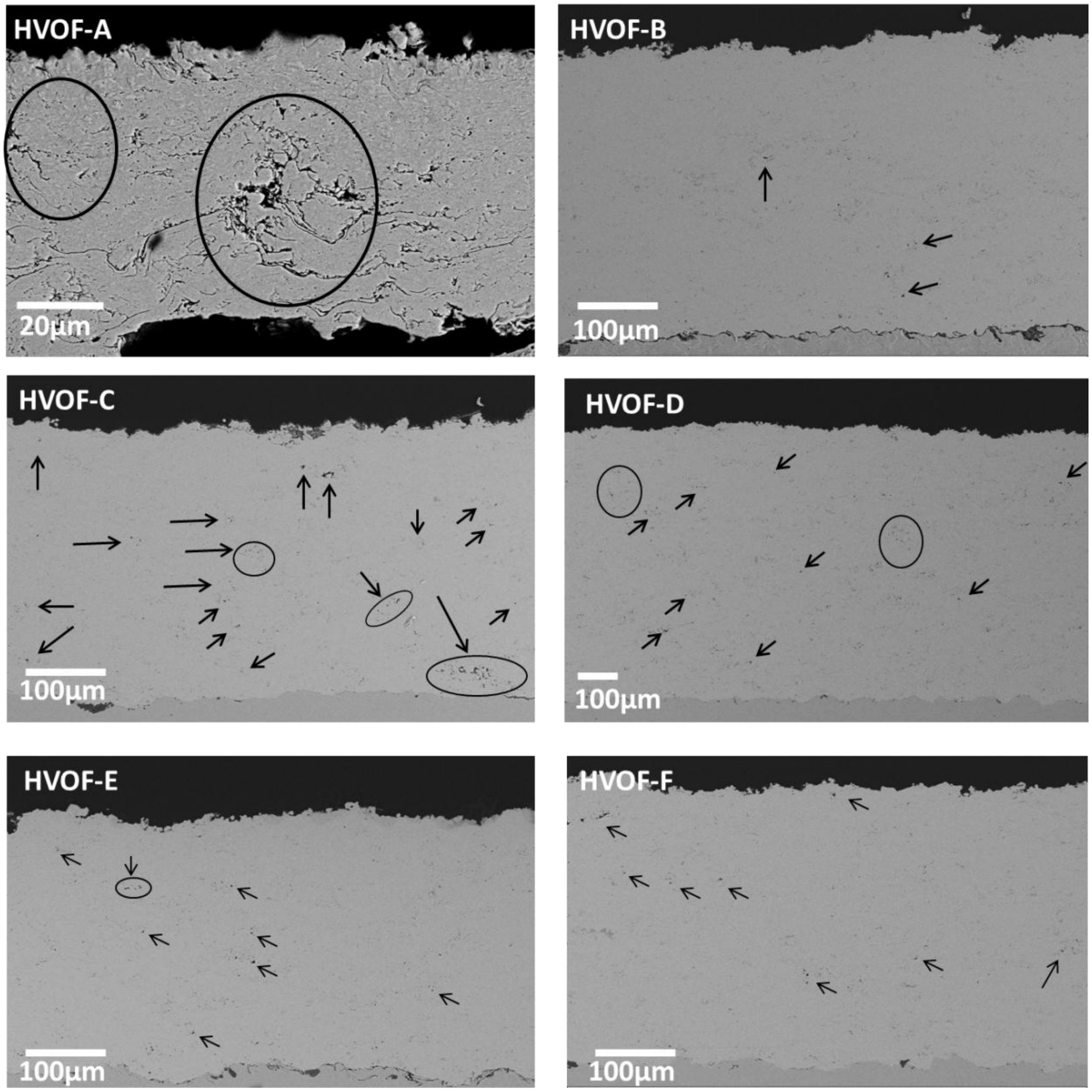

Figure 4.12: Cross- sectional scanning electron micrograph of corroded HVOF JK sprayed Ni. Arrows and circle are for visual aid for pointing to the pores.

Figure 4.12 shows the SEM micrograph for corroded HVOF Ni. After corrosion there is slight increase in porosity and the porosity measurement depicted in figure 4.13 shows the porosity change. Also, it can be noticed that even though the coating thickness of HVOF-C and HVOF-E are similar, HVOF-E outperformed HVOF-C.

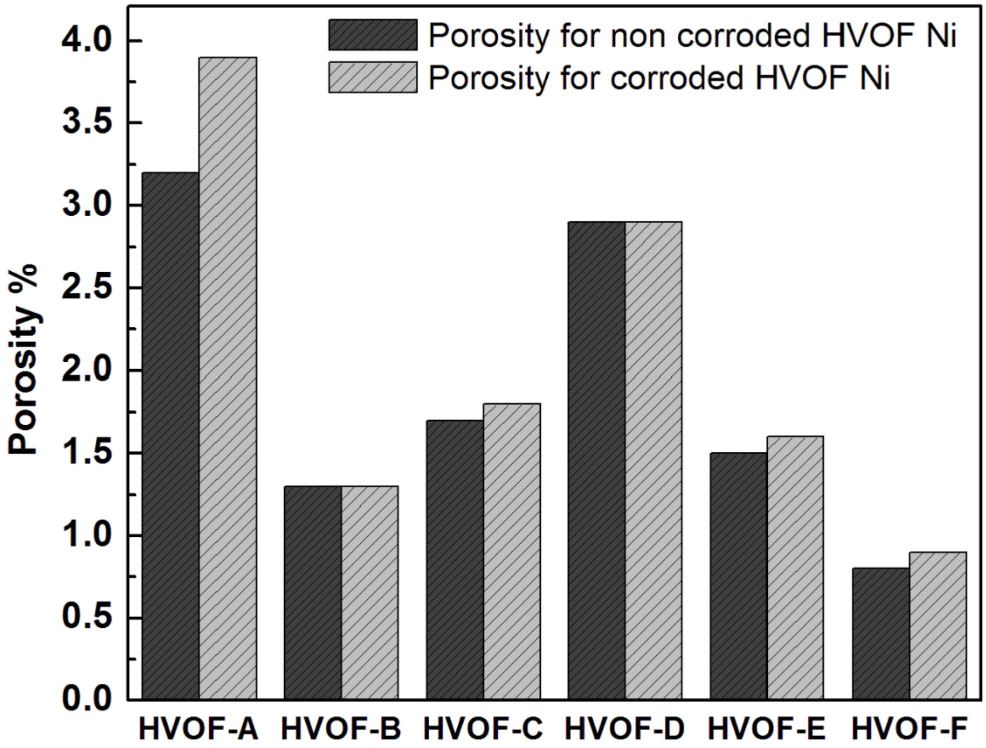

Figure 4.13: Porosity measurement of corroded and non- corroded HVOF JK Ni samples.

From figure 4.11 and figure 4.13 it can be observed that HVOF-C has higher overall porosity in the coating. Whereas the porosity of HVOF-E is more localized at the surface of the coating. Consequently in HVOF-C, the porosity is distributed throughout the matrix, thus increasing the likelihood of interconnecting porosity. This interconnecting porosity allows the corrosive media to penetrate the coating at a faster rate. Similarly, From figure 4.13, it can be seen that the porosity values for HVOF-A and HVOF-D are higher than values of the other HVOF samples as mentioned previously, leading to a higher corrosion potential. The variations of HVOF-A are due un-melted particles, which cause local penetration of corrosive media into coating. The higher porosity values of HVOF-D show that the electrolyte is able to penetrate faster than less porous coatings.

Figure 4.14 shows the first order process map of the HVOF coatings with parameters temperature and velocity. It can be seen that high particle temperature and velocity are important for producing coatings with a dense microstructure and good corrosion performance. The high temperature indicated better melting of particles and thereby coupled with moderate to high velocity helps in achieving dense microstructures.

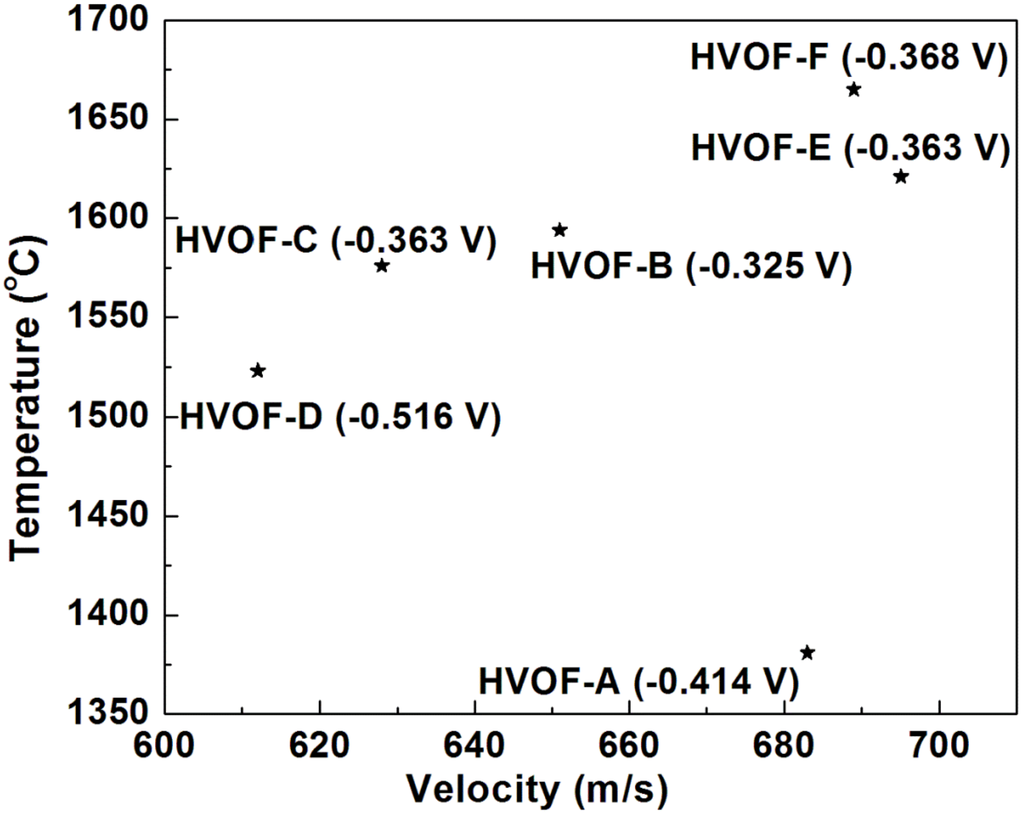

Figure 4.14: First order process map of thermally sprayed HVOF JK Ni. Included in the parentheses besides the sample labels is the highest corrosion potential for a sample.

Feed rate has large influence on the corrosion performance of the HVOF Ni. Coatings deposited with lower and higher feed rate compared to the standard optimized feed rate shows large variability in corrosion potential as shown in figure 4.15. For lower feed rate there are fewer particles in the flame which may lead to overheating the particles. Overheating leads to more oxidation which leads to increased porosity and hence poor corrosion performance of the coating as exhibited by HVOF-A. Also, this coating showed large variation in the corrosion potential. On the other hand higher feed rate leads to introduction of large number of particles in the flame. These particles compete to absorb the surrounding heat for melting. However due to large number of particles the flame cool downs little and there is decrease in the particle temperature as can be seen from figure 4.16. Particles are not enough melted and are not flattened on impingement with the substrate. This leads to increased porosity as is evident from figure 4.13 for HVOF-C and HVOF-D.

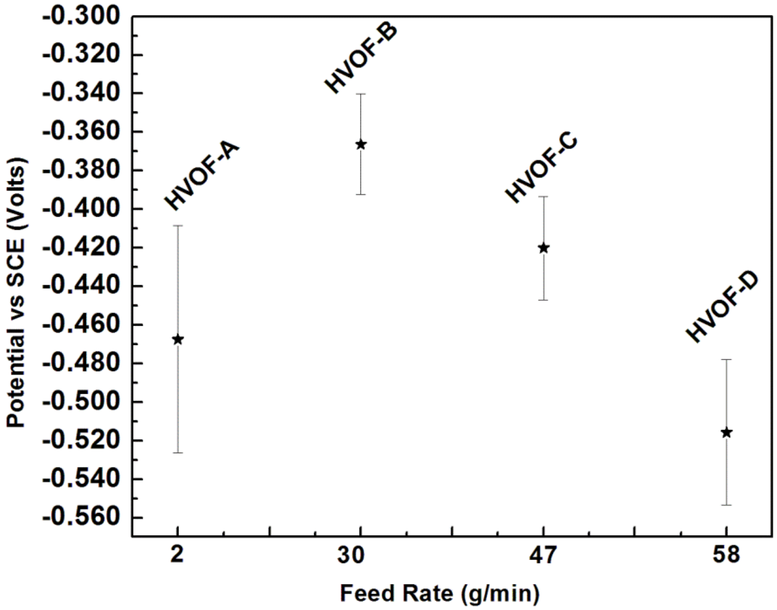

Figure 4.15: Graph of corrosion potential versus feed rate.

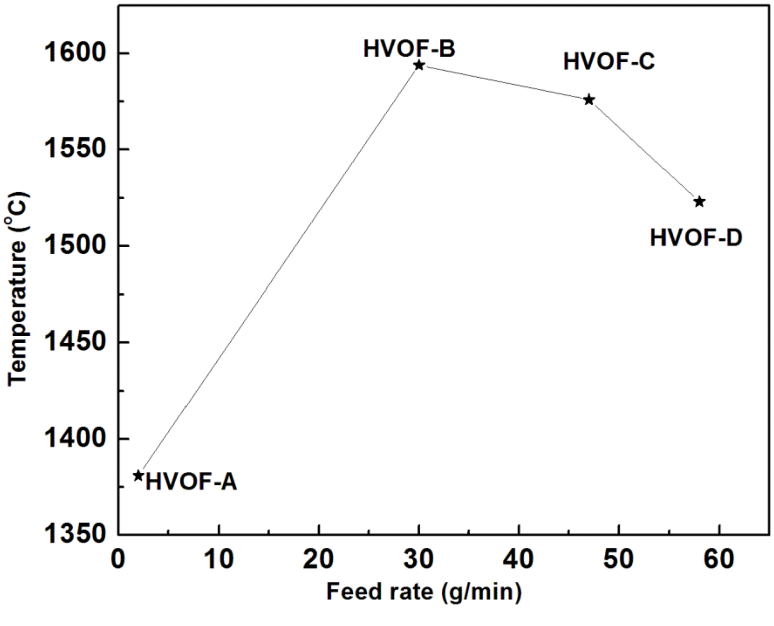

Figure 4.16: Graph of average temperature of the particles versus feed rate for HVOF JK Ni. With increase in feed rate, temperatures decreases.

4.4 Conclusion

Microstructure plays a dominant role in the corrosion performance of TS coatings. The OCP studies on Ni show that for the dense structures of bulk and electroplated nickel stabilization occurs much more quickly (~30 minutes) as compared to porous thermally sprayed coatings where ~ 8 hours was needed for stabilization. The variability in corrosion potential of the coatings is related to their microstructure. The high level of porosity in the APS nickel did not allow for an effective passive barrier. HVOF processing can lead to a dense coating. However, even in HVOF-coated samples variability in E_{corr} is present due to non-uniformity in the microstructure. An appropriate combination of particle velocity and temperature is necessary to produce a corrosion resistant coating. Comparing APS and HVOF it is evident that HVOF process is suitable for depositing corrosion resistant coatings. Furthermore, for HVOF Ni T-V space is beneficial in selecting range of temperature and velocity for obtaining coatings with good corrosion performance. Furthermore, in the literature on the corrosion of thermal sprayed material variability is hardly emphasized. Variability of the thermal sprayed coating is an important issue which describes the corrosion resistance performance of the coating in totality. Through the medium of the present investigation the rationale to pursue the variability in corrosion performance on the same coating is stressed. Furthermore, the effect of feed rate on the corrosion performance is discussed in context to absorption of surrounding thermal energy and heating of the particles. Optimized feed rate enables coating with good corrosion performance by efficient heating of the particles.

Chapter 5

Corrosion Studies of Bulk, APS and HVOF Nickel Chromium (Ni-20 wt.%Cr)

5.1 Introduction

With hard chrome replacement agenda becoming stronger, HVOF systems cermets like WCCo-Cr, WC/NiCr, WC-Ni and Cr_2C_3-NiCr are being increasingly sprayed for EHC replacement. Ni and NiCr are seen to be essential component of the matrix and are expected to exhibit corrosion resistance against corrosive environment [69, 70]. Normally, if WC is used with Co or Ni then due to galvanic coupling formation Co or Ni can corrode which can lead to lose of WC particles and is detrimental causing failure of the coating. Addition of Cr to binder will improve corrosion performance of the binder [69]. Moreover, NiCr composition is present in many superalloys and corrosion resistant alloys. There has been not much investigation on the aqueous corrosion of thermally sprayed NiCr. In the earlier studies corrosion studies on Ni deposited by different techniques like electro-deposition, cold spray, APS and HVOF have been carried out in 3.5% NaCl electrolyte. It was found that by optimizing the process parameters, corrosion resistance can be increased for the HVOF Ni. In the present study effect of addition of Cr to Ni in the form of NiCr alloy has been investigated by using different thermal spray system. Use of thermal spray system for corrosion resistance performance demands optimization of the process parameters for repeatability and best performance of the coatings. Investigation of the simple system NiCr, attempt has been made to understand the role of processing parameter-microstructure for a single torch or across different thermal spray torches on the electrochemical performance of the thermally sprayed NiCr coatings.

As the coating develops stresses are induced in the coating. The stress that develops during deposition is termed as the evolution stresses. Depending on quenching and peening evolution stress can be tensile or compressive. Quenching stress is related to immediate cooling contraction and solidification of molten splats and has tensile stress associated with the process. On the other hand peening stress is related to high kinetic energy of the splats. The peening stress arises due to impact and plastic deformation of an impacted layer. This stress is compressive in nature. After deposition as the coating cools down there may be thermal expansion or contraction mismatch due to difference in thermal coefficient difference. This stress is termed as thermal mismatch stress and is tensile in nature. The overall stress that remains in the coating is the residual stress. These stresses affects the adhesion-cohesion, micro and macro cracking if the microstructure of the coating.

In addition of the influence of particle, the influence of coating thickness on corrosion performance is important to study for industrial applications. It is believed that as the thickness increases the interconnected porosity becomes highly tortuous, making the electrolyte infiltration through them towards the substrate extremely difficult. Hence, in the present study the thickness effect on corrosion performance is carried. Even though thermally sprayed NiCr is used for high temperature oxidation application the present study can be seen as a starting attempt in the corrosion community to establish thermally sprayed NiCr coatings suitable for aqueous corrosion application.

5.2. Experimental Description

5.2.1 Feedstock and Substrate Description

Low carbon steel plates AISI 1018 with dimension of 223 mm x 25.4 mm x 1.4 mm were used as substrate which is used for ICP measurements. Prior to deposition the substrates were grit blasted using 60 micron alumina grit with pressure of 55 – 60 psi on both sides for same time to balance the peening stress during blasting. Substrates were placed on ICP-4 sensor to monitor stress evolution during deposition. Due to differences in feed rate capacity and deposition efficiency of the different spray torches, different number of passes was used in the experiments to produce coatings with similar thickness of around 0.2 mm.

Ni-20 wt.% Cr powder from Praxair Surface Technologies (Ni-105-2, Indianapolis, USA), and Sulzer Metco (Metco 43VF-NS, Westbury, USA) (particle size 5 to 45 μm both) was used to spray the coatings. Powder was in spherical morphology with grain size at about 1- 2 micrometers. Accuraspray sensor (Tecnar, Canada) was used to measure particle temperature and velocity of coatings sprayed by *DJ*, *JK* and *Woka* systems. DPV2000 (Tecnar, Canada) was used for *Triplex* conditions. Particle state for *JP* condition was not measured. Accuraspray senses ensemble particle temperature and velocity, whereas DPV can measure individual in-flight particles.

To study the effect of tailored residual stress on corrosion performance, NiCr powder was sprayed by a hydrogen-fueled Jet-Kote 3000 torch (Deloro Stellite, Inc.) using a 228.6 mm nozzle. The nozzle inner diameter was 6.35 mm. Particle state was monitored by an Accuraspray sensor, based on the two-wavelength pyrometry principle (Tecnar, Quebec, Canada).

5.2.2 NiCr Sample Description

Tempered bulk NiCr (Ni 72-76 wt %/ Cr 18-21wt %) was obtained from Goodfellow (Goodfellow Cambridge Ltd., Huntington PE296WR, England). Five different thermal spray systems were used for coating deposition with particle states being measured during flight. The details of the spray system can be found elsewhere [26]. The process parameters used for the deposition of the NiCr coatings is depicted in Table 5.1.

Table 5.1: Thermal spray process parameters for Ni-20%Cr sample [26]**.**

Process type	torch	condition	Fuel type (slpm)	Fuel Flow	O_2 (slpm)	Carrier gas (slpm)	Air (slpm)	Feed rate (g/min)	T (C)	V (m/s)
HVOGF	DJ2700	A	Propylene	60	198	Nitrogen 25	351	23	2100	730
		B		92	166				1800	800
		C		63	218				2200	760
		D		78	196				2100	830
	JK-III	Std	Hydrogen	590	212	Ar-27	N/A	41	1900	720
HVOLF	Woka-star600	Low E	Kerosene (slph)	13.2	613	N_2-11	N/A	40	2000	375
		Medium E		18.9	875				2150	750
	Jp5000	Std.	kerosene	19.3	800	N_2-60		80		
APS	Triplex Pro200	Low speed	N/A	N/A	N/A	N_2-N/A	N/A	90	2420	150
		High speed							1920	690

HVOGF: high velocity oxygen gas fuel; **HVOLF:** high velocity oxygen liquid fuel; **APS:** Atmospheric plasma spray

For high velocity oxygen gas fuel (HVOGF) torches Diamond Jet 2700 denoted as DJ (Sulzer Metco, Westbury, NY, USA), and Jetkote III denoted as JK (Deloro Stellite, Goshen, IN, USA) were used. In DJ four different conditions (ABCD) as shown in Figure 5.1 were selected with propylene as the fuel. For JK one condition with hydrogen as a fuel was selected.

For high velocity oxygen liquid fuel (HVOLF) WOKAStar 600 denoted as WOKA (Sulzer Metco, Westbury, NY, USA) with nominal energy conditions were used to deposit NiCr coatings. This coating is denoted Woka medium energy (WokaME). For the second coating the fuel and gas flow were decreased by 30% and the low energy condition was used for deposition (WokaLE). The JP5000 torch denoted as JP (Praxair, Concord, NH, USA) with standard conditions was also used. Both these torches used kerosene as fuel.

For APS, a Triplex Pro200 torch, with two conditions of significantly different particle velocity was used. For low speed (LS), torch nozzle of 9 mm diameter was used and conditions were selected so that the particles have velocity around 150 m/s. While in the other process for Triplex high speed (HS) a De-Laval nozzle with particle velocity of 690m/s was used.

Table 5.2 lists the spraying parameters tabulated in the form of an L9 (3^4) orthogonal array for the coatings designed to tailor residual stress. Parameter D (Combustion pressure) presents some insignificant fluctuation amongst the spraying runs. That occurred because oxygen and hydrogen flow had to satisfy simultaneously parameter C (Oxygen-Fuel ratio). The three average levels for parameter D are: D_1: 0.31 MPa, D_2: 0.41 MPa, D_3: 0.51 MPa. The number of passes ranged accordingly to the feed rate in order to produce coatings of similar thickness. The thicknesses of the coatings ranged from 250 μm to 300 μm. The details of the experimental procedure are discussed by [76].

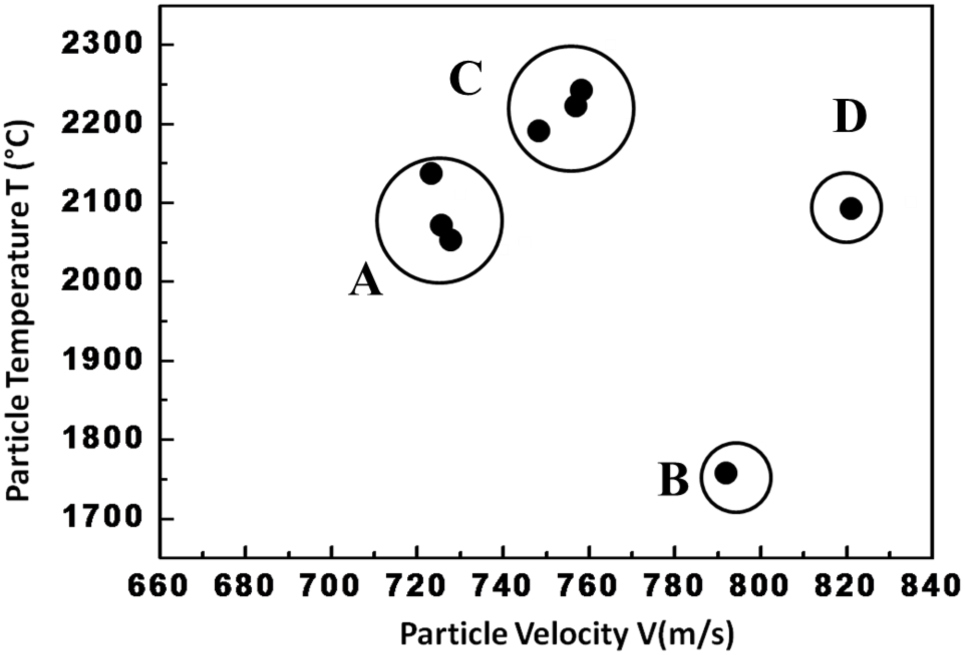

Figure 5.1: T-V conditions for DJ NiCr A, B, C and D sample [26].

Table 5.2: The experimental conditions in the form of an L9 (34) orthogonal array. The values in brackets indicate the level of each factor [76].

Run No.	A.Feed rate (g/min)	B.Distance (mm)	C.Oxygen-Fuel ratio	D.Combustion pressure (MPa)
1	20 (1)	152 (1)	1.2 (1)	0.30 (1)
2	20 (1)	203 (2)	1 (2)	0.41 (2)
3	20 (1)	254 (3)	0.8 (3)	0.52 (3)
4	40 (2)	152 (1)	1 (2)	0.51 (3)
5	40 (2)	203 (2)	0.8 (3)	0.32 (1)
6	40 (2)	254 (3)	1.2 (1)	0.41 (2)
7	60 (3)	152 (1)	0.8 (3)	0.42 (2)
8	60 (3)	203 (2)	1.2 (1)	0.50 (3)
9	60 (3)	254 (3)	1 (2)	0.31 (1)

5.3. Results and Discussion

In this section the results obtained by electrochemical studies including open circuit potential (OCP) and potentiodynamic scanning for various NiCr is presented. Both techniques provide invaluable qualitative information about the corrosion behavior of the coating. OCP provides information about time for stabilization of the samples and hints at the coating performance. Potentiodynamic scanning is a destructive technique and provides information about susceptibility of the coating for corrosion, passivity, corrosion rate and pitting. Furthermore, the microstructure study by scanning electron micrograph is helpful in understanding the potentiodynamic results.

5.3.1 Electrochemical Studies of Bulk, APS an HVOF NiCr

OCP Measurements

The OCP for NiCr samples are shown in Figure 5.2. It can be seen that the coatings are well stabilized after 12 hours. The OCP for thermally sprayed NiCr shows wide variation in the potential ranging from -150 mV to -650 mV. In some of the samples, the OCP show oscillatory behavior due to electrolyte penetration, formation and destruction of the oxide layer [77]. During the destruction of the oxide layer the OCP decreases and as soon as the oxide layer heals, it rises. From the figure it can be observed that the OCP for the different thermal spray system shows wide variation except the APS system which shows low OCP for the Triplex sprayed system. All the other system exhibit mixed performances with respect to the OCP.

OCP for the HVOGF systems increases from the time of immersion except NiCr D. The OCP for NiCr D decreases rapidly in the first hour and stabilizes to ~ -0.550 V. From the SEM it can be seen that NICr D has large pores compared to other HVOGF NiCr systems. JK has dense microstructure compared to other HVOGF which resulted in the difficult infiltration of the electrolyte to the substrate. Except NiCr D the OCP for the HVOGF are near to bulk NICr.

OCP for the HVOLF system shows that OCP for Woka LE decreases from the time of its immersion in the electrolyte and stabilizes within first few hours (~ 4 hours) to nearly -0.650 mV near to that of steel. The decrease in OCP suggests interconnected pathways facilitating the passage of electrolyte to the substrate. On reaching the substrate galvanic pairing of the substrate and nobler coating occurs resulting in the decrease of the OCP. The SEM micrograph also supports the fact that due to large number of unmelted particles the electrolyte can have easy pass across the particles to reach the substrate. The OCP for WOKA ME increases from the initial time of immersion and stabilizes around ~ -0.250 V. In these coatings the oxides formed along the pathways may be blocking the further passage of the electrolyte to the substrate resulting in the increase of the OCP. However, the oscillations observed in these coatings are due to breaking and repairing of the oxide layers.

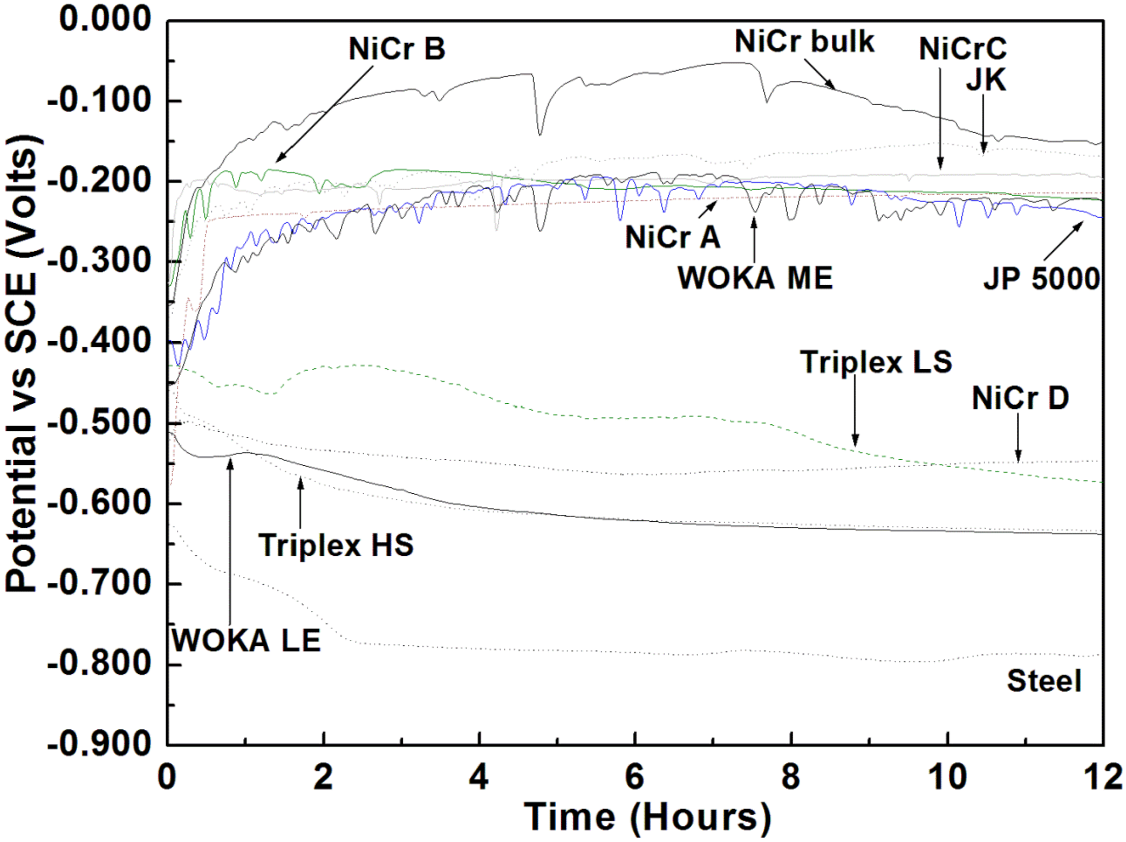

Figure 5.2: Open circuit potential for thermally sprayed NiCr conducted in 3.5 % Nacl.

OCP for the APS sprayed coatings decreases rapidly as soon as the samples are immersed in the electrolyte. However, there is delay in stabilization for Triplex LS as compared to Triplex HS. Triplex HS gets stabilized around 4 hours of its immersion in the electrolyte, whereas Triplex LS takes around 9 hours to stabilize. The OCP for Triplex HS (-0.650 V) at the end of 12 hours is lower compared to Triplex LS (-0.575 V). The OCP measurement suggests that microstructure for Triplex HS has more interconnected pores compared to Triplex LS. In fact from the SEM images it can be observed that Triplex HS has lumpy microstructure due to unmelted particles resulting from its low residence time in the flame on account of its high velocity of 690m/s. Triplex LS has relatively less unmelted particles compared to Triplex HS. Due to the presence of lumped structures, the electrolyte has easy passage across the particles towards the substrate and thus the OCP for these coatings are low and near to the OCP of steel.

Potentiodynamic Measurements

Figure 5.3 shows the potentiodynamic scans for the NiCr samples. From the figure it can observed that NiCr sprayed by APS performs the poorly whereas HVOGF and HVOLF show mixed performances in the static 3.5% neutral NaCl solution. Of all the HVOF process JK coating has highest Ecorr ~ -0.278 v.

The performances of the coatings can be understood from the SEM images shown in figure 4 for the non -corroded coatings. The SEM micrograph shows diverse microstructures across different TS coatings. From the micrograph study the variation and performance of the TS NiCr coatings can be understood. SEM image for the HVOGF coatings show a wide differences in the microstructure of the coatings. NiCrD coating has plenty of unmelted particles, cracks and pores compared to NiCrA, NiCrB, NiCrC. On the contrary it can be observed that JK has homogenous and compact microstructure compared to other HVOGF coatings. SEM images for HVOLF shows WOKALE which has large porosity and cracks. Comparing amongst the Triplex APS coatings, TriplexHS has wide spread unmelted particles throughout the coatings. The boundary of the spherical splats gives rise to high porosity. The high speed of the particles drastically reduced the dwell time in the flame resulting into improper particle-flame interaction giving rise to unmelted particles. TriplexLS has few unmelted particles and the microstructure is compact compared to TriplexHS.

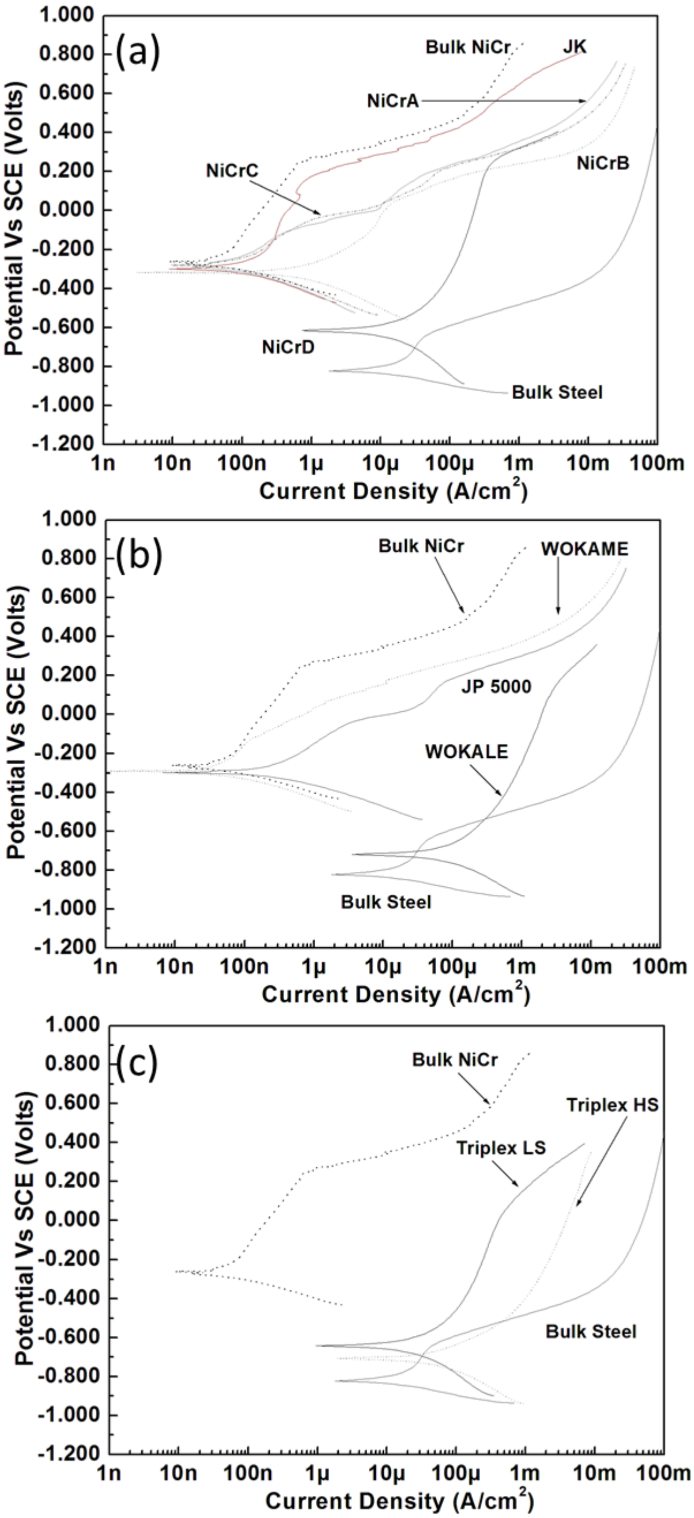

Figure 5.3: Potentio-dynamic scan for (a) HVOGF (b) HVOLF and (c) APS sprayed NiCr in static 3.5% static neutral NaCl solution.

For HVOGF system NiCr D perform poorly with E_{corr} ~-0.612 mV near to steel substrate (E_{corr} ~ -0.827 mV). The low performance of the coating can be understood from the microstructure of the coating. As seen from the SEM images in figure 5.4, NiCrD has high density of pores and cracks. These defects lead to easy electrolyte penetration through the coating and on reaching the substrate the electrolyte attacks the substrate. In contrast, NiCr A and JK exhibit excellent corrosion performance with their E_{corr} near to that of bulk NiCr. The SEM image shows that JK has compact microstructure compared to other HVOGF coatings. The potentiodynamic scan for NiCr C shows that even though has high Ecorr , the current increases with small increase in voltage. Hence, NiCrC is susceptible to pitting.

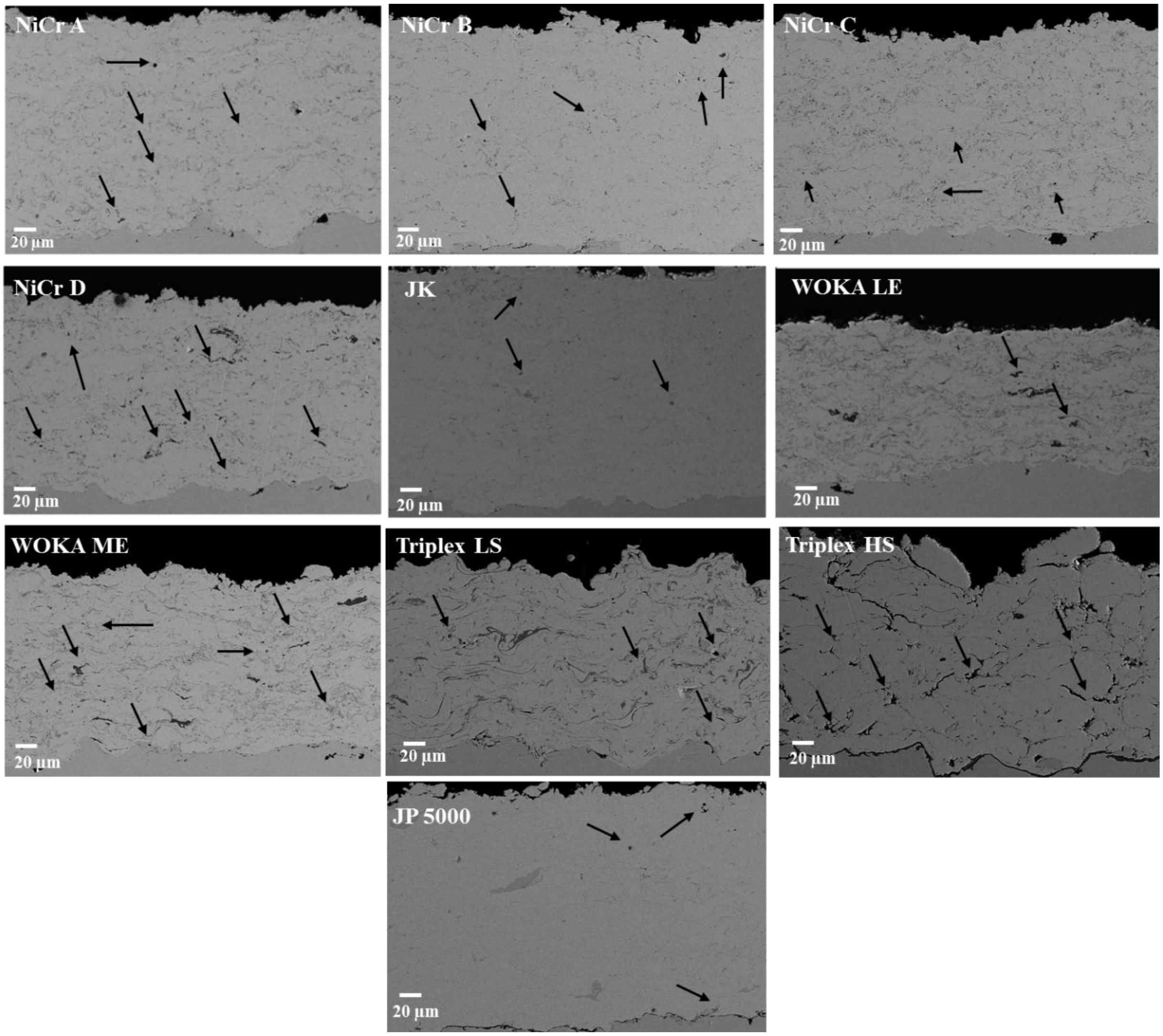

Figure 5.4: SEM image for non- corroded NiCr coatings. Arrows point to the pores present in the coating.

From figure 5.5, The SEM image of the corroded NiCrC coating shows the microstructure with pitting on the surface. It is possible for this coating that the surface oxide layer may have cracked leading to pitting.

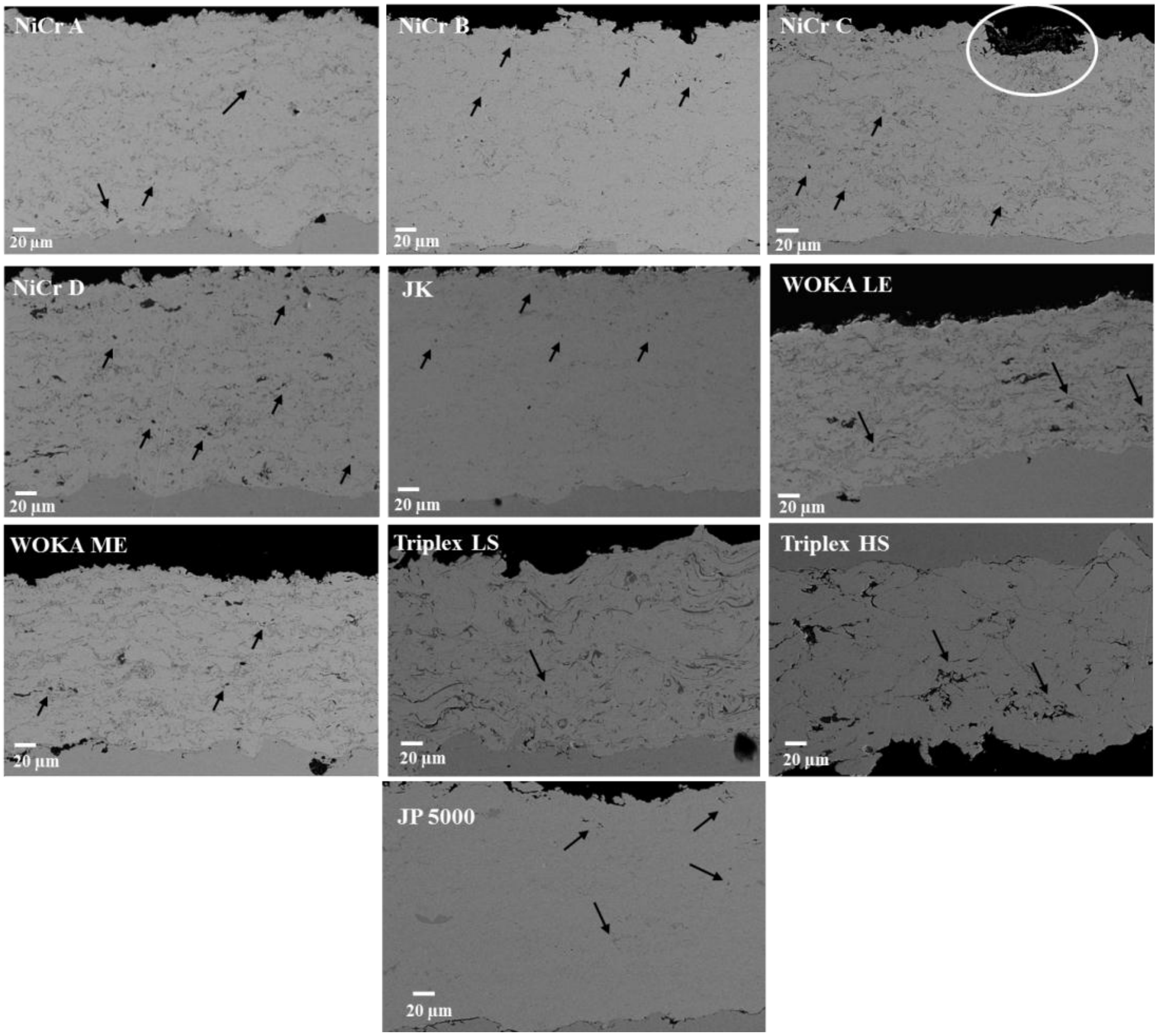

Figure 5.5: SEM image for corroded NiCr coatings. Arrows point to the pores present in the coating. The circle marked for NiCr C is due to pitting.

Porosity of the coatings calculated by image J and the microstructure for the corroded and uncorroded coatings is shown in figure 5.6. APS has the highest porosity. HVOLF and HVOGF exhibit mixed porosity level.

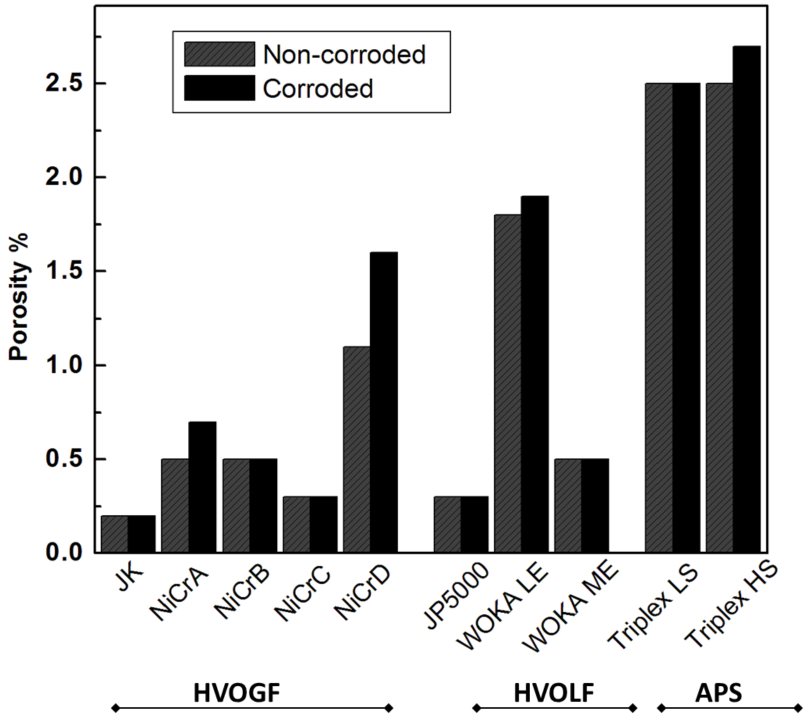

Figure 5.6: Porosity for the corroded and non- corroded thermal spray coatings.

The variation in E_{corr} for the TS samples is shown in Figure 5.7. The HVOF JK showed the best performance. This may be attributed to nominal oxide formation in the coating during the particle- flame interaction. Amongst the NiCr A, B, C and D coatings, sample NiCr C (high temperature and medium velocity) had the least variability and best corrosion performance. Sample NiCr D (medium temperature and high velocity) performed poorly and had large variability in E_{corr}. Sample NiCr B (low temperature and high velocity) had mixed performance. A few spots on the same sample B exhibited superior corrosion resistant performance while few had poor performance.

In HVOLF Woka ME showed better corrosion performance with less variability whereas Woka LE (low enthalpy) had least corrosion performance.

Triplex HS (high speed) shows greater variability and poor performance due to presence of oxides unmelted particles, whereas, Triplex LS has compact E_{corr} distribution. Amongst the three type of TS system APS performed poorly.

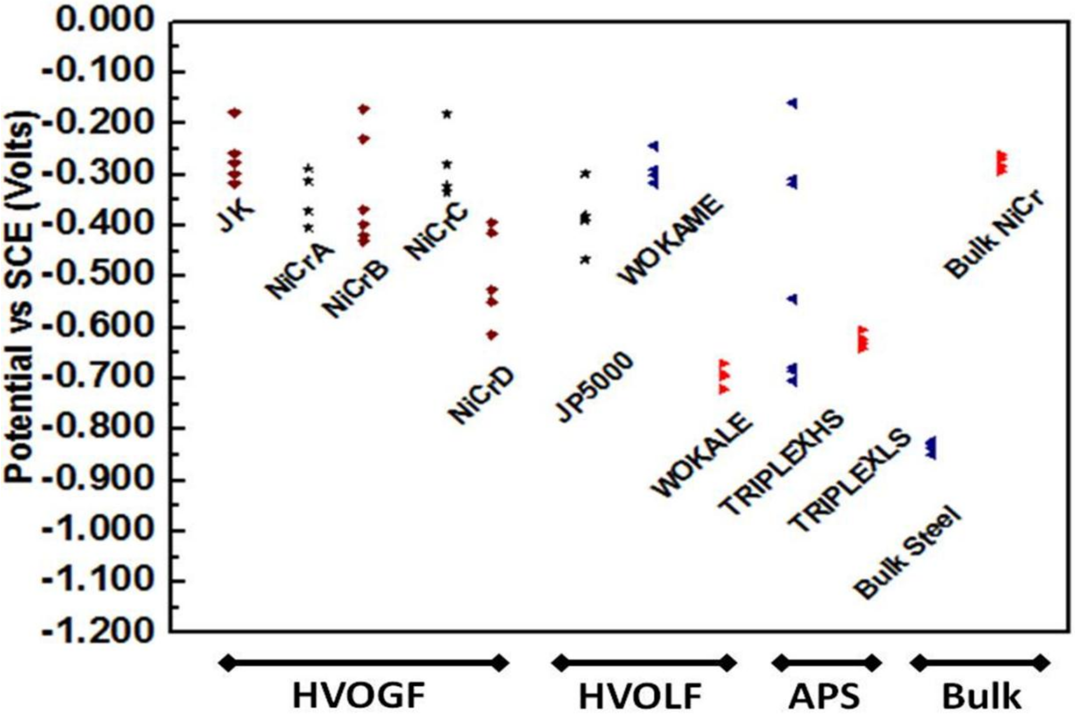

Figure 5.7: Variability in E_{corr} for TS NiCr coatings in static neutral 3.5 wt % NaCl solution.

5.3.2 Influence of T-V on Microstructure and Corrosion

The influence of T-V on corrosion performance can be observed from figure 5.8. T-V space can be divided based on relative corrosion performance of the coatings. From the figure it can observed that coatings with high velocity have higher average corrosion potential. Velocity of the particles affects the dwell time. For the coatings deposited by DJ, WOKA ME, JK, JP the velocity is higher compared to WOKA LE, Triplex LS. Due to the differences in velocity the particles in the former process have low dwell time and low particle flame interaction which leads to lesser oxidation of the particles. Also, higher velocity means increase in peening and better flattening of the particles which lead to increase in density of the coatings. However the coating deposited by APS high speed may have different flame chemistry which adversely affects the corrosion performance. In APS not only the temperature is high but there is easier air entrapment leading to oxidation of the particles. For this coating particles were unmelted as observed in figure 5.4 and the coating had higher porosity. Another important point is the powder injection in APS is radial and external which decreases its dwell time leading to lumpy microstructure with presence of unmelted particles. In WOKA LE the particles have long dwell time for the particle to heat up and is expected that the microstructure will be dense. However, the microstructures shown in figure 5.4 shows presence of unmelted particles. WOKA ME shows comparatively dense microstructure. In WOKA LE even though the dwell time is high the low energy flame heating results into low melting but more oxidation. Whereas, WOKA ME experienced higher temperature for shorter time which resulted into low oxidation and low unmelted particles in the microstructure.

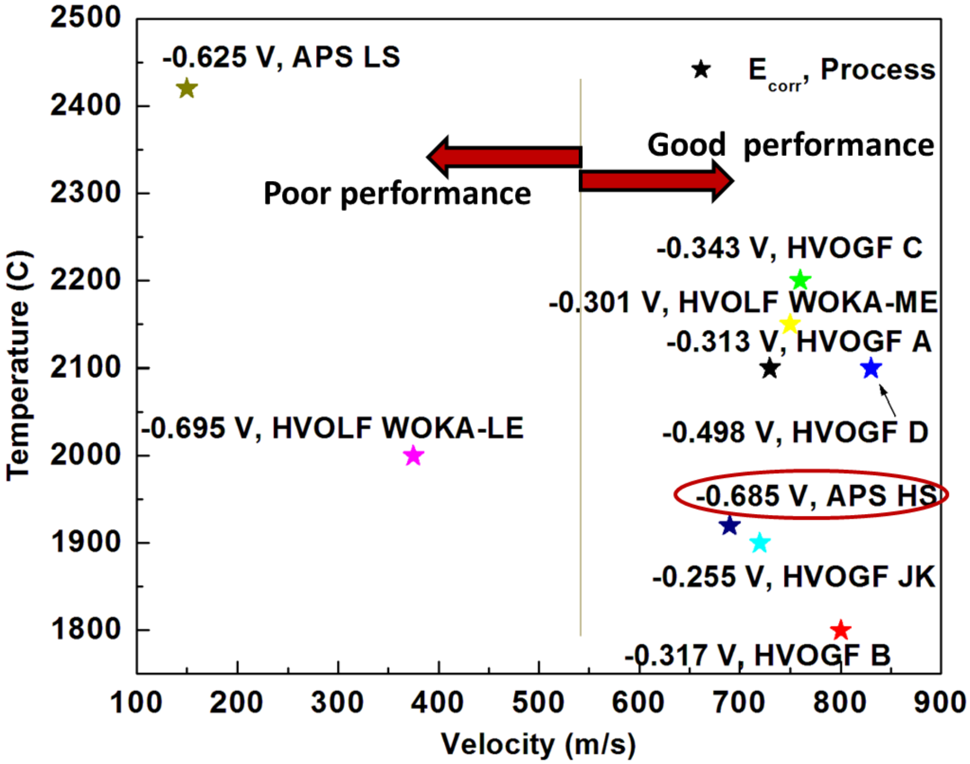

Figure 5.8: Influence of T-V on corrosion performance.

5.3.3 Evolving Stress and Corrosion Performance

Figure 5.9 shows the hardness vs. evolving stress of the thermal spray coatings. The corrosion potential for the coatings is included to show the influence of the evolving stress on corrosion performance. It can be observed that as the evolving stress is more compressive, the corrosion potential becomes nobler indicating better corrosion performance. Corrosion performance is influenced by interconnected porosity. A well compact microstructure has better corrosion performance. With more compressive stress the splats are pressed against each other which results into lowering the porosity. WOKA LE and APS Triplex show relatively higher tensile stress and lower corrosion performance. For WOKA LE and Triplex LS the kinetic energy is low due to lower velocity. This result into peening of lower intensity compared to other coatings resulting in the development of tensile stress.

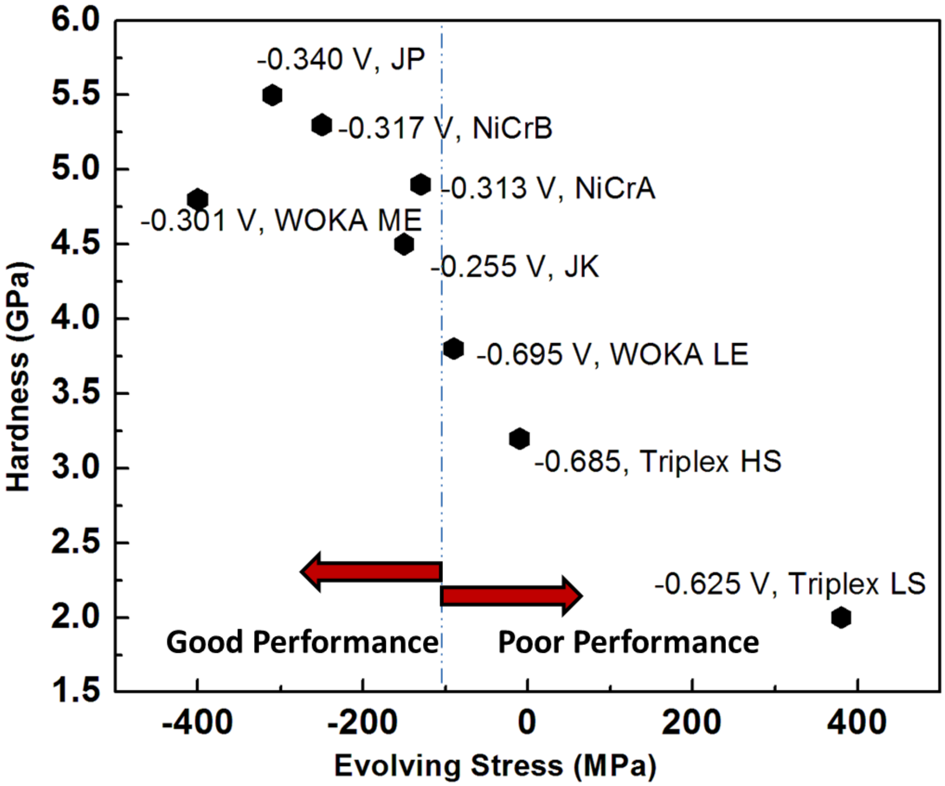

Figure 5.9: Graph of Hardness vs. evolving stress. Corrosion potential is indicated along with the process.

5.3.4 Residual Stress and Corrosion Performance

Figure 5.10 shows the graph of corrosion potential vs. residual stress. It is observed that the coatings JK, DJ, WOKA ME have higher compressive stress compared to APS-Triplex and WOKA LE and show better corrosion performance. Compressive stress tends to close the pores whereas tensile stress tends to open the pores. Consequently, coatings exhibiting tensile stress have higher probability of interconnected porosity and thereby diminished corrosion performance.

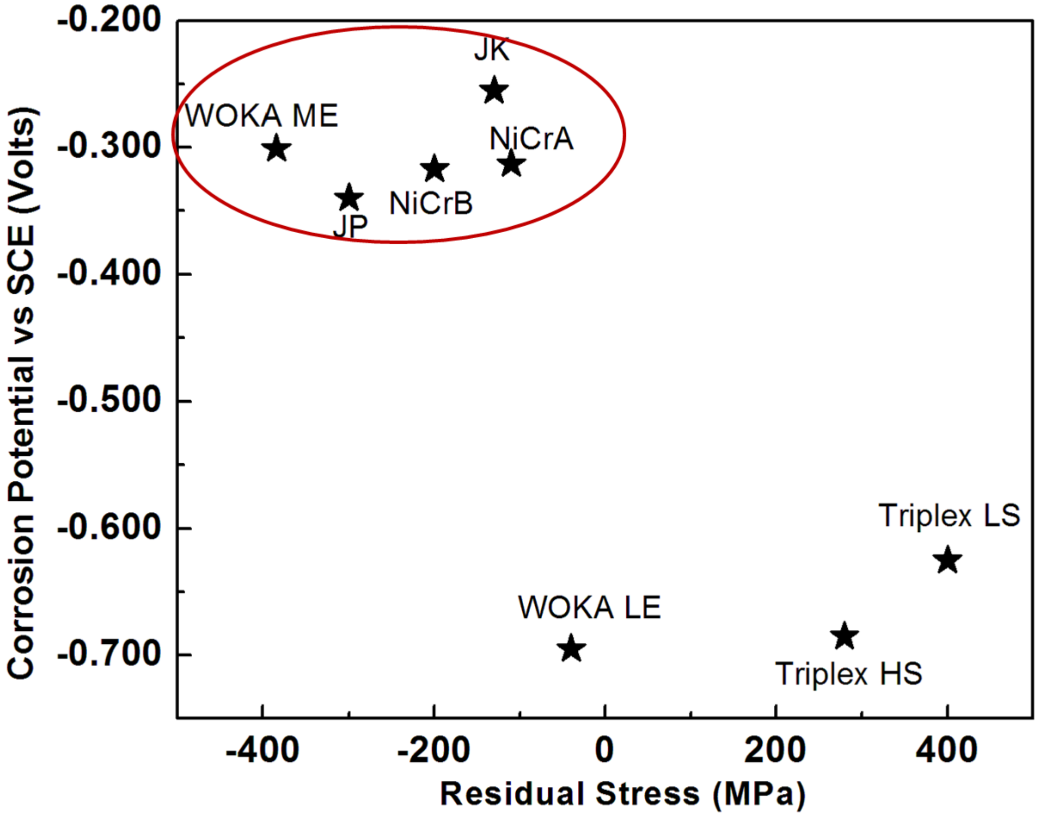

Figure 5.10: Graph of Corrosion potential vs. residual stress. The coatings enclosed in the red circle show compressive stress and higher corrosion performance.

5.3.5 Effect of Thickness Variation on Corrosion Performance

Figure 5.11 shows the variation of corrosion potential with thickness for NiCr JK coating. Clearly, it can be observed that thickness has a marked difference on the corrosion performance of the coating. As the coating thickness increases from 100 µm to 200µm the corrosion potential decreases from -0.550 V to -0.270 V which quite significant. Beyond 200 there is not much reduction of the corrosion potential. As mentioned earlier at lower thickness the electrolyte can have easy passage to the substrate. However as the thickness is increased the interconnected path become highly tortuous and number of path reduces making it difficult for the electrolyte to reach the substrate. Furthermore, it can be observed that the difference in corrosion potential between coating with 200µm and 330µm is small. To understand the difference, the evaluation of residual stress of the coatings will be useful as indicated by figure 5.12. As the thickness of the coatings go from 100 to 200 the residual stress changes from tensile to compressive and corrosion potential becomes relatively nobler. Based on this observation coatings with controlled compressive stress can be developed to mitigate corrosion.

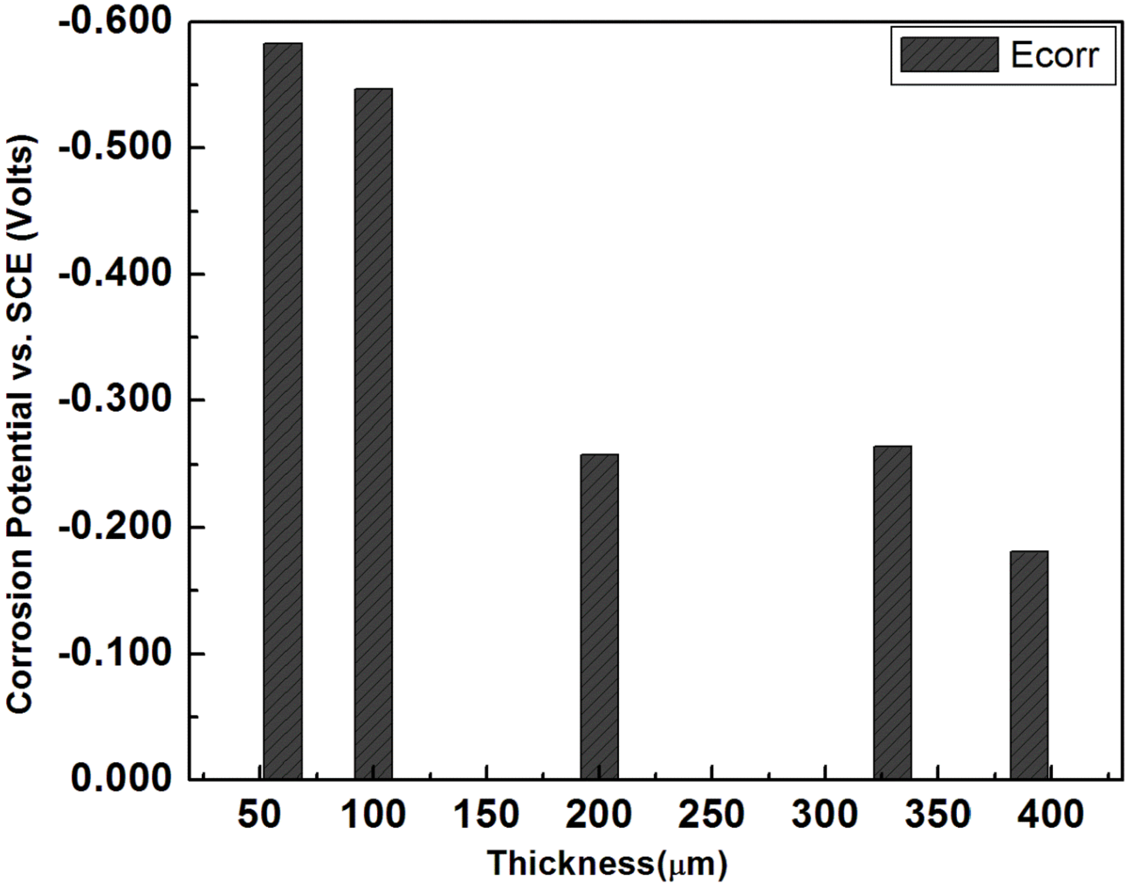

Figure 5.11: Effect of thickness on corrosion potential for JK NiCr coating in static neutral 3.5 wt % NaCl solution.

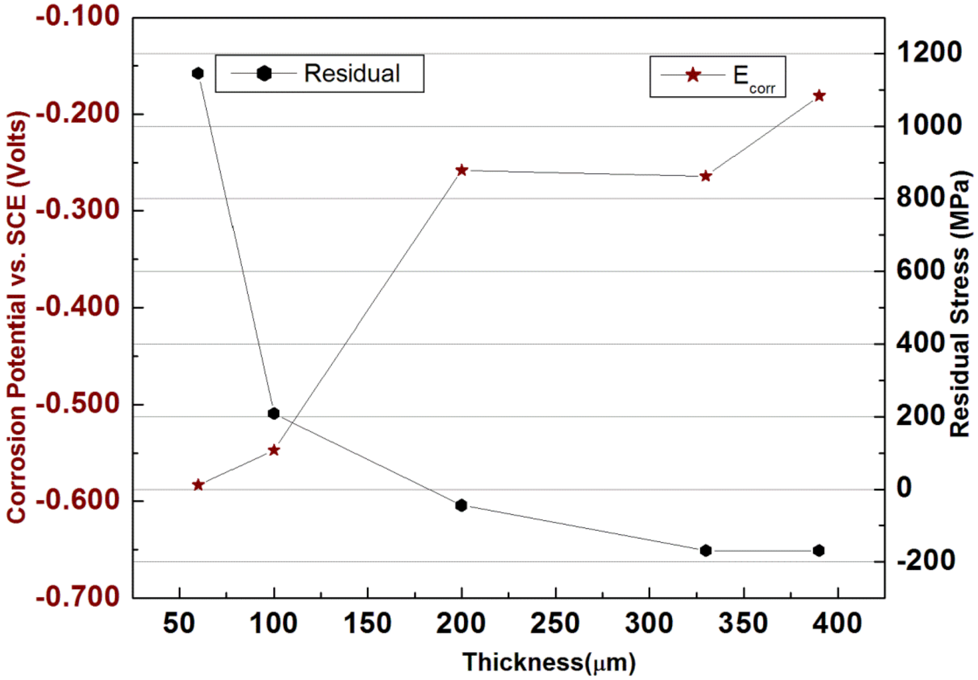

Figure 5.12: Graph of Corrosion potential and residual stress vs. thickness of the NiCr coatings.

5.4 Corrosion Evaluation Based on Tailored Residual Stress

In the last section it was pointed out that tailoring the residual stress is one of the important approaches to control corrosion. In this study distance, combustion pressure, O_2/Fuel ratio and feed rate was varied as described in table 2.

5.4.1 Impact of Processing Parameter on Temperature and Velocity

The graphical effect of each factor in particle in-flight properties is shown in Figs. 5.13 and 5.14. Regarding particle velocity, the most important factors are combustion pressure and distance. Increasing the combustion pressure or decreasing the distance increases roughly linearly the velocity. Temperature is decreased from oxygen-rich (1.2) to fuel-rich ratios (0.8) suggesting oxidation of the particles during their flight. Oxidation occurs due to the high oxidation affinity of Cr. The exothermic reaction of chrome oxides Cr_2O_3 produces enthalpy of -1.14 x 10^3 KJ/mol which adds up heat on the flying particle [78].

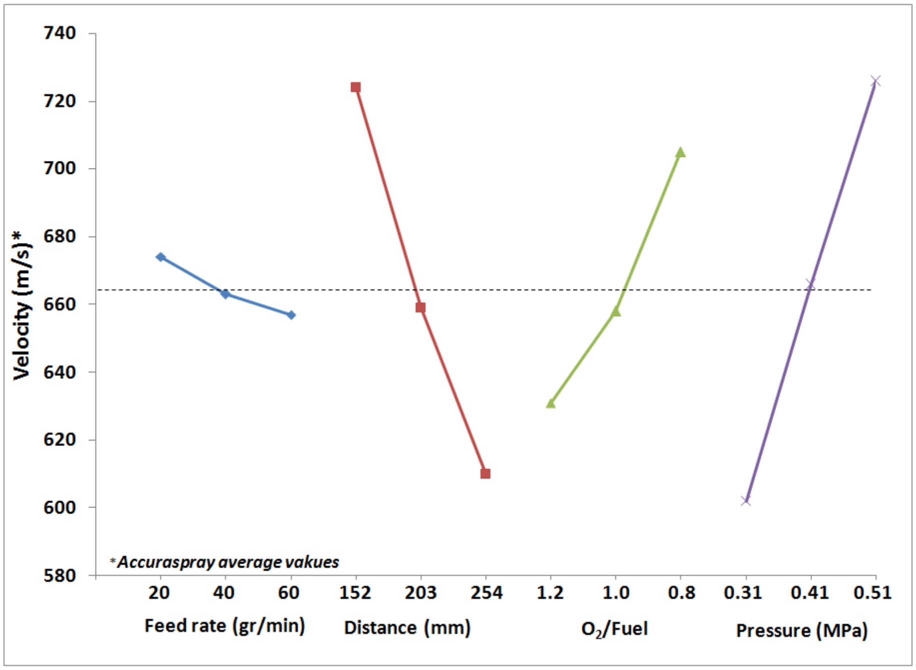

Figure 5.13: The graphical impact of each parameter level on particle velocity Dotted line is the average value [76].

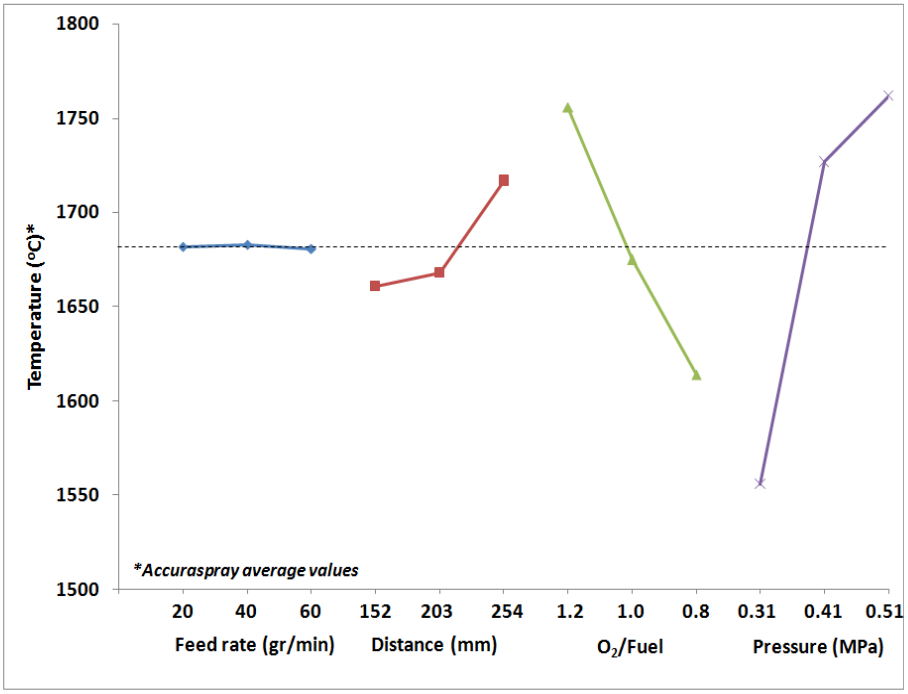

Figure 5. 14: The graphical impact of each parameter level on particle surface temperature (The dotted lines indicate the average values) [76].

The surface temperature readings of Accuraspray are possibly biased by the oxide formation on the outer shell of the in-flight particles. The increased particle temperature by an increasing combustion pressure can be justified by prolonged heating during flight, a direct result of the expansion of the flame.

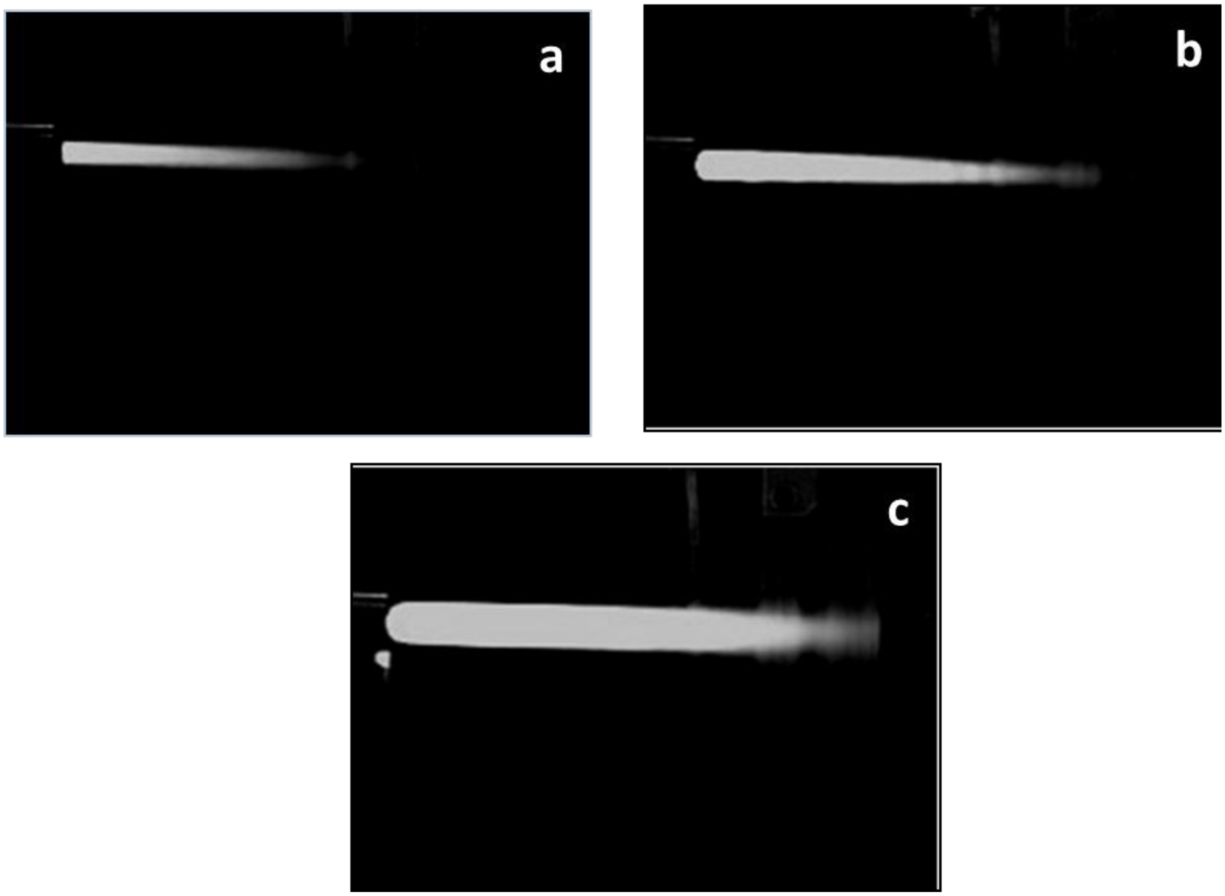

Figure 5.15: (a) 0.31 MPa at 1.2 O_2/F ratio, (b): 0.51 MPa at 1.2 O_2/F ratio, (c): 0.31 MPa at 0.8 O_2/F ratio [76].

In higher combustion pressures the flame is not getting hotter, but it expands in front of the exit of the gun nozzle, extending the supersonic core of the jet (Figs 5.15a and 5.15b)[79]. That forces the particles to receive additional heat as they travel through the hot flame core. However, the increased combustion pressure is not completely capable of preventing air entraining into the flame and oxidation still occurs [79]. At the fuel-rich ratio, the flame is over-expanded, even at low combustion pressure (Fig. 5.15c), due to unburned fuel ignition at exposure in the air-dissolved oxygen. The additional fuel acts as a shroud which minimizes particle oxidation by consuming any available oxygen molecule. Feed rate plays a negligible role in both particle properties.

The coating microstructure is demonstrated in figure 5.16. Co9 has large porosity compared to the other NiCr coatings.

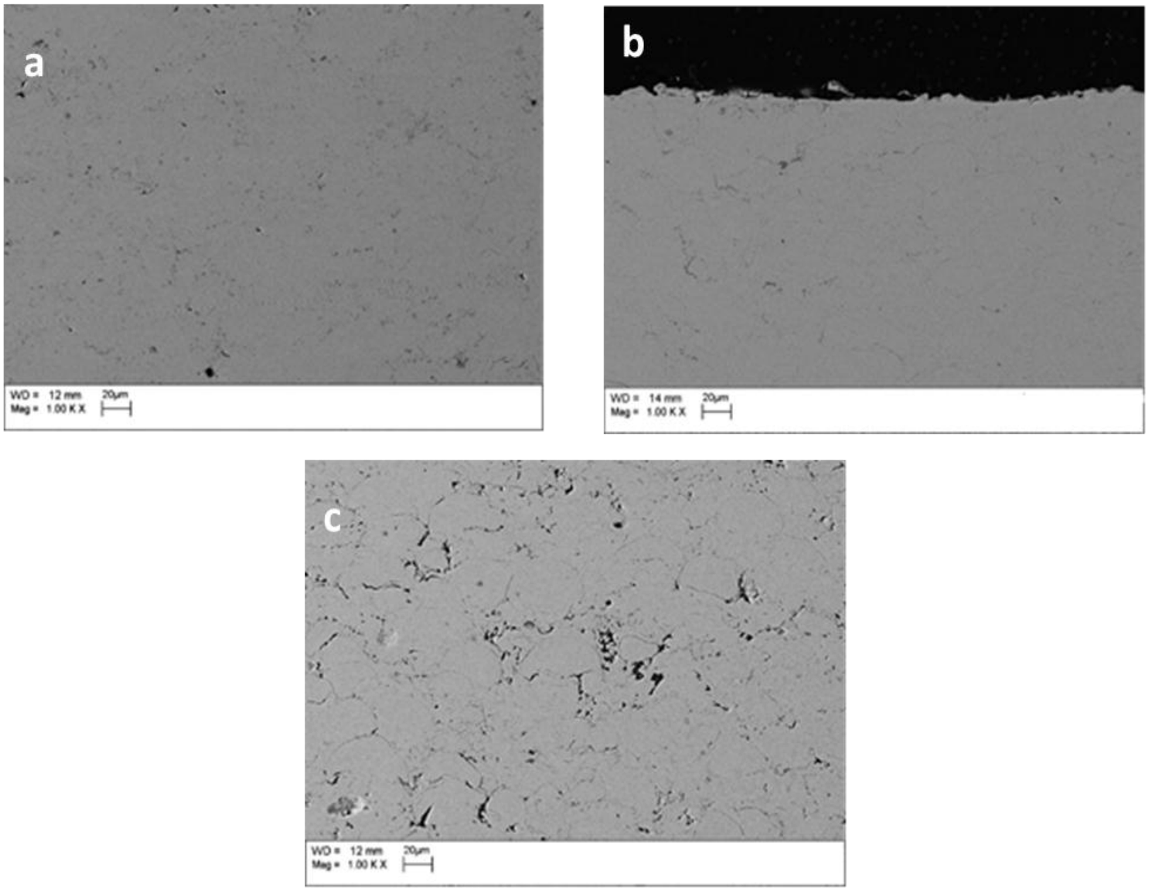

Figure 5.16: Cross section SEM images of the representative NICr coatings a: coating c04, b: coating c06, c: coating c09.

5.4.2 Process Parameter Effect on Stress

As it has been mentioned by previous investigations [80, 81, 82] thermal stresses increase with coating temperature and coating thickness. In the present case, coating thicknesses were kept rather similar, leaving substrate temperature as the main component affecting the curvature ascending degree. It can be noticed in Fig. 5.17 that generally an increasing substrate temperature expands the gap between evolving and residual stresses, as it amplifies the αc-αs difference.

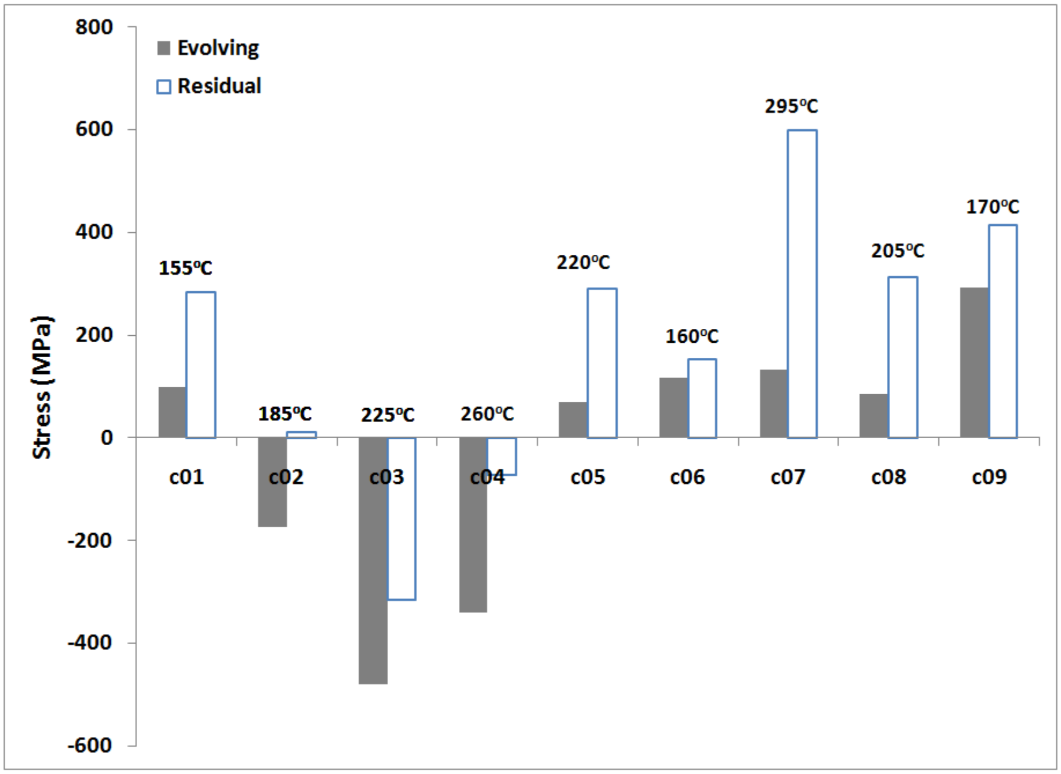

Figure 5.17: Evolving and residual stresses distribution in the deposited coatings. The labels indicate substrate temperature [76].

In general, it has been reported that peening intensity is increasing proportionally to particle velocity [74]. However, high particle velocity solely cannot assure compressive evolving stress. As shown in Figs. 5.18a and 5.19 an increasing feed rate, will shift the evolving stress to less compressive and ultimately to tensile state (60 gr/min). Higher feed rate implies that more particles impinge on pre-deposited splats in every torch pass.

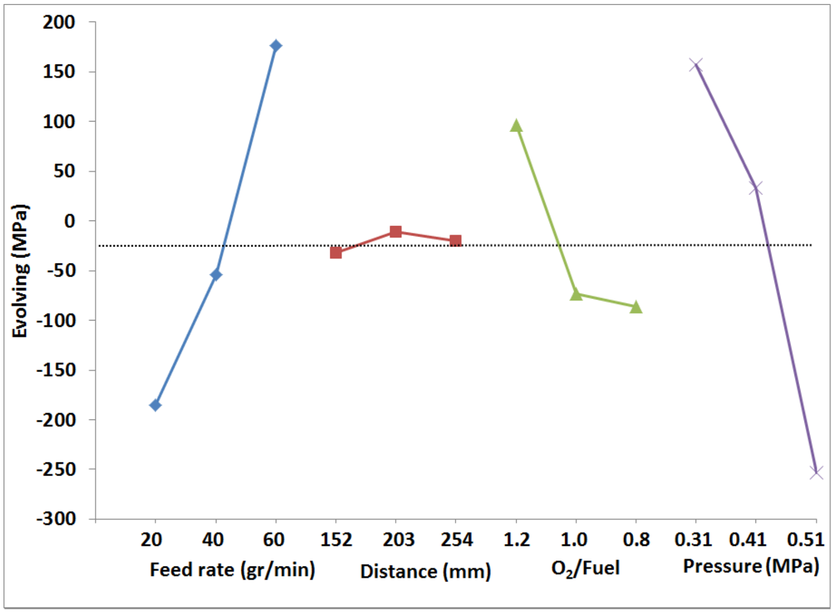

Figure 5.18: The graphical impact of each parameter level on evolving stress [76].

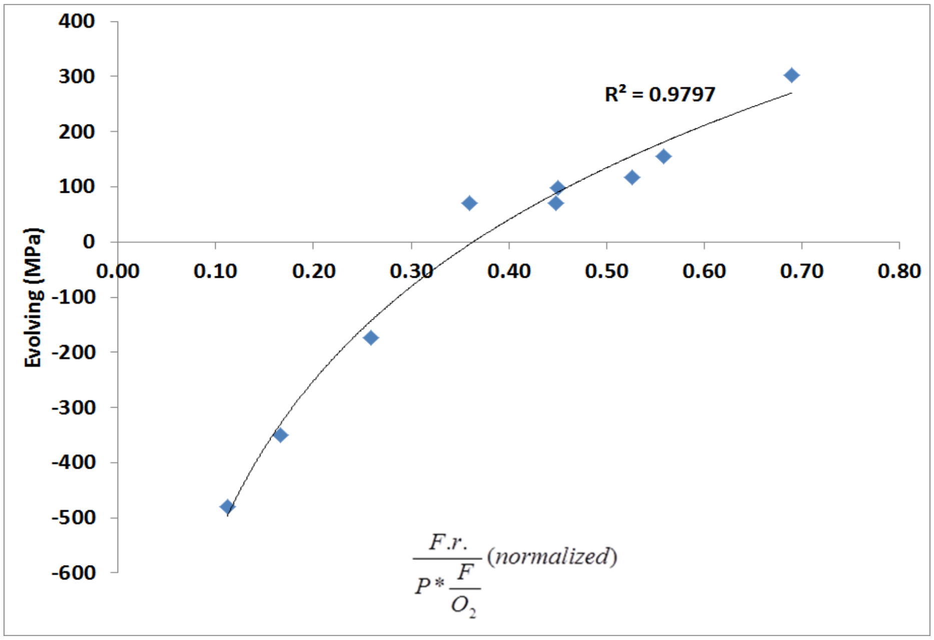

Figure 5.19: Evolving stress prediction as a function of process parameters, (the dots indicate experimental data, F.r: Feed rate) [76].

As the time intervals between impinging particles are extremely short, they tend to bond in a hot state. Hot surfaces of the solidifying particles promote improved wetting, more rapid heat transference and therefore increased cohesion. Better intersplat contact is considered to provide a stronger constraint against the contraction of each splat after solidification which results in significant increase in the values of quenching stress [83]. Moreover, peening is associated with work hardening of the impacted material. The high temperature of the solidifying particles possibly decreases their work-hardening level as recovery takes place during spraying [84]. It is inferred hence, that feed rate promotes an increasing quenching stress trend compared to peening stress. By correlating evolving stress with process parameters, according to the procedure described above, the plot in Fig. 5.19 can be constructed. At the ratio of 0.37, quenching stresses equalize peening stresses. An increase in feed rate or a decrease in combustion pressure shifts the stress to tensile state, while the opposite promotes compressive stress. An oxygen rich flame seems to promote quenching stress at a limited degree, since it decelerates the particles, as shown in Fig. 5.13. The generally good correlation (Fig. 5.19) provides the ability to describe a coating's evolving stress magnitude, by using process parameters. The same correlation for residual stress is more intricate to be employed, since there are additional factors such as the 1st pass curvature-indicative of the adhesion [74]-, varying substrate temperature (Fig. 5.17), *etc*. that should be considered.

5.4.3 Process Parameter Effect on Porosity

Figure 5.20 shows the variation of porosity with process parameters. Higher spraying distance and increasing combustion pressure seem to raise majorly the porosity levels. Conversely, a fuel-rich flame ensures more sufficient melting of the particles, allowing filling of the voids. Porosity seems to be inversely proportional to particle impinging velocity, as they are affected by the same spraying factors. Uncertainties such as particle sections or entire particles pull-outs during polishing and micro-porosity often found in the splat boundaries increase the uncertainty of the measurements table 5.3 and consequently decrease the precision of the regression analysis [85].

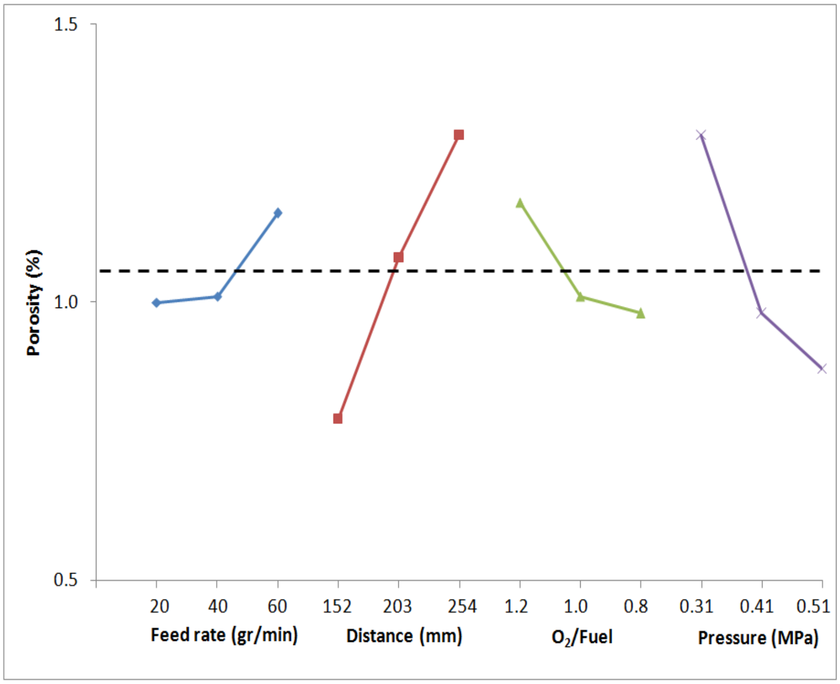

Figure 5. 20: The graphical impact of each parameter level on porosity, (the dotted line indicates the average value).

Table 5.3: Porosity of the deposited NiCr coatings.

Sample	Co1	Co2	C03	Co4	Co5	Co6	Co7	Co8	Co9
Porosity	1.0 ±0.3	0.8 ±0.2	1.4 ± 0.4	0.5 ± 0.2	2.2 ± 0.4	2.2 ± 0.8	0.8 ±0.1	1.1 ± 0.2	1.2±0.5

5.4.4 Corrosion Studies

The potentiodynamic plots of the deposited coatings are exhibited in Figs. 5.21a-c. For comparison, the potentiodynamic polarization scans of a bulk Ni-20 wt.% Cr alloy and of the 1018 AISI substrate steel are plotted. The corrosion (E_{corr}) and pitting potentials (E_p), expressing general and local corrosion are listed in Table 5.4.

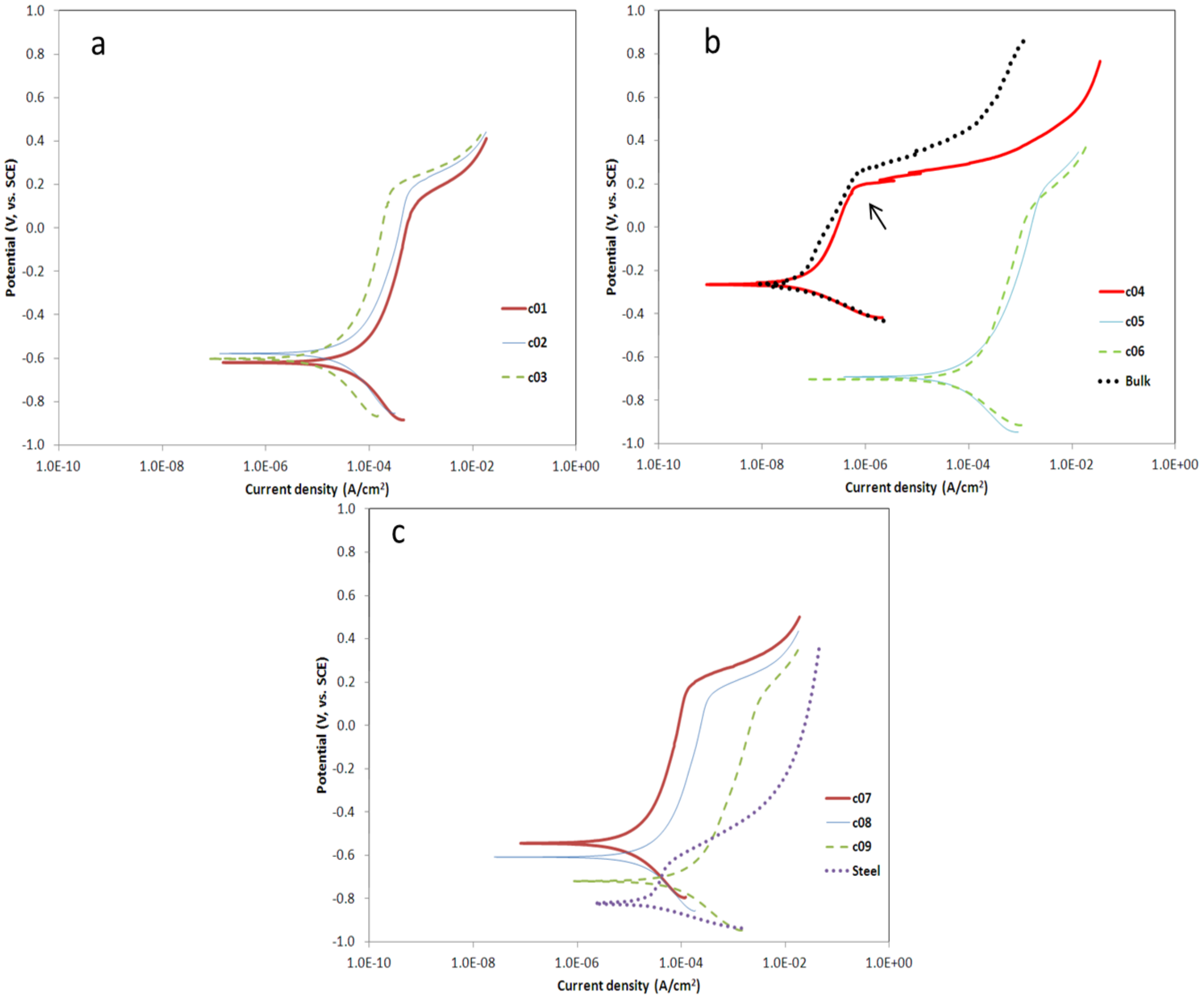

Figure 5.21. (a)Potentiodynamic plots of the deposited coatings in 3.5 wt. % NaCl. a: Coatings c01-c03 (sprayed at 20 gr/min), (b) coatings c04-c06 (sprayed at 40 gr/min) and bulk Ni-20wt. % Cr , (c) coatings c07-c09 (sprayed at 60 gr/min) and 1018 substrate steel.

Table 5.4: Corrosion potentials of the deposited coatings, Ni-20 wt.% Crbulk alloy and 1018 AISI substrate steel.

	Corrosion potential, E_{corr} (V, vs SCE)	**Pitting potential, E_p (V, vs SCE)**
c01	-0.63	0.07
c02	-0.62	0.14
c03	-0.60	0.15
c04	-0.26	0.17
c05	-0.69	0.13
c06	-0.70	0.04
c07	-0.54	0.14
c08	-0.61	0.08
c09	-0.72	0.10
Bulk Ni-20% Cr (wt.)	-0.26	0.21
AISI 1018	-0.83	-0.42

Figure 22a demonstrates the particle velocity influence on the corrosion potential (E_{corr}) of the coatings. This correlation can be justified by an improved intersplat cohesion, reflected on the modulus of the coatings as shown above, which minimizes the number of potential passages to the coating-substrate interface (Fig. 22b). Fig. 22c shows the interrelation between evolving stress and E_{corr}. Generally, under the same feed rate, compressive stress, increases the coatings' E_{corr}. It is worth noting that high tensile stresses cannot ensure substrate protection since the particle impact energy is not sufficient to lessen the intrasplat microporosity. According to that, short spraying distance and high combustion pressure assure nobler coatings, in compliance with the velocity's parameters impact (Fig. 22d). Fig. 22e shows the description of E_{corr} as a function of spraying parameters.

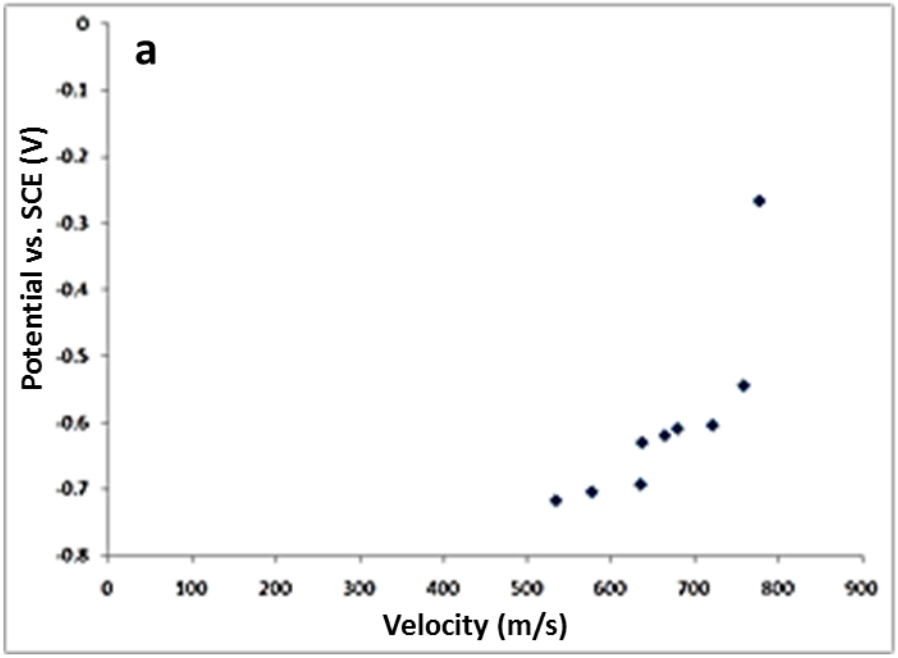

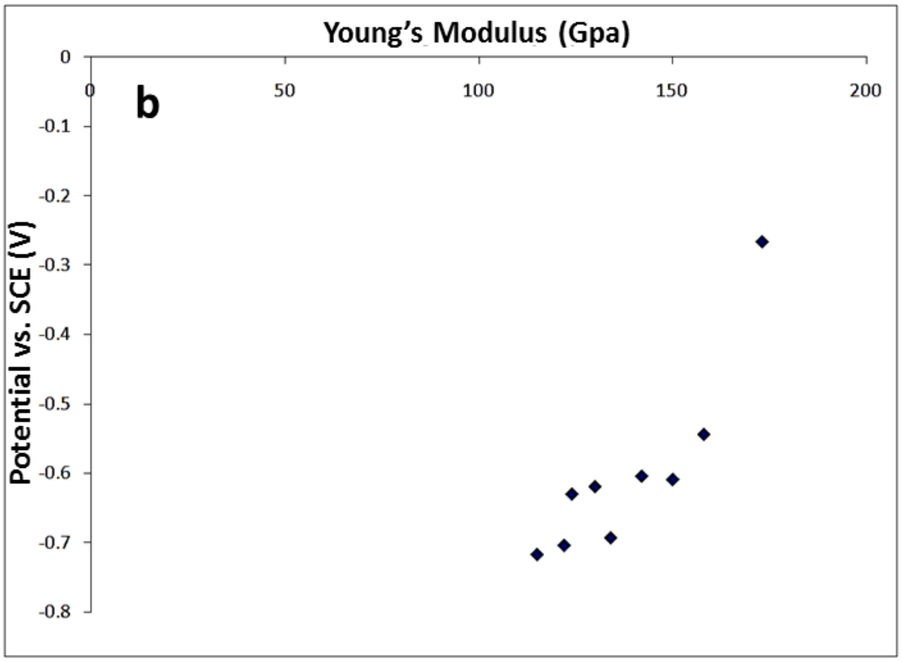

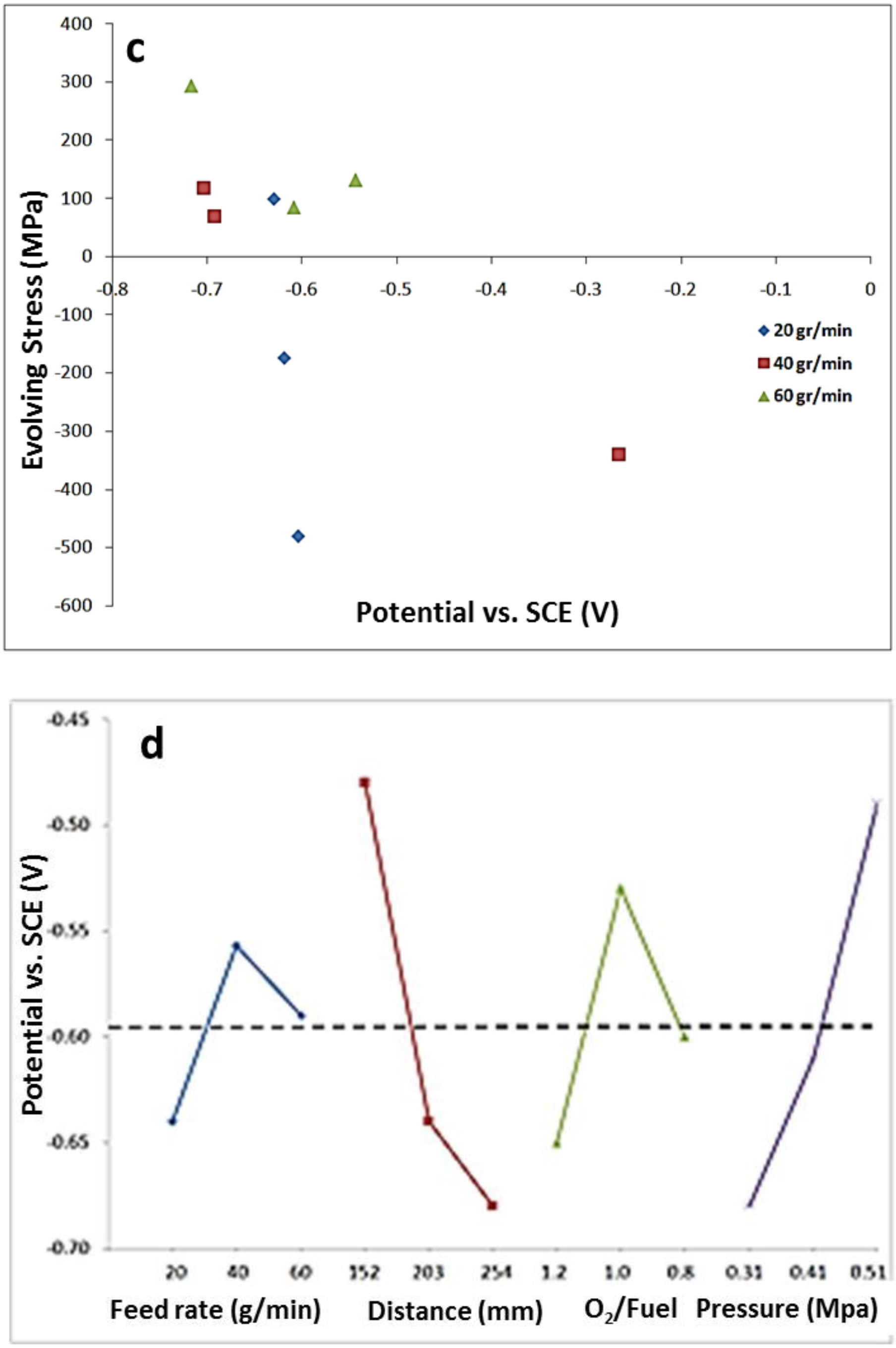
c
Evolving Stress (MPa)
400
300
200
100
0
-100
-200
-300
-400
-500
-600
-0.8
-0.7
-0.6
-0.5
-0.4
-0.3
-0.2
-0.1
0
Potential vs. SCE (V)
◆ 20 gr/min
■ 40 gr/min
▲ 60 gr/min
d
Potential vs. SCE (V)
-0.45
-0.50
-0.55
-0.60
-0.65
-0.70
20
40
60
152
203
254
1.2
1.0
0.8
0.31
0.41
0.51
Feed rate (g/min)
Distance (mm)
O2/Fuel
Pressure (Mpa)

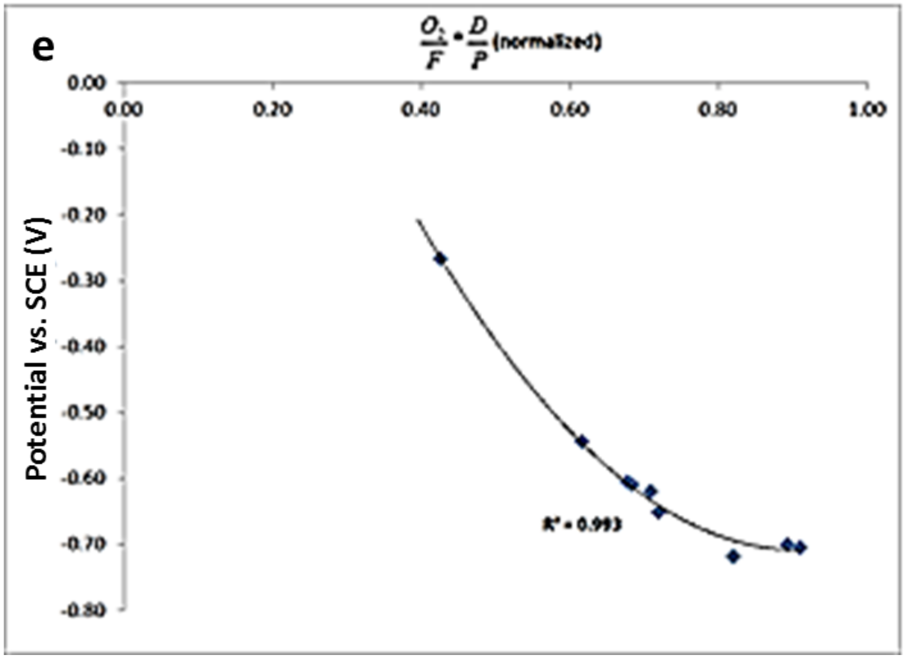

Figure 5.22: (a) The coating corrosion potential as a function of particle velocity, (b): the corrosion potential as a function of coating Young's modulus, (c) evolving stress as a function of the corrosion potential, (d) the graphical impact of each parameter level on corrosion potential (the dotted line indicates the average value) (e) the corrosion potential as a function of the process parameters, (the dots indicate experimental data).

The pitting potential (E_p) is indicative of the dissolution of the superficial protective thin oxide film which hinders ions course bi-directionally. The stability of this film is related to the Cr content in the alloy, where higher content designates increased durability in higher potentials, and hence more aggressive environments [4]. Figure 5.23a shows the correlation between E_p and particle velocity at impact. In the same graph, the repercussion of the flame environment on the corrosion potential of the coatings is clearly discernible. Coatings deposited by an oxygen rich flame show lower E_p and thus an inferior performance compared to neutral and fuel enriched flame sprayed coatings. That can be justified by Cr bonding with oxygen molecules to form oxides during spraying, resulting to its depletion in the alloy. The degree of the flame environment influence on the E_p is easily noticeable in the factors effect in Fig. 5.23b. Additionally, the oxide formation in oxygen-rich flame verifies the biased particle surface temperature during spraying. Figure 5.23c presents the description of E_p as a function of the three significant parameters. Fig. 5.23d shows that compressive stresses increase the E_p of coatings when they are sprayed at the same O_2/F ratio.

Coating c04 presented a polarization plot excessively similar to the one of the bulk Ni-20% Cr (wt.) alloy. This performance can possibly be related to extensive peening, combined with a stoichiometric flame which prevented Cr depletion. Considerable pitting was noticed on the surface of coating c04 (Fig. 24a) in polarization potentials higher than the E_p, which assisted the electrolyte to eventually reach the substrate. Following that, the current density increased rapidly (arrow, Fig. 5.21b).

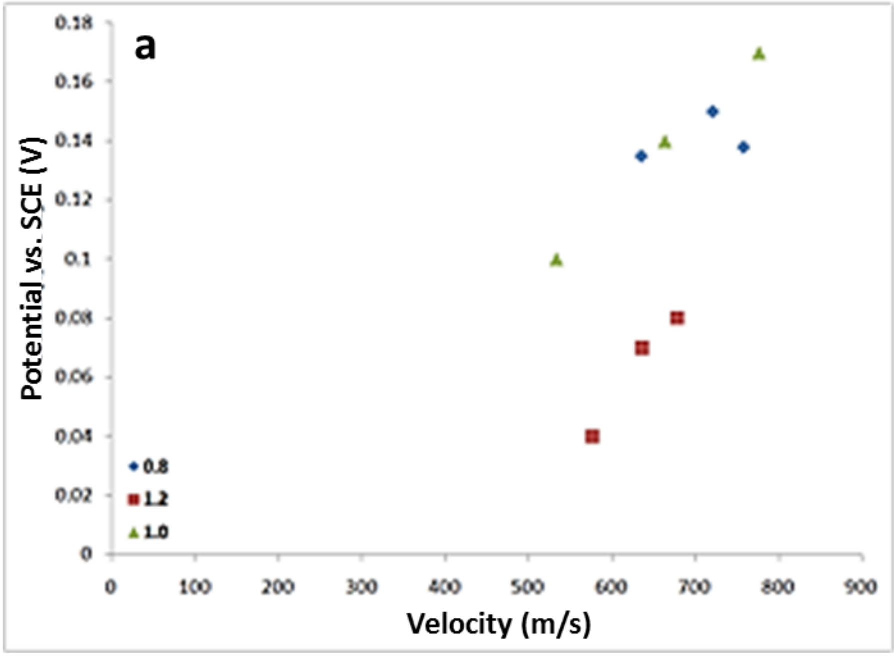

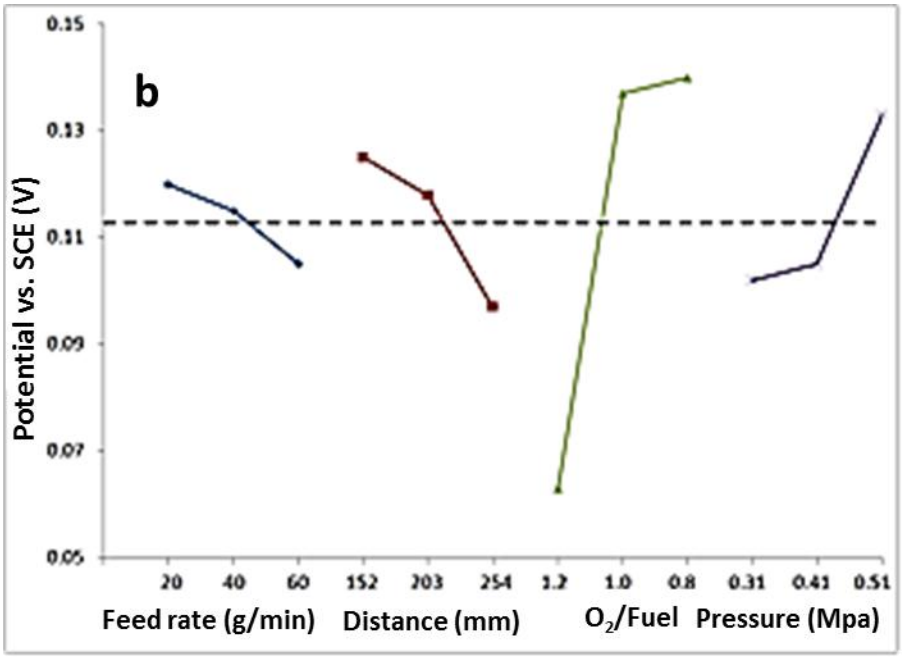
b
Potential vs. SCE (V)
0.15
0.13
0.11
0.09
0.07
0.05
20
40
60
152
203
254
1.2
1.0
0.8
0.31
0.41
0.51
Feed rate (g/min)
Distance (mm)
O2/Fuel
Pressure (Mpa)

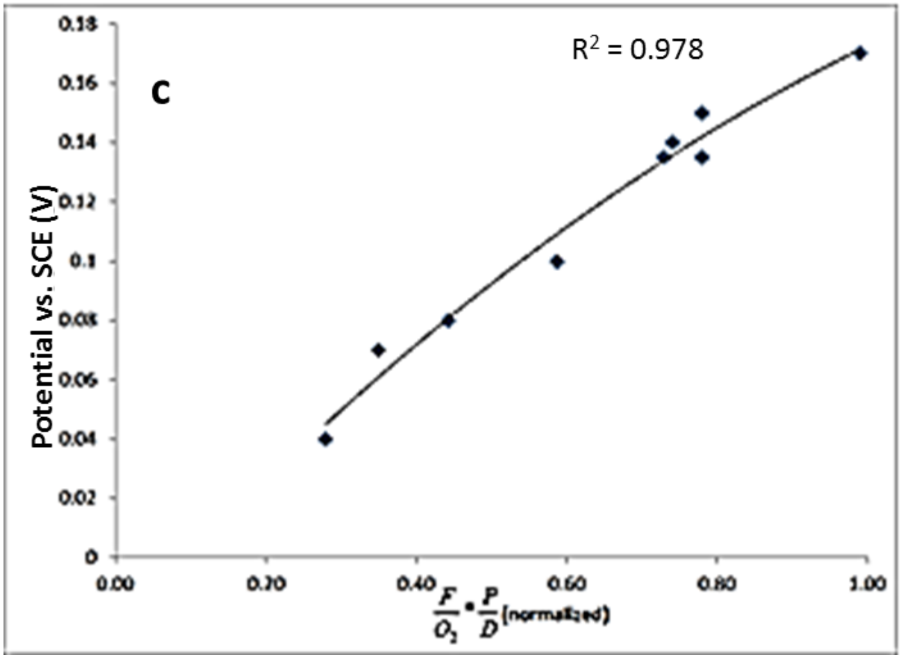
c
R2 = 0.978
Potential vs. SCE (V)
0.18
0.16
0.14
0.12
0.1
0.08
0.06
0.04
0.02
0
0.00
0.20
0.40
0.60
0.80
1.00
F/O2 • P/D (normalized)

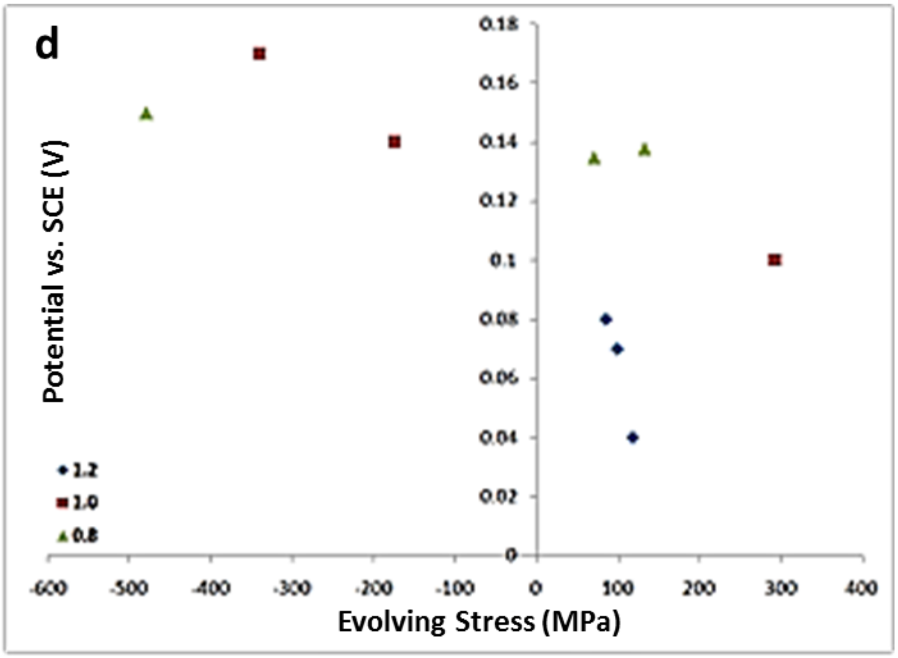

Figure 5.23: (a) The pitting potential as a function of particle velocity, (b) the graphical impact of each parameter level on breakaway potential (the dotted line indicates the average value), (c) the breakaway potential as a function of process parameters, (the dots indicate experimental data), (d) the breakaway potential as a function of evolving stress.

As modulus decreases and porosity increases, the electrolyte acquires more passages to the substrate, thus reducing the amount of pitting on the surface of the coatings. When the potential reaches E_p, limited pitting occurs on the surface (coating c07, Fig. 5. 24b), as general corrosion runs laterally. Finally, in coatings of very low E_c and high porosity, such as coating c09, oxides can be traced inside the coating (Figs. 5.24c-5.24d), suggesting extensive general corrosion of the steel substrate. The limited current density increase in potentials above E_p, confirms that. Concluding, two extreme cases can be defined in the NiCr coatings' corrosion behavior. In coatings demonstrating high E_c and low porosity, such as coating c04, the potentiodynamic plot resembles the plot of the bulk NiCr alloy, where the passive film efficiently protects the material as high as its pitting potential (E_p). On the contrary, coatings of low E_c and high porosity, such as coating c09, present a polarization plot similar to the plot of the steel substrate, suggesting its parallel widespread dissolution. The rest of the coatings presented polarization plots between these two extremes.

Decomposing the coatings' corrosion performance to spraying parameters, more corrosion resistant coatings regarding E_{corr} are deposited when sprayed at highest pressure combined with short spraying distance. Fuel rich or stoichiometric flame should be used to prevent Cr depletion and to raise the pitting potential.

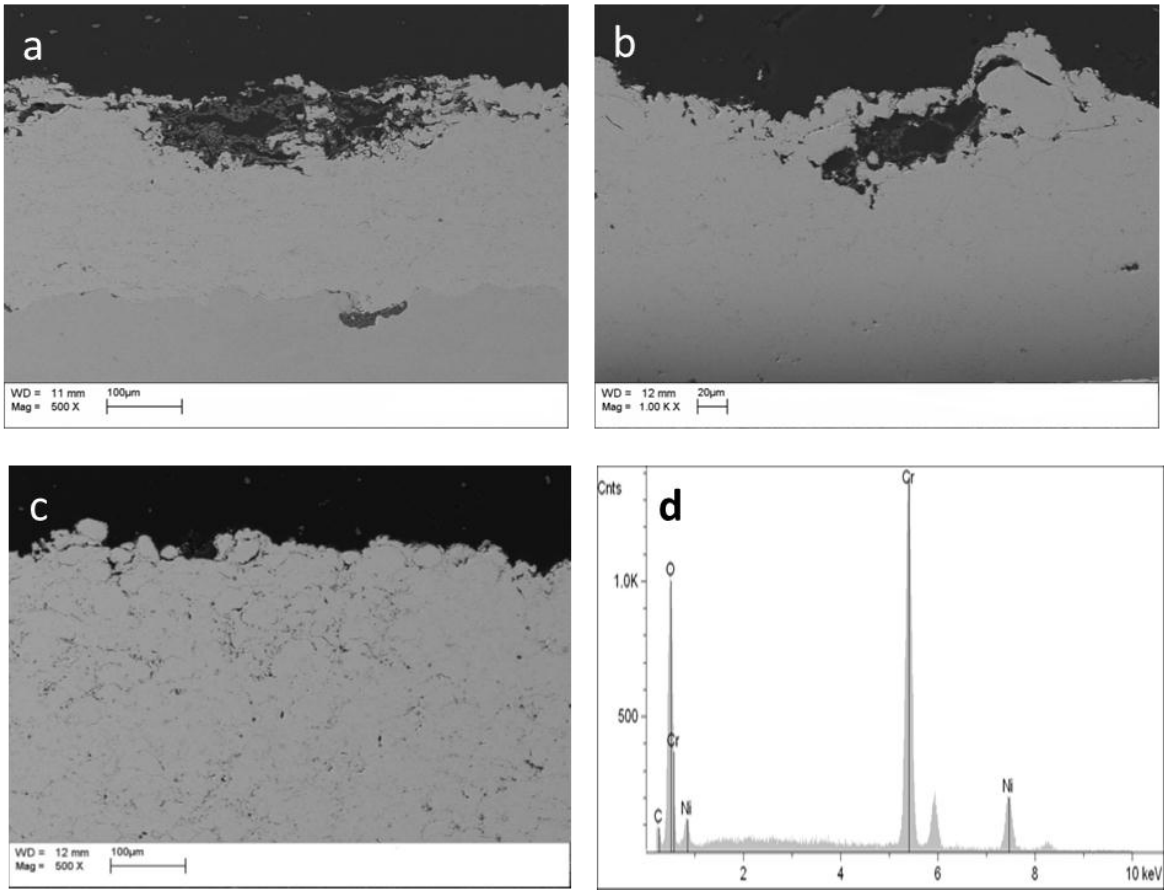

Figure 5.24: (a) Pitting corrosion in the surface of coating c04 (cross section, BSE detector), (b): pitting corrosion in the surface of coating c07 (cross section, BSE detector), (c): oxides path showing electrolyte infiltration in coating c09 (cross section, BSE detector), (d): elemental analysis of the oxide in c.

5.5 Conclusion

From the result presented, it is seen that microstructure plays dominant role in the corrosion performance of the coating which in turn is influenced by the processing parameters. The variability in corrosion potential of the coatings is related to their microstructure. A dense microstructure leads to reduced variability as seen for NiCr samples. Furthermore, APS thermal spray coatings have worst corrosion performance as is evident from the corrosion studies of the commercial Ni. The HVOF samples had better corrosion performance as compared to APS. However, even in HVOF coated TS samples variability in E_{corr} is present due to non- uniformity in the microstructure. An appropriate combination of particle velocity, temperature is necessary for corrosion resistant coating. Comparing APS and HVOF it is evident that HVOF process is suitable for depositing corrosion resistant coatings.

The conclusion from the study on the residual stress designed coating are:

1) In particle in-flight properties, combustion pressure and distance indicated the most profound impact on particle velocity, while O_2/F ratio and combustion pressure influenced particle surface temperature. Particles presented higher temperature in oxygen-rich flame suggesting extensive oxidation during spraying.

2) Evolving stresses were affected majorly by two parameters: Feed rate and combustion pressure. Combustion pressure acted as the leverage in inducing peening stress, as it majorly reflects particle velocity, while feed rate favored quenching stress, as it expresses improved intersplat contact. Over a certain powder feed rate, dominant peening in the coating was unachievable. Extensive peening stresses were still present in the coating, but they were overwhelmed by the faster increasing quenching stresses.

3) General (E_{corr}) and pitting (E_p) corrosion behavior was improved at a higher particle impinging velocity. Stress-wise, compressive coatings presented an overall better corrosion performance. The flame environment was the major factor influencing the pitting susceptibility of the deposited coatings.

Chapter 6

Corrosion Studies of Tungsten Carbide/Cobalt (WC-Co) and Tungsten Carbide/Cobalt Chrome (WC-10Co/4Cr)

6.1 Introduction

Thermally sprayed transition metals carbides (WC, TiC, Mo_2C, TaC, NbC, Cr_3C_2,), hard oxides (Al_2O_3, TiO_2, Cr_2O_3), metals (W, Mo, Ti, Ta) and their alloys (NiCr, NiCoCr, AlY) are routinely used for simultaneous corrosion and wear resistance applications [86]. For the pure carbides of the transition metals, decarburization, oxidation, thermal decomposition or phase changes due to their high melting temperature can occur at elevated temperature. Instead of depositing pure carbides, the hard carbides are embedded in easily melted, wetting and ductile metals like Co, Cr, Ni or their mixtures [86, 87].

The combination of high hardness, wear and corrosion resistance of WC and the ductility, toughness, low melting temperature of Co makes the cermet WC/Co an attractive candidate to replace hex-Cr. Convincing experiments have been conducted to validate the use of WC/Co [44]. However, degradation of WC/Co during the deposition process is observed due to decarburization of WC, W_2C, complex Co-W-C and occurrence of metallic W. This degradation has a marked effect on wear and corrosion performance and is found to be greater in the coatings deposited by APS as compared to HVOF due to their inherent flame temperature characteristics [88].

The corrosion performance of WC/Co is quite complex due to interconnected pores leading to solution penetration to the substrate and direct attack [89]. Pore architecture is one of the influential factors in controlling corrosion and it is dependent on process parameters [90]. The interconnected porosity leads to galvanic coupling between the nobler coating to the substrate which acts as an anode in this situation [87, 89]. Furthermore, in WC/Co cermets under a corrosive environment particularly acidic or static saline medium Co shows preferential oxidation and dissolution in the electrolyte as shown in figure 6.1 [87, 91, 92]. Also, investigators have reported the galvanic interaction between hard WC phase and Co where Co behaves anodically. Eventually, due to the removal of the binder near the carbide phase, the skeletal network of WC is exposed and can be removed during wear [91, 93].

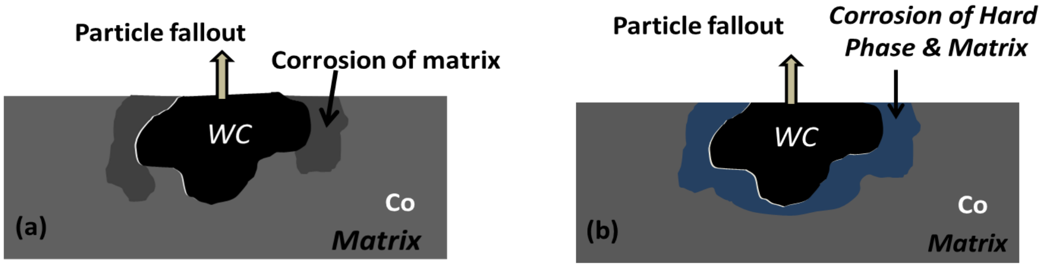

Figure 6.1: Hard carbide particle falls out due to: (a) matrix dissolution and loosening of particle. (b) Simultaneous corrosion of hard phase and matrix [94].

To improve the corrosion and wear performance of cermet coatings apart from minimizing the pore interconnectivity, the corrosion performance of binder phase is of prime importance [91]. Consequently, many investigators have replaced Co in WC/Co with Co-Cr, Ni, NiCr, Co-Ni-Cr to investigate the corrosion résistance of the coating as a whole [92, 93]. Typically, Cr addition has a marked effect in reducing the corrosion current density by forming protective surface oxide which is predominantly Cr_2O_3 layer over the coating [92].

In the present chapter carbide size and Co content on corrosion of WC-Co has been investigated. The effect of addition of Cr to WC-Co has been studied by the corrosion investigation of WC-Co/ 4%Cr. To supplement the validation of WC-Co/Cr as chrome replacing candidate the electrochemical performance of the coating deposited by carbide jet system (CJs) and diamond jet system have been thoroughly assessed. An attempt has been made to understand the impact of the process induced microstructure on the corrosion behavior of the coatings. Since the particle state has profound influence on the microstructure, in the present work, optimized temperature (T) and velocity (V) ranges of the particles have been identified which influence the microstructure and corrosion performance of the best coatings enabling production of tailored materials [55]. Furthermore, local failure of the best performing coating has been studied critically to emphasize that imperfection introduced externally or present prior to deposition has influence on the corrosion performance.

From technological and economical perspective, thickness and surface roughness of the protecting coatings is important. Mitigating corrosion by controlling thickness is a convenient technique. As the thickness increases the interconnected path become tortuous as shown in figure 6.2, making it formidable for the electrolyte to reach the substrate. Also, determination of minimum thickness for corrosion protection provides economic advantage by using expensive powder and other resources in lean manner.

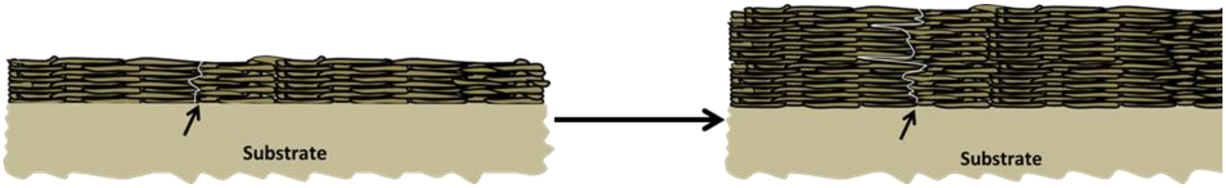

Figure 6.2: Effect of increase in thickness of coating on enhancing the tortuosity of electrolyte path.

As shown in figure 6.3, reducing the surface roughness by grinding and polishing reduces chances of pitting corrosion and also closing the pores opening towards the surface. Another, advantage of reducing surface roughness is reducing the surface contact and frictional wear. In this study minimum thickness was determined and effect of roughness on corrosion performance has been investigated.

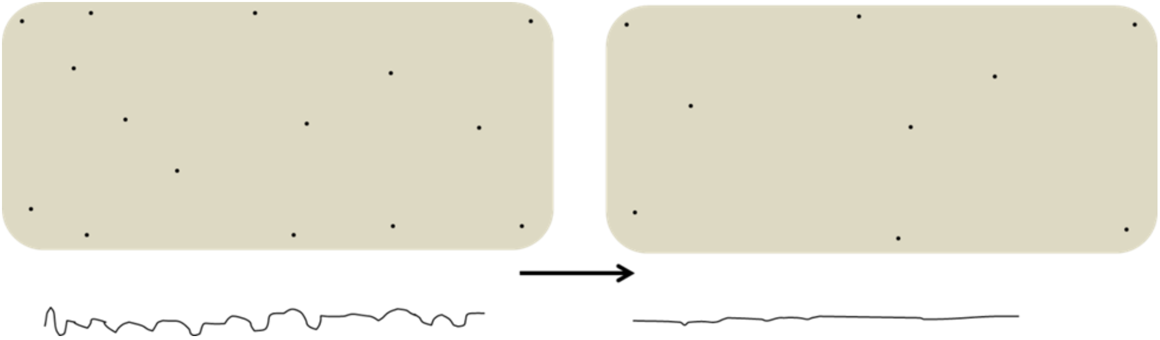

Figure 6.3: Effect of polishing on minimizing surface porosity and roughness. For rougher samples the trough acts as pitting site.

6.2 Experimental Process Description

WC-Co coatings were deposited with different carbide size and Co content as shown in Table 6.1. Co content was varied from 9% to 18%. Tungsten carbide and different Co contents were embedded in polymer matrix. On introduction in the flame, the polymer gets vaporized and only WC particles embedded in Co get deposited on the substrate.

Table 6.1: Specifications for WC-Co with different carbide size and Co content.

Sample Designation	Composition	Nominal carbide size	Mean carbide size (µm)	Oxygen ppm
WC-9CoF	**WC-9Co**	**Fine(F)**	**-**	**-**
WC-12CoF	**WC-12Co**	**Fine(F)**	**1.5**	**960**
WC-18CoM	**WC-18Co**	**Medium(M)**	**1.5**	**-**
WC-18CoF	**WC-18Co**	**Fine (F)**	**3.5**	**900**
WC-18CoC	**WC-18Co**	**Coarse (C)**	**7.6**	**520**
WC-17CoVC	**WC-17Co**	**Very coarse(VC)**	**>7.6**	**121**

WCCoCr powder was obtained from DURMAT (Durum, Germany). The deposition of WCCo-Cr was carried on carbon steel using third generation gun-Thermico Carbide Jet System (CJs) and second generation -Sulzer Metco HVOF Diamond Jet (DJ) hybrid gun. The details of the particle size, fuel rate, temperature and velocity of the particles for HVOF CJ and DJ processes are tabulated in table 6.2 and table 6.3. Prior to the deposition steel substrates were grit-blasted with 590-710 µm alumina particles at 4.5 bar pressure followed by ultrasonic cleaning in the acetone. Enough air cooling was applied to keep the substrate temperature at 150˚C during spraying. Spray Watch diagnostic device (OSEIR Ltd Finland) was used to measure particle temperature and velocity. The CJS sample are named as TG-A, TG-B and TG-C. Whereas, the DJ samples are named as SG1, SG2, and so on.

Table 6.2: Process specifications for WC-CoCr by CJS.

Sample	Particle size (µm)	Carbide size (µm)	Kerosene (slpm)	O_2 (slpm)	H_2 (slpm)	N_2 (double port) (slpm)	Powder feed	T (°C)	V (m/s)	W_2C/WC	Coating Thickness (µm)
TG-A	5-25	0.4	12	980	80	16 + 16	65	1215	783	0	190
TG-B	10-25	0.4	14	960	80	16 + 16	65	1583	766	0	280
TG-C	10-25	0.4	16	940	80	16 + 16	65	1701	746	0.06	330
T: **Temperature of particles;** V: **Velocity of particles**											

Table 6.3: Process Specification for WC-Co/Cr by DJ.

Sample	Particle size (µm)	N_2 (slpm)	H_2 (slpm)	O_2 (slpm)	Air (slpm)	Fuel/O2	T (°C)	V (m/s)	W_2C/WC	Thickness (µm)
SG1	24- 45	14	565	225	350	1.9	1633	571	0.16	125
SG2	24- 45	14	605	246	350	1.9	1643	594	0.15	
SG3	24- 45	14	635	215	350	2.2	1783	582	0.17	435
SG4	24-45	14	665	230	350	1.2	1787	598	0.14	
SG5	24- 45	14	660	192	350	2.5	1845	584	0.22	469
SG6	24- 45	14	708	210	350	2.5	1872	608	0.29	411

T: **Temperature of particles;** V: **Velocity of particles**

Figure 6.4 shows the temperature – velocity of the coatings sprayed by the two processes. For third generation process, it can be observed from table 6.2 and figure 6.4 that with increase in kerosene flow rate temperature of the particle increases whereas with increase in oxygen flow the velocity of the particles increases. For second generation process with increase in hydrogen content temperature also increased. Compared to third generation, particles of second generation have high temperature and low velocity. In third generation even though the particle were smaller in size, decarburization is nil. Whereas, in second generation process there is certain amount of decarburization.

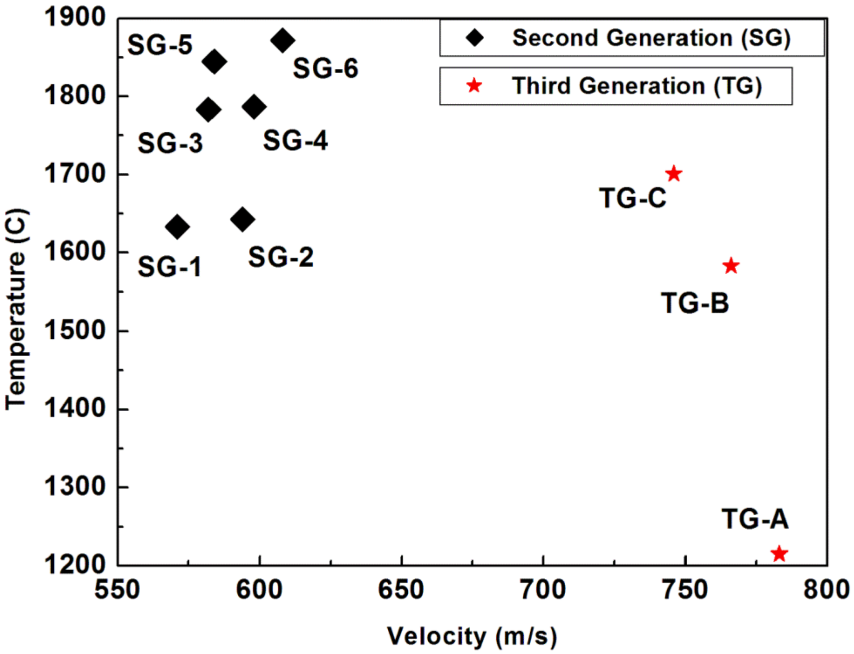

Figure 6.4: Temperature velocity range for second generation and third generation process.

6.3 Results and Discussion

6.3.1 Electrochemical Studies on WC-Co and WC-Co/Cr

Open Circuit Potential (OCP) Study

OCP scan for the WC-Co with different Co content and carbide size depicted in Figure 6.5 shows that the samples are stabilized are 12 hours. The OCP are in the range -0.500 to -0.650 V. The OCP decreases with increasing time indicating active corrosion and finally stabilization with the electrolyte. Except for WC-9CoF and WC-18CoF, the OCP value decreases with increase in Co content. OCP for the coatings decreases in the following order WC12CoF > WC17CoVC > WC-18CoM > WC-18CoC.

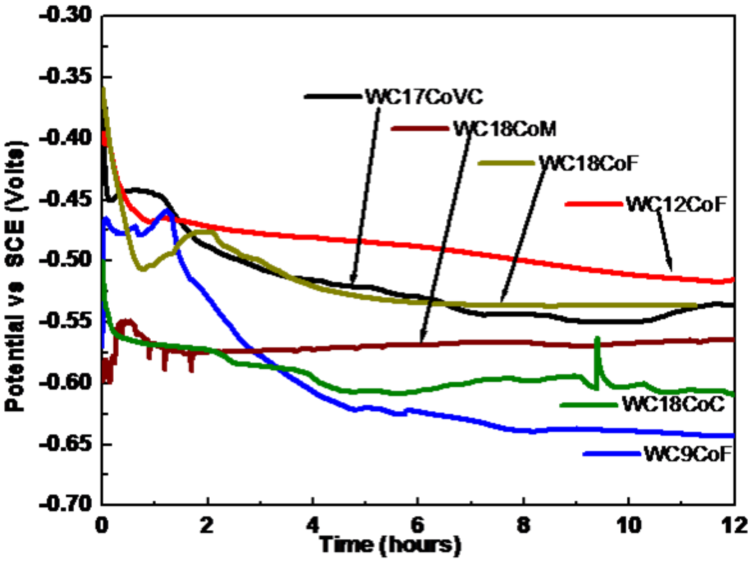

Figure 6.5: OCP for thermally sprayed WC-Co in static 3.5% neutral NaCl.

OCP (E_{oc}) versus time measurements of SG sprayed WC-Co/Cr obtained in unstirred 3.5% NaCl solution during 8 hours of their immersion is shown in figure 6.6. The E_{oc} for all the SG samples decreases with time. The final E_{oc} for SG varies between -0.434mV to -0.530 m . The E_{oc} trend for SG samples suggests that the microstructure is less dense and the decrease in E_{oc} can be associated with the presence of porosity in the coating [95]. The E_{oc} for SG-1and SG-2 remains low at all time from the beginning of immersion in the electrolyte and the E_{oc} is near to steel substrate compared to other SG sample. The E_{oc} for other SG samples SG-4 and SG -6 decreases immediately after immersion in the electrolyte. The Eoc of SG -3 decreases rapidly in the first 4 hours and thereafter the change in E_{oc} is decelerated. However, the sample SG -5 shows decrease in E_{oc} like other SG samples, but the decrease in E_{oc} is slow and is higher (-0.406 mV) at the end of 8 hours compared to the E_{oc} of other SG samples. The E_{oc} values suggest that even though all the SG samples have porosity, SG -5 might have less porosity compared to other SG samples.

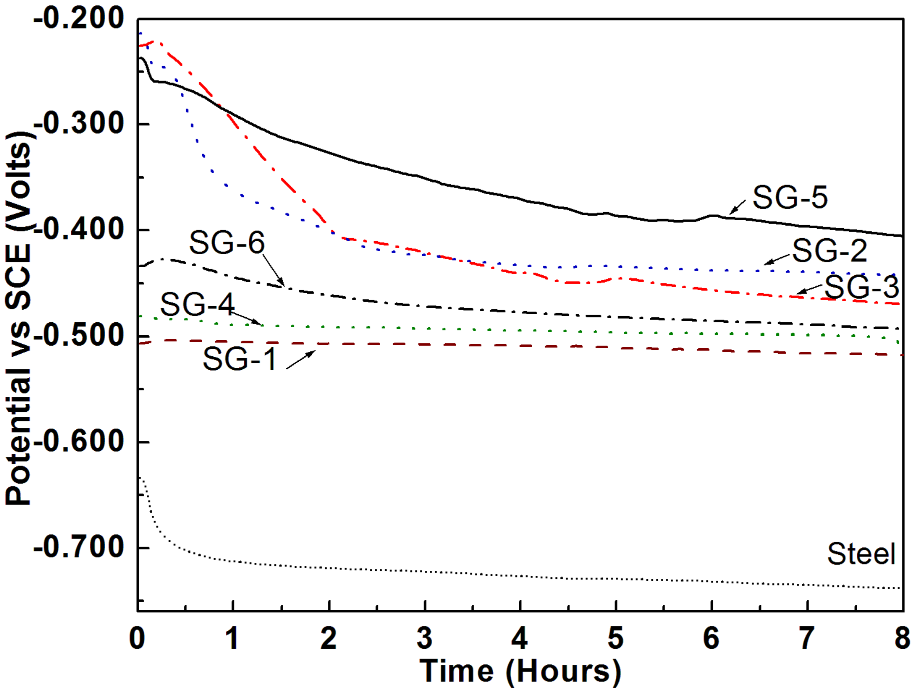

Figure 6.6: OCP (E_{oc}) for SG sprayed WC-CoCr in static 3.5% neutral NaCl.

Figure 6.7 shows the OCP (E_{oc}) versus time measurements of CJ sprayed WC-Co/Cr obtained in unstirred 3.5% NaCl solution during 12 hours of their immersion. It is observed that the E_{oc} for all the CJ samples increases rapidly in the first few hours of immersion in the NaCl solution except the B3 spot on sample B. B3 shows rapid decay in E_{oc} from -0.450 to -0.650 in first few hours and gets stabilized at -0.650 mV. Around 12 hours all the CJ samples get stabilized at ~ -0.300 mV. The rise in E_{oc} for CJs can be attributed to the formation of passive layer mainly chromium oxide during immersion. A close observation of figure 6.7 shows that the final E_{oc} for samples are in the decreasing order sample A > sample B > sample C. Furthermore, for sample C the E_{oc} first increases upto -0.275 mV and then decreases to -0.300 mV before getting stabilized. The E_{oc} measurement obtained at the spot B3 for sample B shows that the E_{oc} abruptly decreases in the initial 2 hours of immersion in the electrolyte and finally E_{oc} stabilizes at -0.650 mV which is close to E_{oc} (-0.744 mV) of bulk steel substrate. The E_{oc} measurement is because of complex events occurring and registers the potential change of the system as result of thermodynamic consideration to minimize Gibbs potential. The E_{oc} can show increasing trend and show stability due to protective oxide formation [96]. On the other hand the E_{oc} can exhibit decrease in potential as in the case of B3 of sample B.

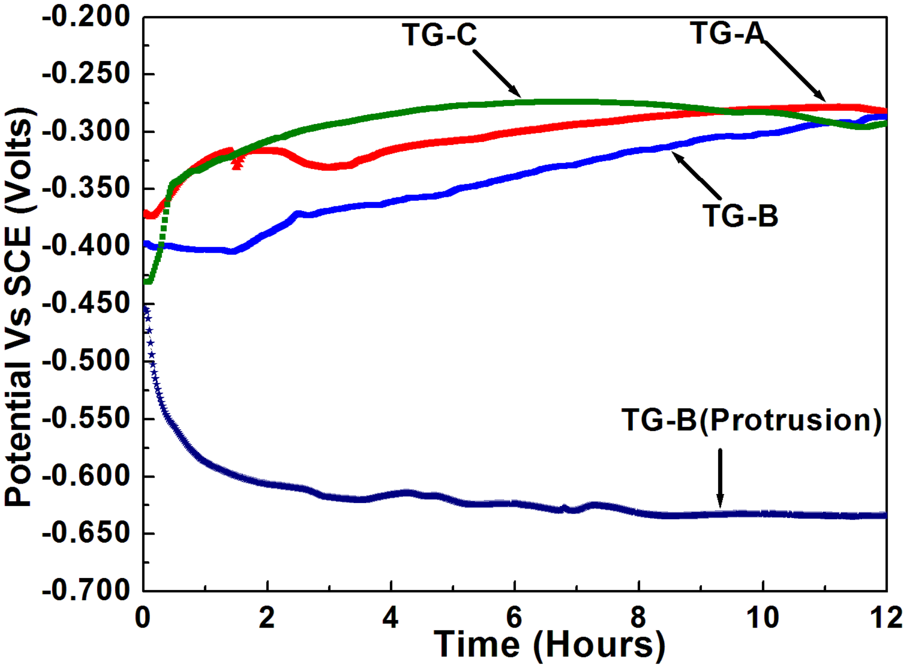

Figure 6.7: OCP (E_{oc}) for TG sprayed WC-CoCr in static 3.5% neutral NaCl.

The decrease in potential can be associated to different factors like chloride adsorption, changes in oxygen and metallic ion concentration giving rise to diffusion layers, metallic oxides formation, changes in the surface activity as the electrolyte enters the pores, galvanic corrosion as the electrolyte penetrates the coating and reaches the steel substrate [97]. The galvanic coupling so formed can result in coating detachment [98]. The drastic difference in the final E_{oc} of the different spots of sample B, B1(far from protrusion) and B3 (near protrusion), suggests that near the protrusion, the microstructure of the coating must be infiltrated with cracks and pores, and thereby facilitating easy passage of the electrolyte to the substrate. The final E_{oc} of the samples insinuates that the porosity of sample A and B must be relatively small compared to C. In sample A and sample B passive layer formed on the surface and in the pores must have resulted in extremely slow penetration of the electrolyte and hence there must have been a large delay for the contact of electrolyte with the substrate. This good performance of the sample A and B suggests that these samples have denser and homogenous microstructure due to relatively high velocity of the particles because of high oxygen flow and low temperature. On the other hand the relative low performance of sample C can be attributed to low impact velocity and high temperature resulting in relative high porous microstructure. The high temperature and low velocity of the particles resulted from high kerosene flow and low oxygen flow.

Potentiodynamic Study

The potentiodynamic studies conducted on the WCCo samples exhibits passivation in all samples except WC-9CoF as shown in figure 6.8. The passivation current ranges from 500μA to 1.3 mA. The E_{corr} for the samples ranges from – 600 mV to -750mV. Similiar to the OCP trend the E_{corr} shows decreasing trend in the order WC12CoF(-624 mV)>WC17CoVC(-645 mV)>WC-18CoM(-658 mV)>WC-18CoC(-732 mv).

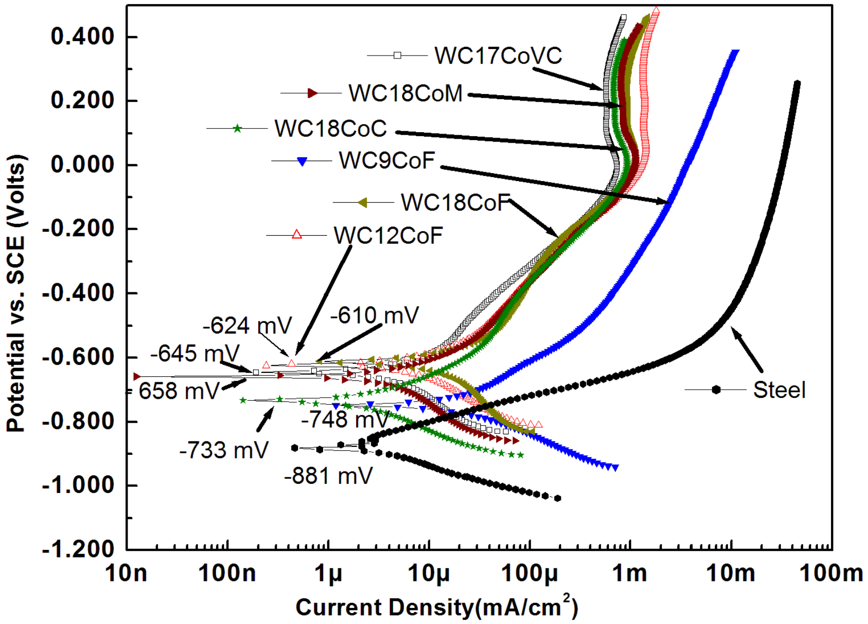

Figure 6.8: Potentio dynamic scans for Steel and WC-Co TS coatings in static 3.5% static neutral NaCl solution.

As mentioned previously, due to increase in Co content the current increases up to 0 V. After the Co particles are corroded WC-Co skeletal network remains behind and the pseudo passivation is observed. However, the pseudo passivation observed in the present study is in the range 500µA to 1.3 mA which is well below the passivation (~ 50 mA) observed by A. Human et.al [93, 96].

Figure 6.9 shows the Tafel plots for the SG samples. Figure 6.6 and figure 6.9 shows that the E_{corr} for all the SG samples are lower than their E_{oc} by -0.100 V. These coatings may perform poorly in the corrosive medium. The E_{corr} of for the SG samples are near to steel substrate. Also, it can be observed that the Tafel plots for the SG samples are situated towards higher current density. The trend of E_{corr} for SG samples is consistent with their Eoc values. It can be noticed that E_{corr} for SG-5 is highest amongst the SG samples and E_{corr} for SG- 1 and SG-6 are the lowest. The low value to E_{corr} for SG samples may be due to high porosity.

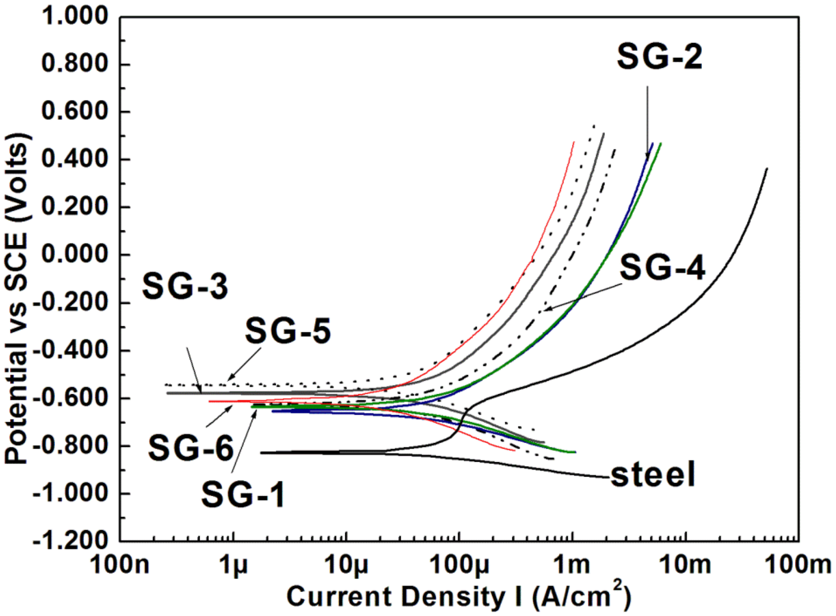

Figure 6.9: Potentio-dynamic plot for SG WC-Co/Cr in static 3.5% neutral NaCl.

From table 6.3 it can be observed that SG-1 has in addition to low temperature and velocity, has comparatively lower thickness (125 µm) than other coatings. This thickness may not be sufficient to resist the passage of electrolyte to the substrate resulting in its low corrosion performance with the corrosion potential of ~ -0.634 V. On the other hand DJ-5 has larger thickness (469 µm) and is capable to resist the passage of electrolyte. SG-3 which has thickness similar to SG-5 of ~ has similar corrosion performance with corrosion potential ~ -0.577 V. Thus thickness is found to have impact on corrosion performance of the SG coatings.

Figure 6.10 and figure 6.11 shows difference in microstructure for the SG-WCCo/Cr coatings before and after corrosion. The increase in porosity after corrosion is evident from the image is due to fall out of the hard phase particles and may be due to increase in width of pores during corrosion. The corrosion current for the SG samples are in tens of µA/cm^2. This value is typically high for WCCo/Cr system. During corrosion process there must be significant galvanic corrosion of the hard phase/ matrix which may result into the loosening of WC phase and fall out of the particles. Due to void formation pathways may have been created leading to the easy passage of the electrolyte to the substrate.

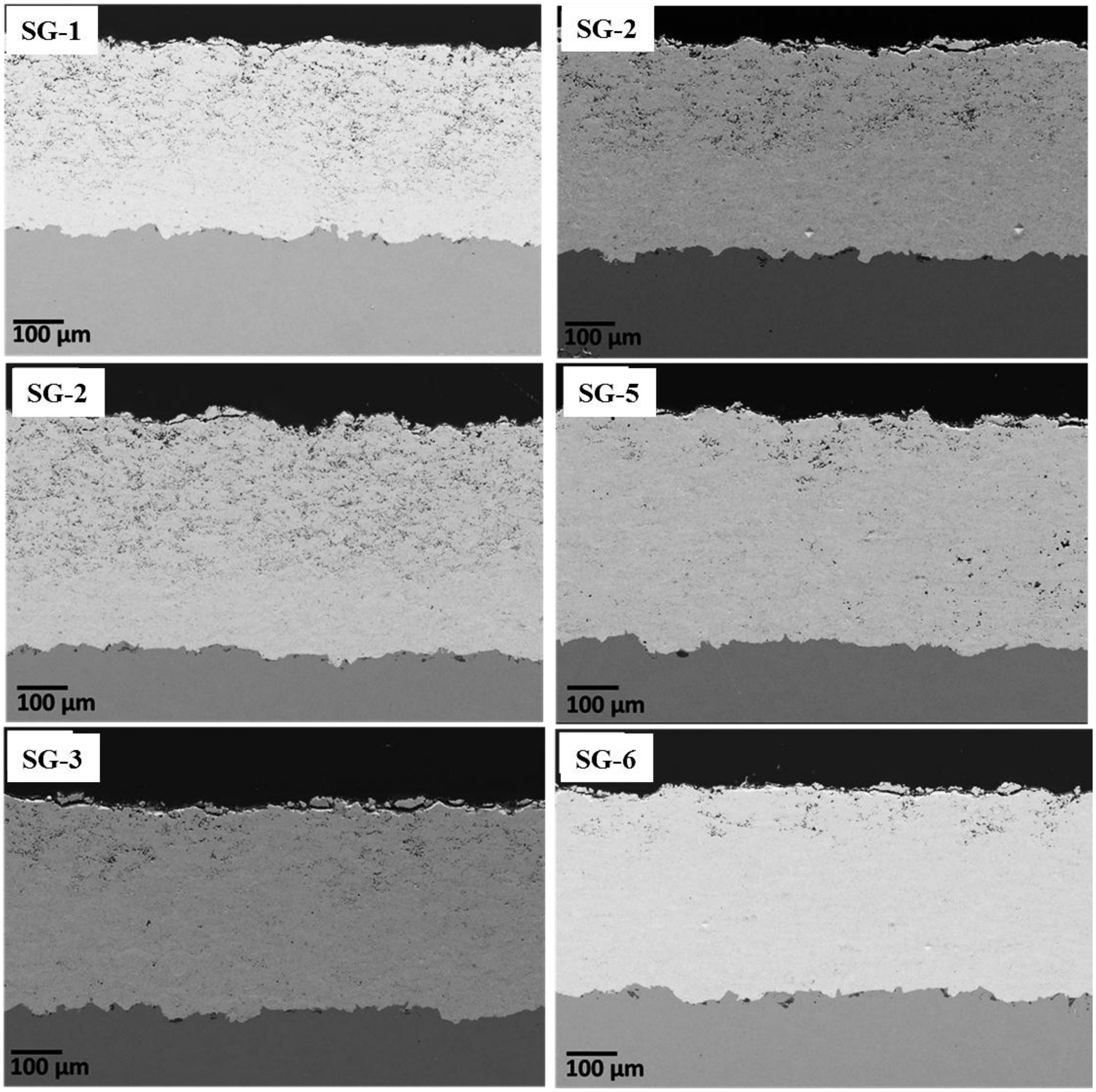

Figure 6.10: SEM image for SG WC-Co/Cr before corrosion in static 3.5% neutral NaCl.

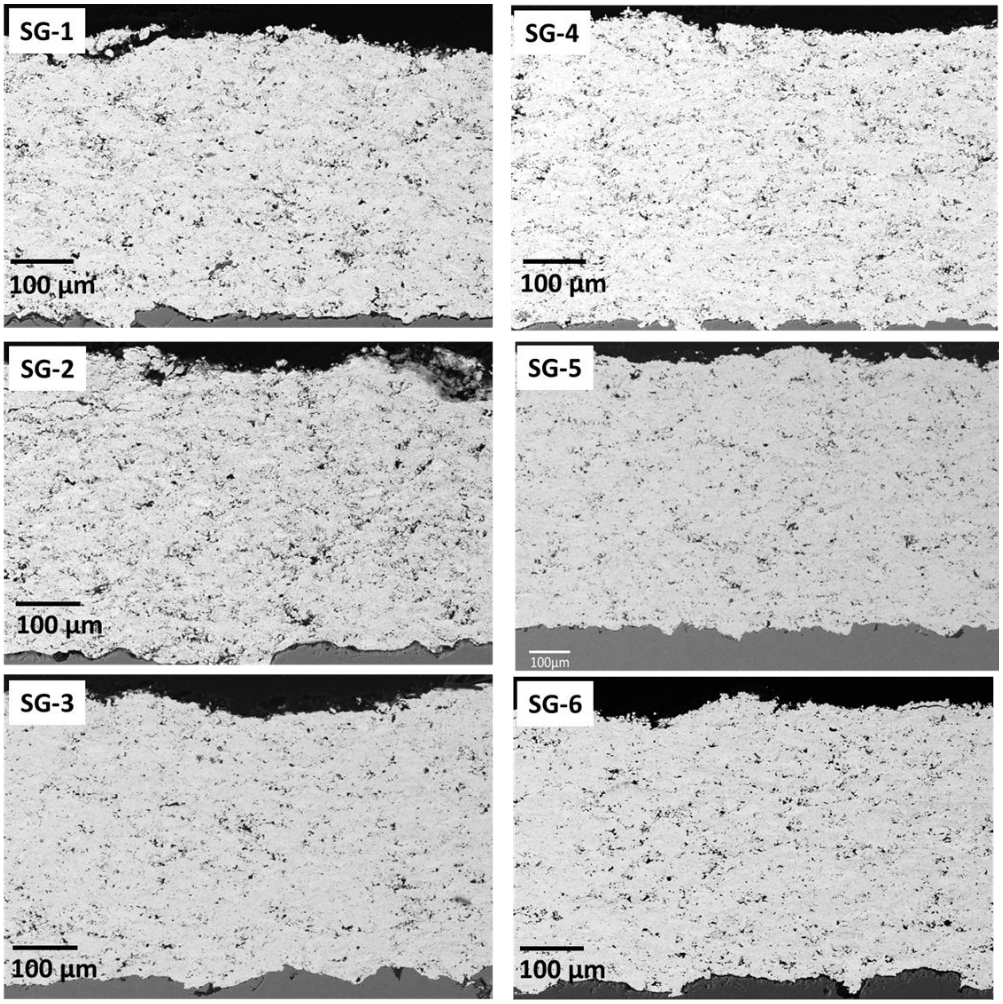

Figure 6.11: SEM image for SG WC-Co/Cr after corrosion in static 3.5% neutral NaCl.

Porosity obtained from the image analysis of SEM image of SG coatings before and after corrosion show significant amount of porosity. The corrosion current calculated by Tafel analysis show agreement with the porosity as shown in figure 6.12.

Figure 6.13 shows the potentiodynamic scan for TG samples. It can be seen from figure 6.7 and figure 6.13 that the E_{corr} of the samples are near to E_{oc}. Hence, it can be expected that these coatings would exhibit good protection from the corrosive environment [99]. However, for spot of sample B where there is protrusion, it can be observed that the E_{oc} remains quite positive for the entire immersion time and the difference being 0.175 V which remains almost constant from the third hour of immersion. Hence, this region may exhibit extremely poor or no corrosion protection to the substrate.

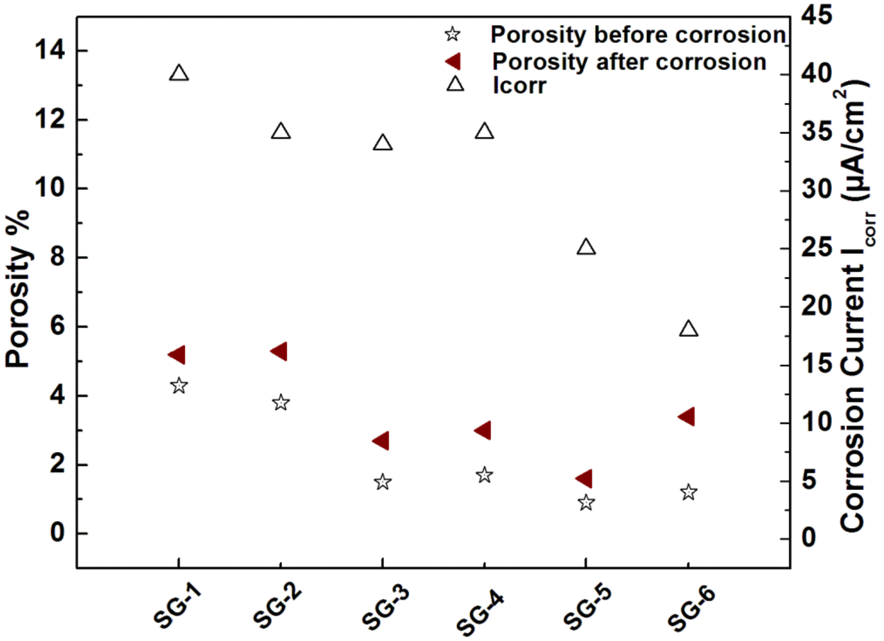

Figure 6.12: Porosity and I_{corr} for the SG coatings.

The protruded spot can undermine the corrosion performance of the coating by localized corrosion failure. Furthermore, from figure 6.13 it can be seen that the coatings show kink in the Tafel plot around 0.400 V. Protruded spot of sample TG-B (figure 6.14) shows sharp kink very near to E_{corr} similar to the steel substrate. Beyond kink which marks the breakdown potential there is sudden growth of current and marks starting of pitting. For all the samples the position of breakdown potential is comparatively higher than E_{corr} which indicates that these coating resist pitting. With further increase in voltage, around 0.500 V there is slight decrease in current and remains almost constant. This feature can be attributed to the healing behavior of Cr. Also, it can be noticed for all the sample not only the Tafel plots are present at higher potential compared to bulk steel substrate, but also the Tafel plots are displaced towards left side of the I-V space indicating that the samples have low I_{corr} compared to bulk steel. Since I_{corr} is important factor controlling the corrosion rate, it can be safely asserted that the samples have low corrosion rate compared to bulk steel.

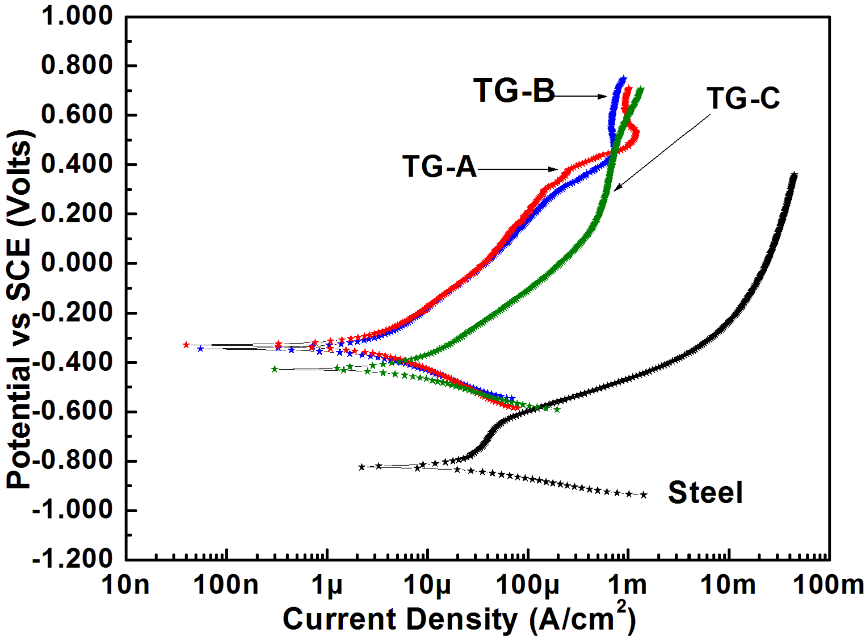

Figure 6.13: Potentio-dynamic plot for TG WC-CoCr in static 3.5% neutral NaCl.

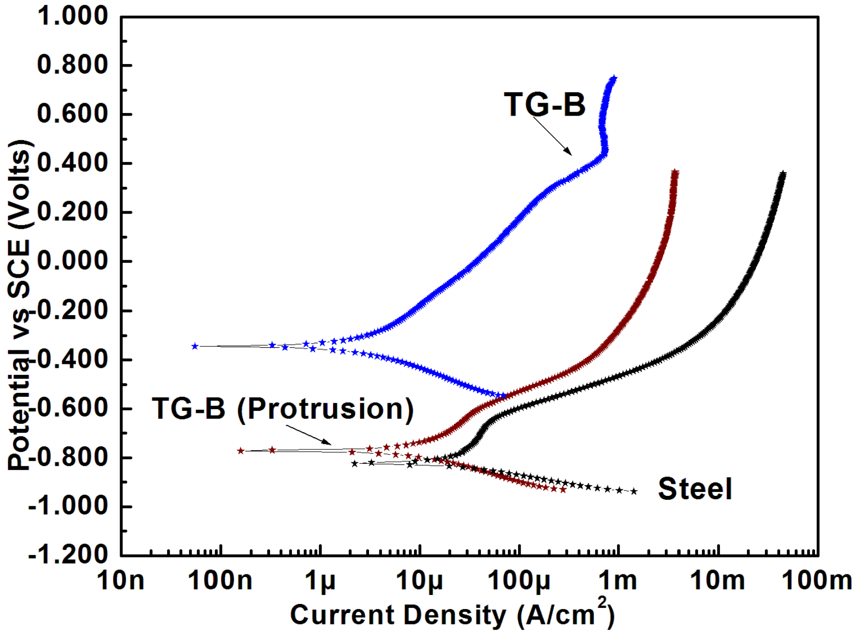

Figure 6.14: Potentiodynamic scan for sample B. The protruded region shows Ecorr near to that of steel.

Potentio-dynamic measurements for the different TG samples shows that TG-A sample has best corrosion resistance performance in the NaCl electrolyte compared to sample TG-B and sample TG-C. The average corrosion resistance performance of the samples is in the order sample TG-A (-0.300 V) > sample TG- B (-0.350 V) > sample TG-C (-0.400V). Furthermore, it can be observed from figure 6.15 that sample A shows very narrow variation in the corrosion potential, sample B excluding protruded spot has intermediate variability and sample TG-C shows maximum variability in the E_{corr}. The corrosion performance and variability in E_{corr} of the samples can be further understood from the SEM image of the TG samples. The SEM cross sectional image of figure 6.16 shows that sample A has dense microstructure and least porosity, whereas sample TG-C exhibits microstructure dispersed with pores which is comparatively higher compared to sample TG-A and sample TG-B. Table 6.3 shows that sample TG-A is deposited with highest particle velocity, sample TG-B with medium velocity and sample TG-C with low particle velocity. Difference in velocity of the particles might have resulted into differences in the porosity of the samples. Increase in velocity may increase in peening effect leading to densification in sample TG-A.

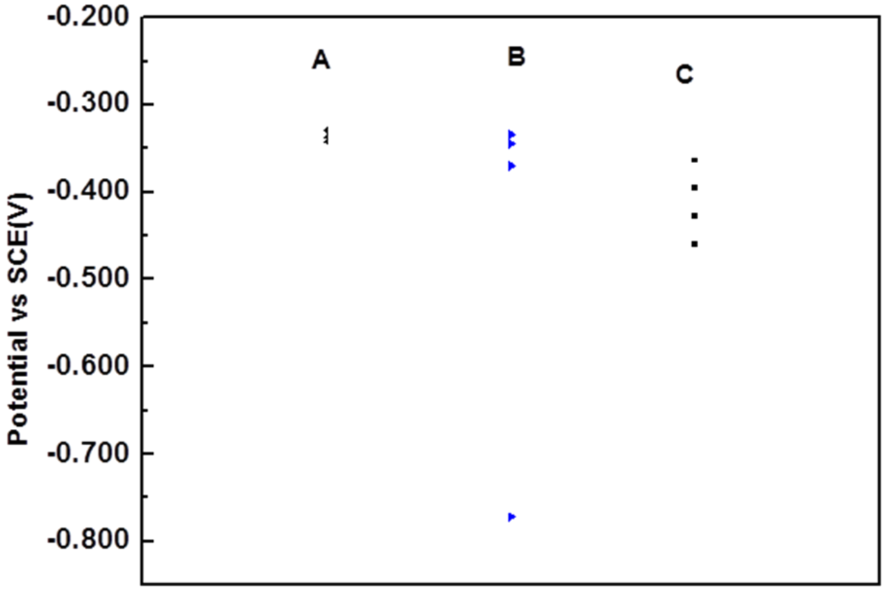

Figure 6.15: E_{corr} variation for TG sprayed WC-Co/Cr. Sample A shows least , sample TG-B shows medium and sample TG- C shows wide variability in E_{corr}.

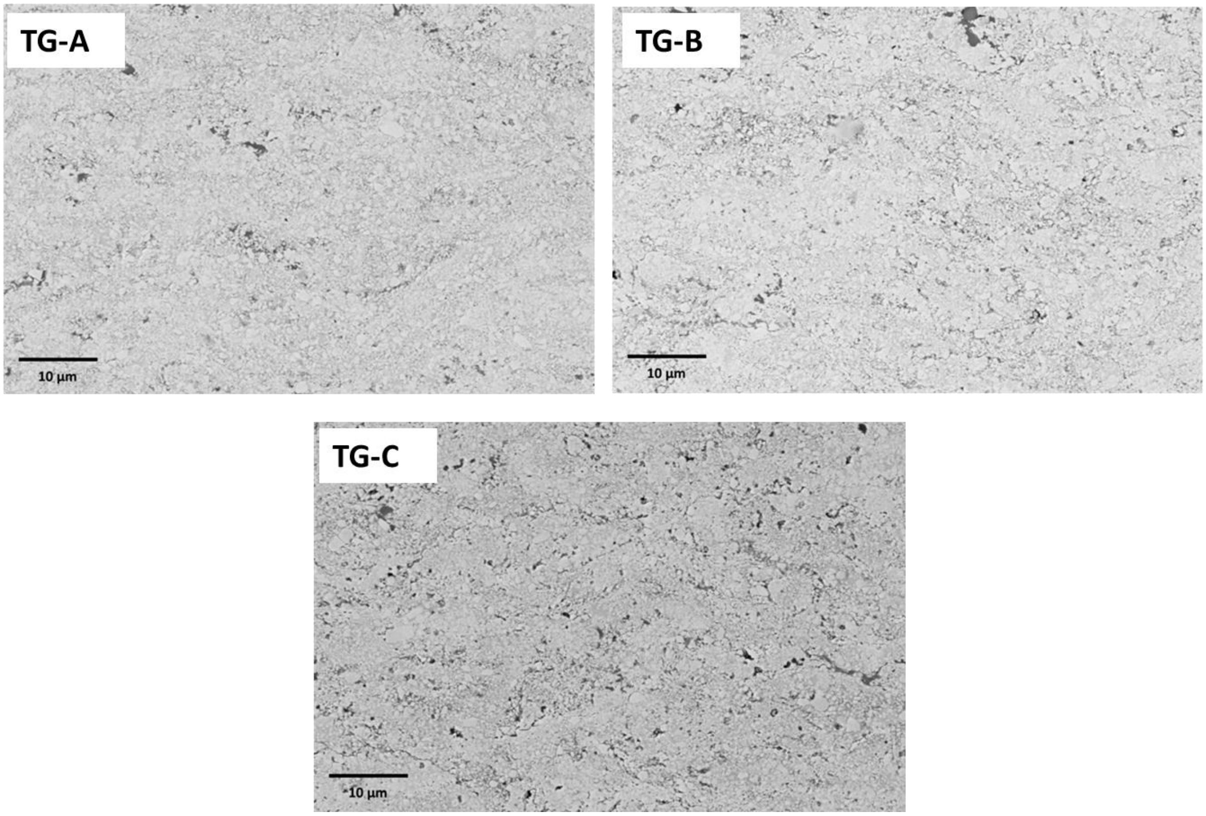

Figure 6.16: SEM image of TG WCCoCr. Image “TG-C” has large porosity compared to image TG-A and image TG-B.

Porosity of the TG coatings as shown in figure 6,17 show low level of porosity which is unchanged before and after corrosion. Also, the corrosion current obtained by Tafel analysis show small corrosion current for all the coatings.

Potentio-dynamic measurement conducted at protruded spot of TG-B shows that the E_{corr} is about -0.750 V which is close to E_{corr} of steel substrate (-0.827 V). Figure 6.18 shows the SEM image of the protrusion spot of sample TG-B. It can be observed that there is vast difference in microstructure at the protrusion and remaining of the coating. The microstructure near the protrusion shows a large number of cracks and pores which facilitate the substrate to be reached by the electrolyte. Also, it can be seen that coating is not uniformly present over the protrusion. There exist a gap between the protrusion and substrate.

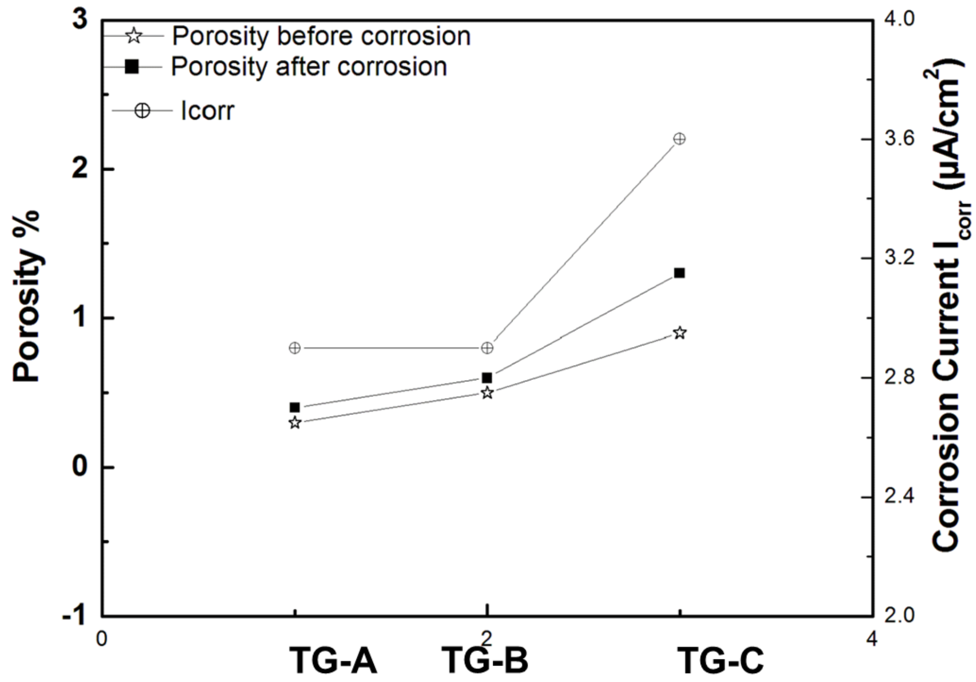

Figure 6.17: Porosity and I_{corr} for the TG coatings.

A tenacious coating layer can be seen on the substrate immediately below the protrusion. Protrusion may be extraneous and must have got deposited during spraying. During corrosion event crevice corrosion must have contributed leading to the diminished corrosion performance. A closer look of the protrusion reveals that the coating microstructures present at the top of the protrusion is similar to the microstructure away from the protrusion. The porous microstructure near the slanting portion of the protrusion is due to the fact that the angle between normal to the surface at each point of the protrusion and momentum of the particles changes.

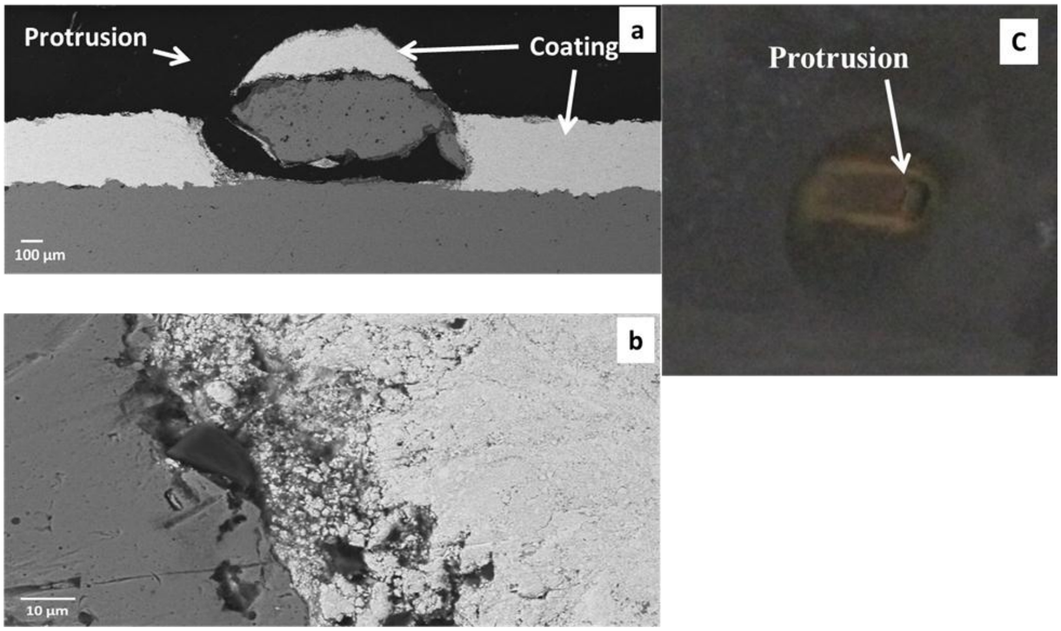

Figure 6.18: SEM image of protruded spot of sample TG-B showing (a) protrusion with coating discontinuity (b) region near to protrusion depicting pores and cracks leading to local corrosion failure. The arrows indicate crack direction. (C) Optical image of the protrusion on the surface.

Figure 6.19 shows the schematic of the impact of particles with a protrusion on the surface of a substrate along with the definition of normal (V_N) and tangential component (V_T) of velocity and impact angle (α; $0° < \alpha \leq 90°$). At different angles of impact $\alpha_1 > \alpha_2 > \alpha_3$ the normal component of velocity (V_N) is decreased in the order $V\sin\alpha_1 > V\sin\alpha_2 > V\sin\alpha_3$. Consequently, the momentum is reduced with reduction in impact angle and the peening effect is reduced at slanting edge which reduces compressive stress and leads to increased porosity in the vicinity of the protrusion and the mechanism is described in [100, 101]. The lower spray angle at the falling edge of protrusion induces porosity by another mechanism called shadowing or shielding mechanism discussed by Tillman et al [102]. Furthermore, minute cracks are seen to run throughout the microstructure near the protrusion. One of the big cracks marked by the arrows is seen to run longitudinally and finally merging with perpendicular crack. This indicates the presence of high tensile stress near the protrusion.

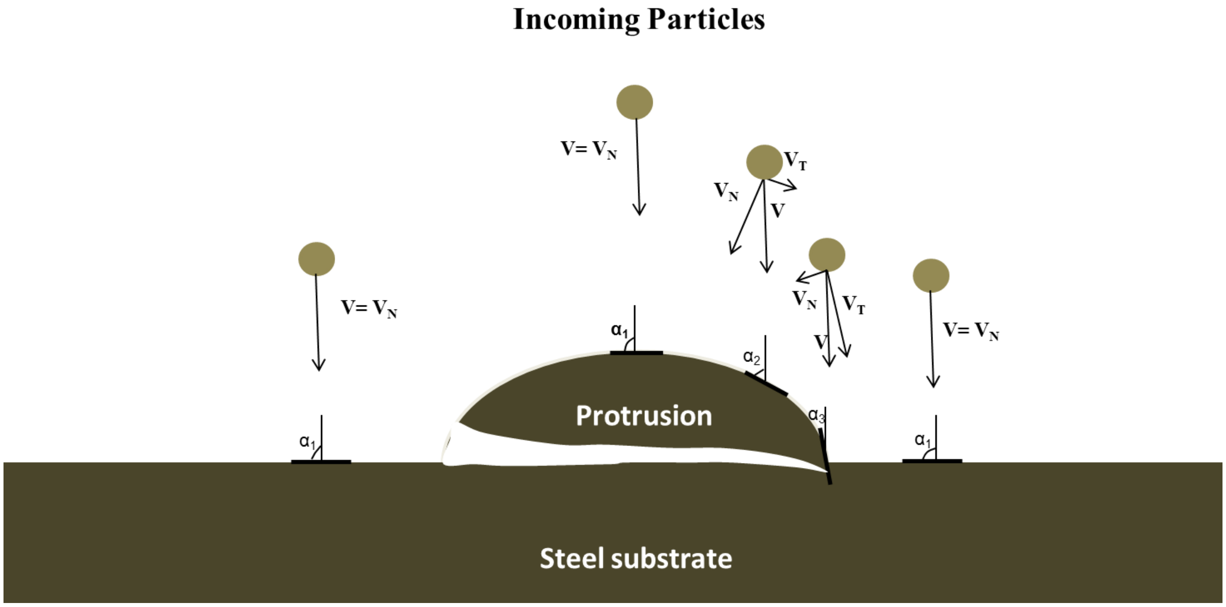

Figure 6.19: Schematic of the incident particle on substrate with protrusion. Various points on the protrusion present different off spray angle and normal angle during particle impact. V, V_N, V_T and α, are velocity of the particle, normal component, tangential component of velocity and impact angle respectively. Length of arrow indicates the dominant component of velocity.

Figure 6.20 presents the variation of porosity and corrosion current of the TG and SG coatings. It can be observed that for TG there is no significant difference in porosity for corroded and un-corroded region indicating the coating integrity against corrosion resistance. Only, protruded spot of TG-B shows highest porosity due to reasons explained previously. TG samples exhibit large difference in porosity before and after corrosion. Furthermore, it can be noticed that the corrosion current for TG is approximately 8 to 20 times that of SG. In addition to porosity measurement, the high I_{corr} for SG corroborates that the coating has interconnected pores, microcracks between lamellae leading to the passage of electrolyte to the substrate and causing heavy corrosion of the substrate. In the case of SG the I_{corr} is found to be more than the steel substrate. Such high corrosion current may be result of galvanic corrosion of substrate and coating, crevice corrosion, corrosion between hard phase and matrix. The low I_{corr} for TG samples compared to SG and steel indicates the high dense nature of the coating. The deposition conditions from table 6.2 and table 6.3 indicate that the best performing SG coatings have particle temperature less than the particle temperature of SG coatings. Furthermore the velocity of TG coatings exceeds by 200 m/s than SG coatings. Particle temperature and velocity are the most important parameter influencing the property of the HVOF coatings. High temperature leads to more oxidation and reduces corrosion performance as it is observed for SG samples. High impact velocity within critical velocity enhances plastic deformation of the particles and results into densification.

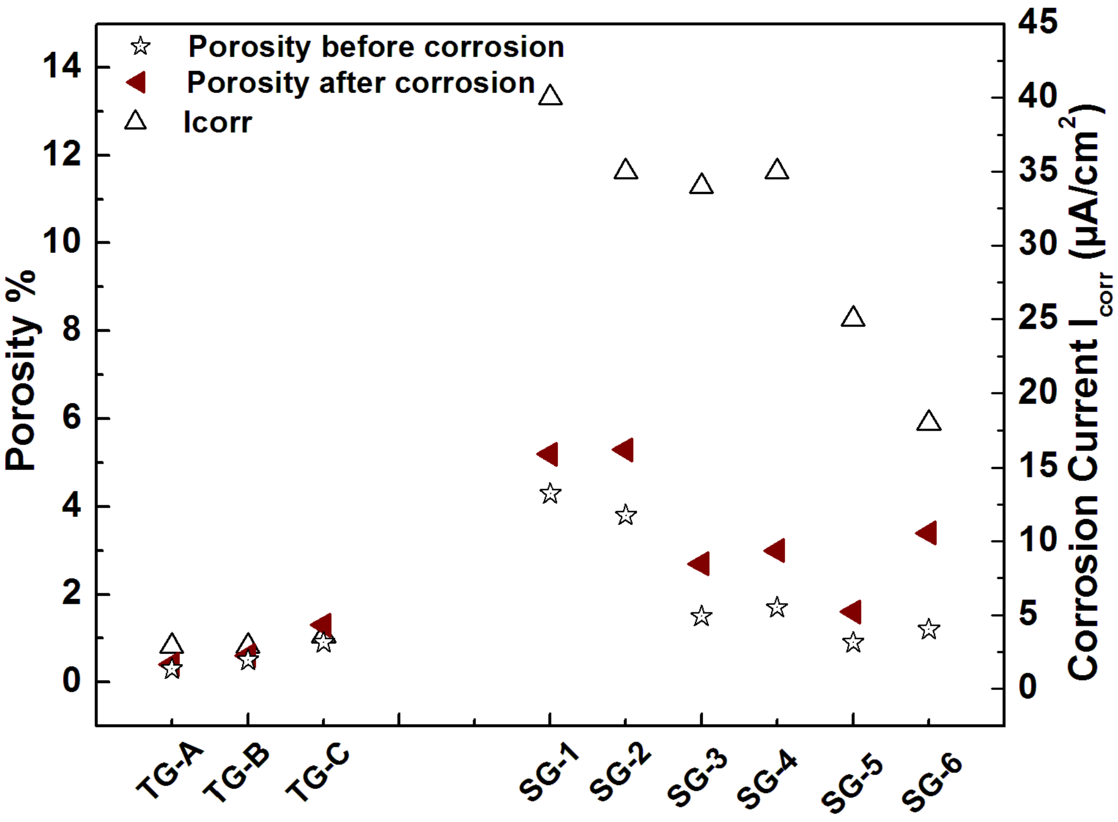

Figure 6.20: Comparision of I_{corr} and porosity between SG and TG coatings.

Figure 6.21 shows the corrosion potential of WC-Co/Cr sprayed by JK with landing gear condition, SG-second generation with gas fuel and TG-third general using liquid fuel. Also, electroplated chromium is included for benchmark purpose. As described in chapter 3 Cr shows variation in corrosion performance even though coated in same electroplating house. It can be observed that WC-Co/Cr can compete with Cr in corrosion performance by parameter optimization. TG coating outperform not only SG coating in this case but also the WC-Co/Cr sprayed by jetkote with landing gear condition. The low temperature and high velocity of TG process enables to produce coating with none decarburization indicating minimum flame particle interaction. This tends to produce coating with excellent corrosion performance.

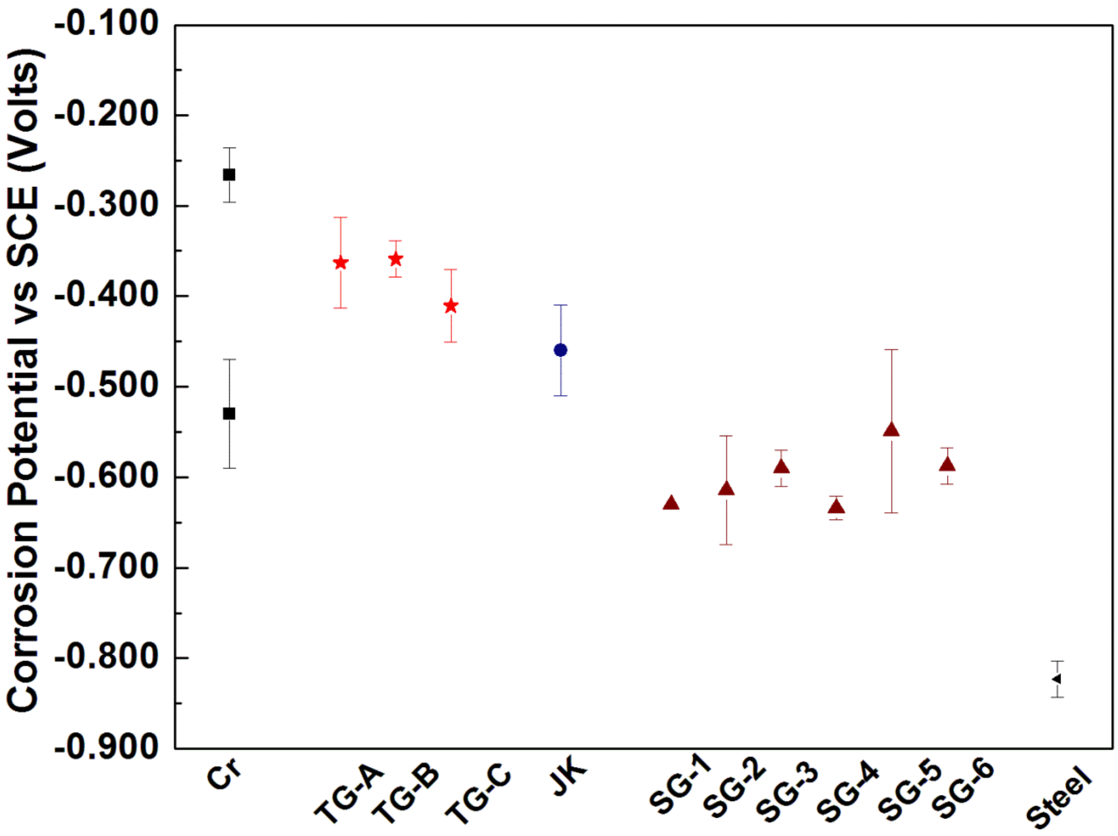

Figure 6.21: Graphical comparison of corrosion potential of third generation (TG), second generation (SG), landing gear condition Jetkote (JK) WC-Co/Cr and Cr.

6.3.2 Effect of Thickness and Surface Roughness on Corrosion Performance

Figure 6.22 shows the variation of corrosion potential with thickness and surface roughness for on as sprayed TG coating. Clearly, it can be observed that thickness has a marked difference on the corrosion performance of the coating. It can be seen from both as sprayed and polished TG samples that as the thickness is varied from 100 to 200 there is a sudden shift in corrosion potential from -0.650 to -0. 320 V towards nobler end. This observation indicates that there is minimum thickness for optimized parameters below which corrosion performance is diminished. As previously described in section 6.1 with increase in thickness the interconnected path becomes more tortuous offering more resistance for the passage of electrolyte. Furthermore, the effect of polishing (figure 6.23) is evident in that not only the corrosion potential shifts to nobler end compared to corrosion potential of as sprayed coating, but also the corrosion potential is almost constant throughout the thickness of the coating. This indicates that due to polishing most of the surface pores are closed. A similar increased in corrosion performance was observed by P. Niranatlumpong et.al for wire arc sprayed Hastelloy C-276 [103]. Also due to grinding and polishing the surface, not only the larger pores are closed but also macro surface area is reduced. With larger area the ion release rate is also increased and lower corrosion performance [104, 105]. Hence, with polishing the reduction in surface area of the coatings lead to increase in corrosion performance.

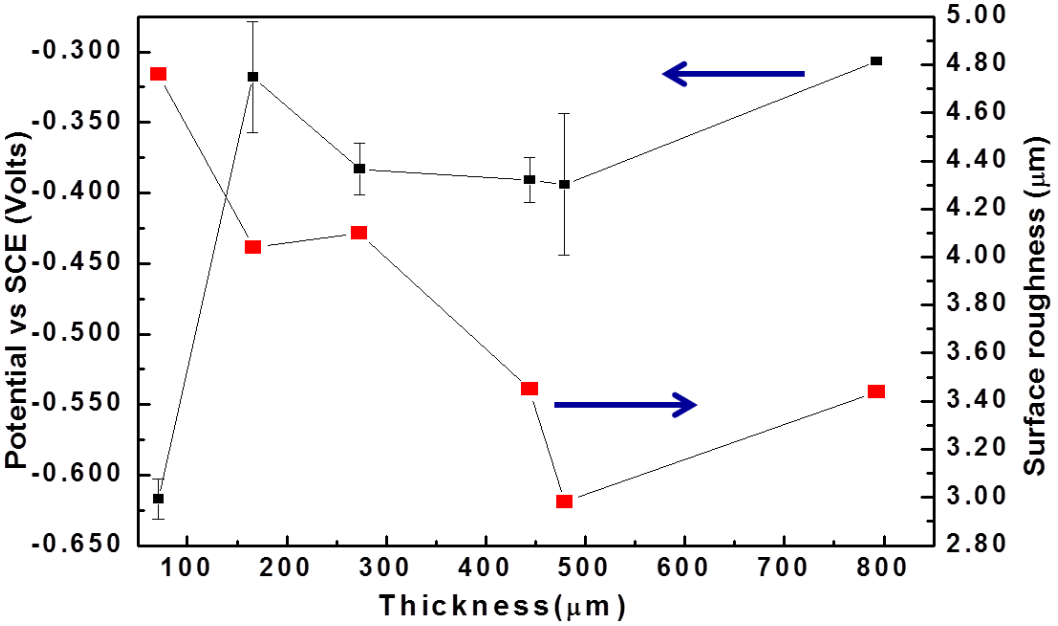

Figure 6.22: Effect of surface roughness and thickness on corrosion performance for as sprayed TG coating.

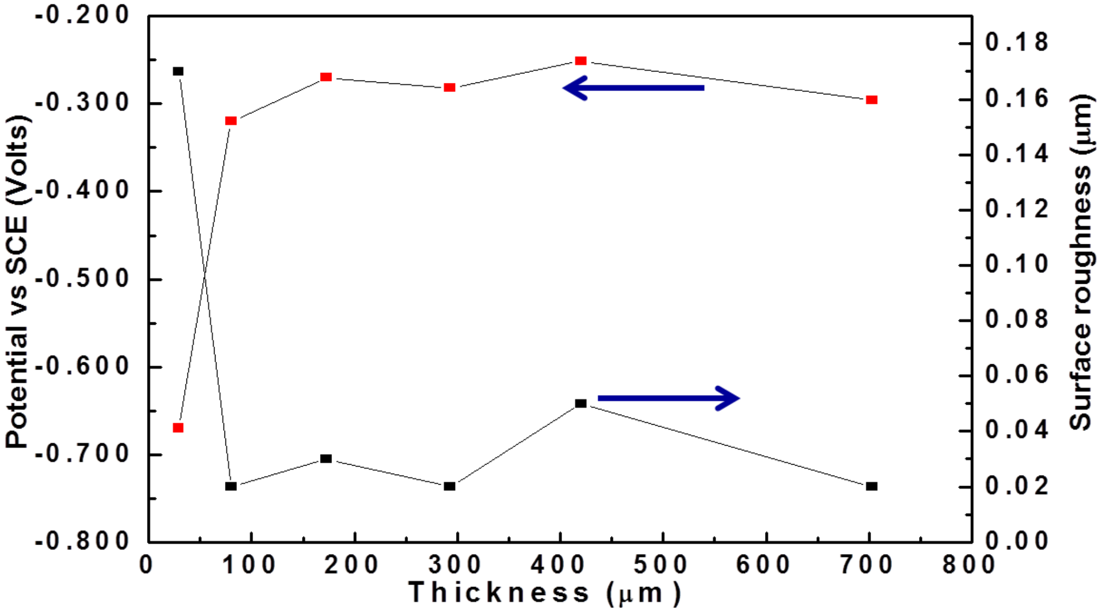

Figure 6.23: Effect of surface roughness and thickness on corrosion performance for polished TG coating.

Figure 6.24 shows the effect of temperature and velocity on E_{corr} and hardness. It can be observed that the coating TG- A and TG-B deposited at comparatively higher velocity have high corrosion potential and hardness. At higher velocity the particles may have undergone plastic deformation and densification with reduced porosity. This factor contributes to higher hardness and higher corrosion resistance. Also, in this coating the elastic modulus is higher which indicates good cohesion between the splats and compact microstructure. The high corrosion resistance, high hardness and elastic modulus indicate well optimized parameters. Whereas TG-C which is deposited at lower velocity and higher temperature have higher porosity and lower hardness due to which the splats are not compacted or peened very well during deposition. This may be the reason because of which TG-C has lower corrosion performance. We note that the decarburization is non-existent in these coatings and assume that particle flame interaction is negligible. Hence, velocity may be playing dominant role in controlling hardness and microstructure of the coatings.

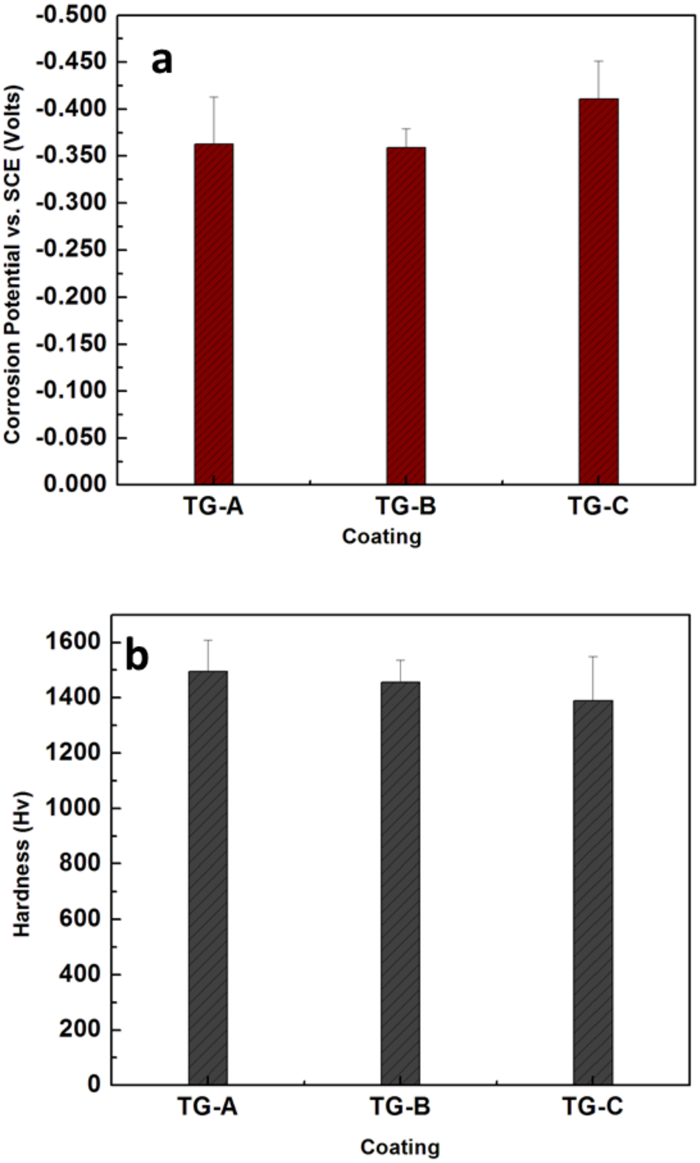
a
Corrosion Potential vs. SCE (Volts)
-0.500
-0.450
-0.400
-0.350
-0.300
-0.250
-0.200
-0.150
-0.100
-0.050
0.000
TG-A
TG-B
TG-C
Coating
b
Hardness (Hv)
1600
1400
1200
1000
800
600
400
200
0
TG-A
TG-B
TG-C
Coating

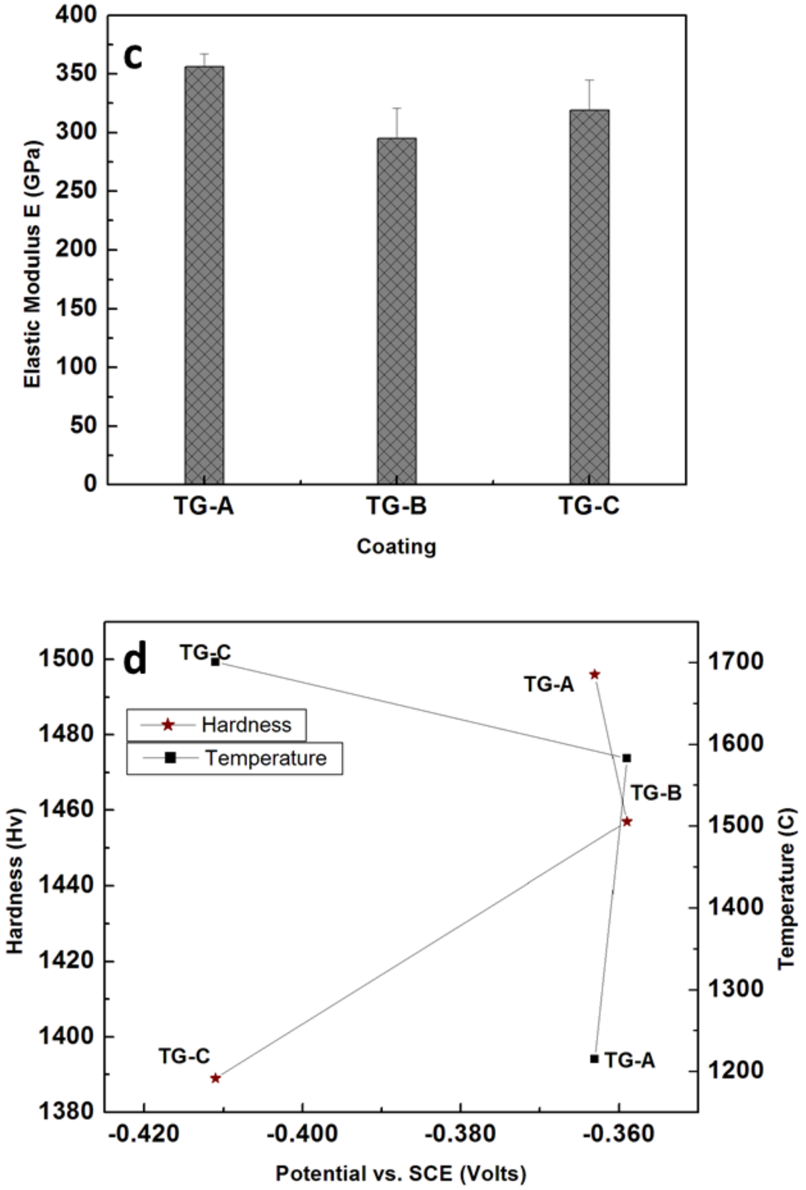
c
Elastic Modulus E (GPa)
0
50
100
150
200
250
300
350
400
TG-A
TG-B
TG-C
Coating
d
Hardness
Temperature
Hardness (Hv)
1380
1400
1420
1440
1460
1480
1500
Temperature (C)
1200
1300
1400
1500
1600
1700
-0.420
-0.400
-0.380
-0.360
Potential vs. SCE (Volts)
TG-C
TG-A
TG-B
TG-C
TG-A

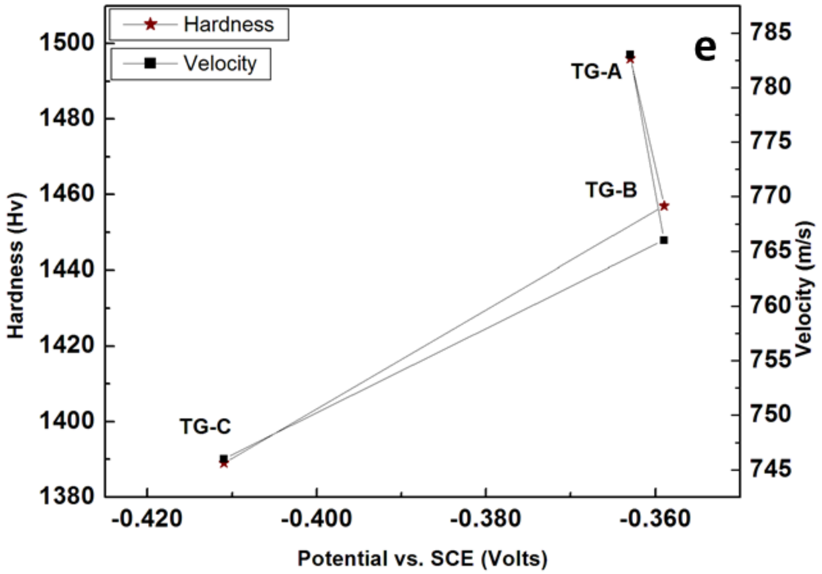

Figure 6.24: (a-c) Graphical schematic of TG coating property and corrosion performance. (d) Effect of temperature on E_{corr} and (e) Effect of velocity on hardness and E_{corr}.

6.4 Conclusion

From the study of WC-Co and WC-Co/Cr it can be concluded

1) Increase in Co content decreases corrosion resistance as WC is nobler compared to Co.
2) With fall of Co from the microstructure during corrosion, coatings exhibit pseudo passivation.
3) Addition of Cr to WC-Co improves corrosion resistance.
4) Low temperature and high velocity for TG coating produce coatings with higher corrosion resistance and narrower variability in corrosion potential.
5) Compared to SG, TG show better corrosion performance.
6) By fine tuning of parameters corrosion performance of WC-Co/Cr can match the performance of Cr.

Also, thickness and surface roughness are important criteria for corrosion performance. There is minimum thickness for optimized parameters above which coatings exhibit better corrosion performance due to increase in tortuous path with increase in thickness. Surface polishing decreases the probability of pitting by surface leveling and close of surface pores.

Chapter 7

Corrosion Studies of Chrome Carbide Nickel Chrome ($75\%Cr_3C_2$- 25%NiCr)

7.1 Introduction

In the last chapter corrosion performance, variability and process parameter impact on corrosion was discussed for WC-Co/Cr was discussed. WC-Co/Cr has high wear resistance and has wide wear applications. However, the maximum high temperature for WC based applications is 450° C [106, 107]. At high temperature where chemical stability is required CrC- NiCr has been extensively used to minimize corrosion and wear [27, 69, 108]. Moreover CrC-NiCr is cheaper and lighter than WC-CoCr. Consequently, corrosion study of CrC-NiCr is beneficial to ascertain its role as a candidate for hexavalent chromium replacement. In this chapter impact of processing on corrosion of CrC-NiCr is described.

7.2 Experimental Process Description

CrC-NiCr was obtained from Globaltungsten products inc, USA**.** JP5000 was used to spray the powder on 1018 steel substrate with dimensions of 223 mm x 25.4 mm x 1.4 mm. Prior to spray, all the substrate were cleaned by acetone and then grit blasted using 60 micron alumina grit with pressure of 55 – 60 psi. Table 7.1 describes the experimental parameters used during spraying of the powder. Accuraspray was used to measure particle temperature and velocity.

Table 7.1: Process specifications for CrC-NiCr by JP5000.

Sample	Feed rate gm/min	Distance /inches	O_2/ Fuel	Total flow (gal/slph)	Velocity (m/s)	Temperature (C)	Thickness Before (µm)	Thickness After (µm)
JP-1	65	16	1.25	8 (4.4/1220)	339	2174	160.0	107.9
JP-2	65	16	1.00	8 (4/1100)	354	2118	260.0	243.8
JP-3	65	16	0.75	8 (3.5/960)	355	2075	150.0	133.4
JP-4	65	16	1.25	14 (7.8/2140)	585	2054	250.0	215.6
JP-5	65	16	1.00	14 (7/1925)	656	1985	260.0	242.4
JP-6	65	16	0.75	14 (6.1/1670)	665	1930	240.0	193.0

Figure 7.1 shows the temperature velocity of the particles obtained from the Accuraspray diagnostics tool. The lines in the vertical plane represent locus of points for total flow whereas line in the horizontal plane are those connecting the same oxygen to fuel ratio. It can be seen that the temperature ranges from 1930 °C to 2155° C and velocity ranges from 339 m/s to 665 m/s. Furthermore it can be seen that for same oxygen/fuel ratio velocity increases and temperature with total flow. With increase in total flow the particles gets vigorously propelled in forward direction.

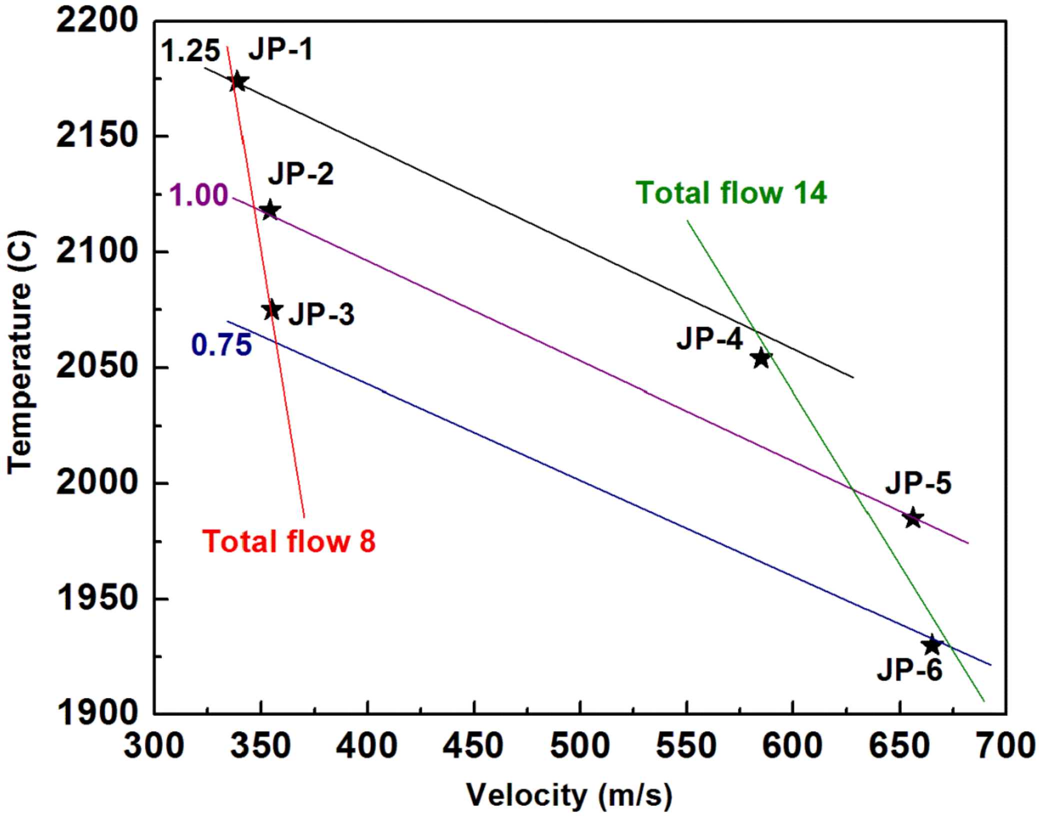

Figure 7.1: Temperature- velocity of the Cr_3C_2-NiCr particles.

7.3 Process Impact on Corrosion Performance

In this section impact of various process parameters on corrosion performance is described.

7.3.1 Impact of Velocity on Corrosion Potential

Figure 7.2 shows the plot of corrosion potential of the coatings vs. velocity. It can be observed that with increase in velocity, corrosion potential increases. With increase in velocity kinetic energy increases in quadratic proportion with velocity. The particles on impinging the substrate may undergo plastic deformation to larger extent proportional to velocity. Hence, the coatings undergo compaction with increase in velocity. Thus dense coating is formed at high velocity.

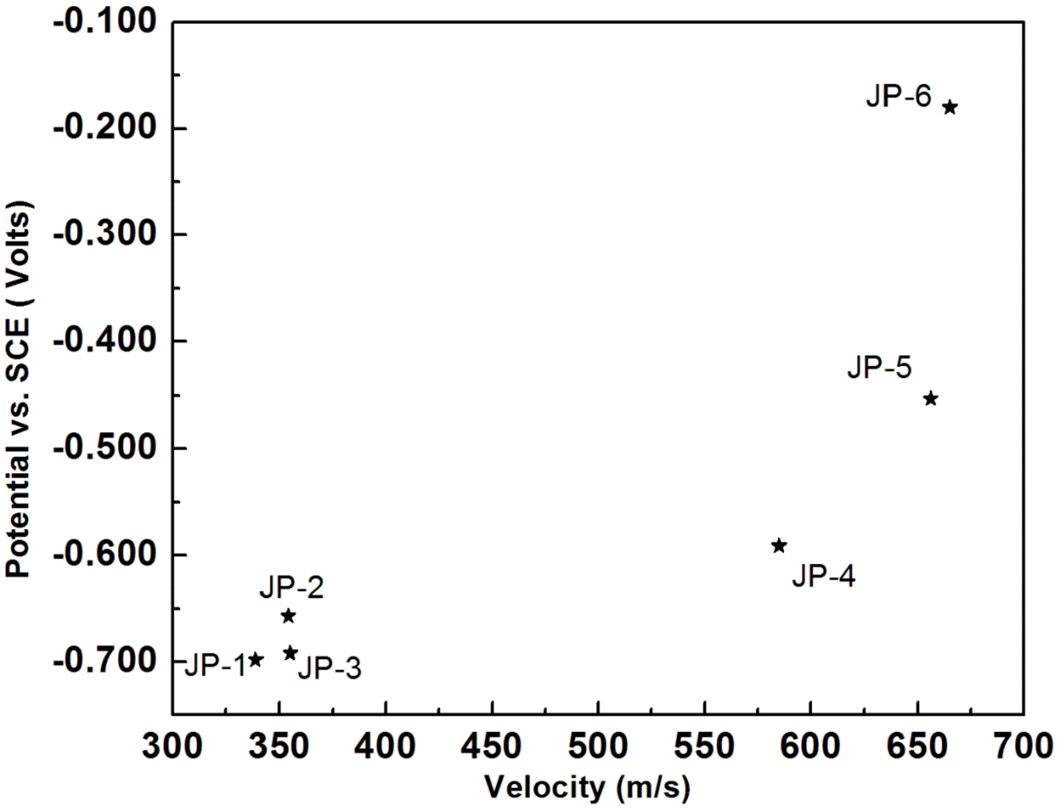

Figure 7.2: Graph of corrosion potential vs velocity.

7.3.2 Impact of Residual Stress on Corrosion Potential

Figure 7.3 illustrates the effect of Residual stress in the film on the corrosion performance of the coating. Compressive stress tends to close the interconnected pores and hence the coating offers resistance to the flow of electrolyte to the substrate. Whereas, tensile stress tends to widen pore diameter and can contribute in developing cracks which facilitate the passage of electrolyte to the substrate and diminish corrosion performance of the coating [109]. As the coating generates more compressive stress, corrosion potential increases.

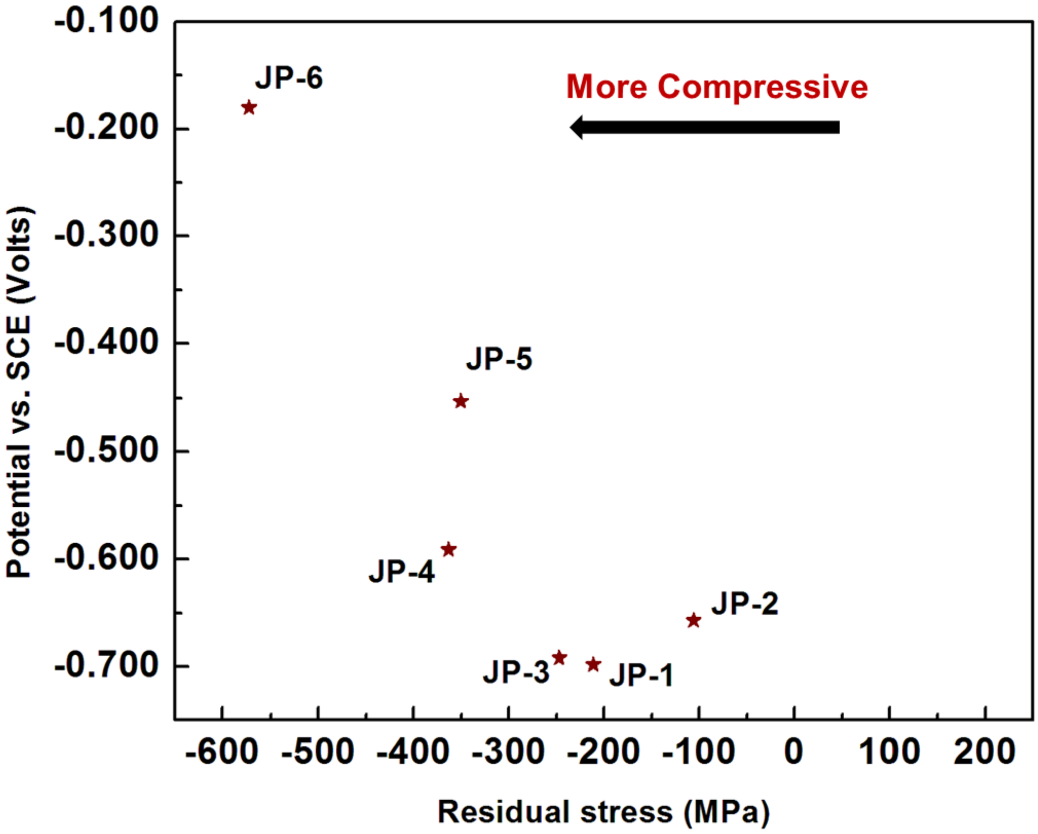

Figure 7.3: Graph of Ecorr vs. residual stress.

7.3.2 Impact of Thickness on Corrosion Potential

Figure 7.4 illustrates the effect of thickness of coating on corrosion performance of the CrC-NiCr coatings. It can be observed that the corrosion resistance does not increase monotonically with thickness. There is a upper bound to thickness beyond which corrosion resistance drastically drops. This means thickness alone is not a governing factor to control corrosion performance. From figure 7.4 it can be seen that the coating JP-2 with higher thickness was under low compressive stress. This coating had lower compressive stress compared to other coatings like JP-4, JP-% and JP-6.

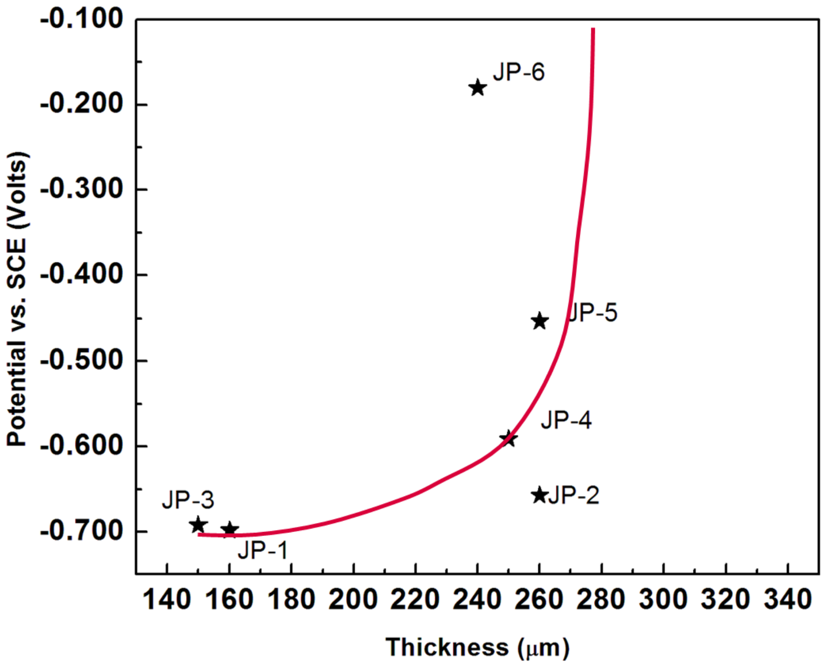

Figure 7.4: Graph illustrating impact of thickness parameter on corrosion performance. Blue circle encloses coatings with residual and lower compressive stress. The red curve shows the trend in increase of corrosion potential with thickness.

7.3.3 Impact of Processing on Microstructure and Corrosion Performance

Figure 7.5 shows the cross sectional SEM image of the Cr_3C_2-NiCr coatings. From the figure 7.2 and 7.3, the impact of processing on microstructure and hence on corrosion performance is clearly evident. From the figure it can be observed that JP-5 and JP-6 have compact microstructure with few pores. These coatings had high flow rate and comparatively high velocity. In this coating deposition was done in fuel rich condition which may have resulted into less oxidation of the particles [110]. Furthermore, these coatings were under relatively high compressive stresses which lead to narrowing pore diameter and increased corrosion performance. The high velocity resulted into peening of particles and compact microstructure.

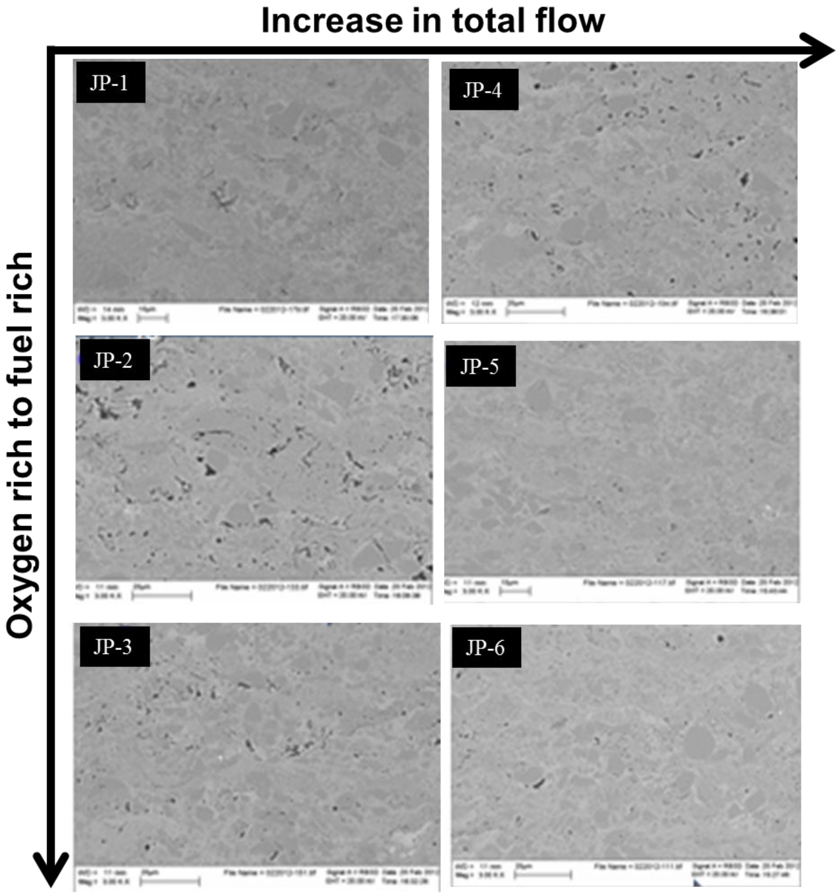

Figure 7.5: Cross sectional SEM image of CrC-NiCr coatings.

On the other hand the coatings deposited in oxygen rich condition and low velocity conditions have high porosity. At lean fuel/oxygen condition, all the oxygen is not utilized for combustion. This creates oxidizing environment which is further increased by the easier mixing of oxygen from surrounding air. Thus higher oxygen level leads to oxidation of the semi molten particles and porous microstructure. On the contrary, higher fuel creates oxygen depleted reducing flame condition resulting into less oxide content in the coating [111, 112]. Also, lower velocities for these particles are not enough to provide enough momentum for flattening. Thus at low velocity the coating microstructure is less compact.

7.4 Conclusion

The investigation of processing parameter on corrosion performance of CrC-NiCr indicates:

1) Denser and less oxidized coating require low temperature and higher velocity of the particles.
2) Coatings with higher compressive stress showed better corrosion performance due to narrowing of pores. Whereas, coatings with tensile stress showed poor corrosion performance.
3) Higher thickness leads to stochastic closing of interconnected pores. Hence corrosion performance increases with increase in thickness. However, residual stress also needs to be considered along with thickness. High coating thickness with progressively increased tensile stress leads to poor corrosion performance.
4) Reducing flame condition leads to less oxide content and dense coating.

Chapter 8

Discussion on Processing and Post Process Impact on Corrosion Performance

8.1 Introduction

This chapter discusses the various processing and post processing influence on corrosion performance of thermal spray materials investigated in previous chapters. The processing parameters considered for the investigation included feed rate, different thermal spray systems, particle state, oxygen/fuel content, total flow, thickness, addition of Cr. Furthermore, porosity present in microstructure, residual stress impact on corrosion performance has been discussed. In the post processing technique, influence of surface roughness is considered.

8.2 Processing Impact on Corrosion

Thermal Spray Gun Systems

Different thermal spray systems like APS, HVOF, cold spray had remarkably different microstructure which affects the corrosion performance of the coating. APS produces coatings with unmelted particles and microstructure can have high porosity. For Ni coating APS coating microstructure had interconnected porosity which led to poor corrosion performance. Also, for NiCr, coating deposited by APS showed diminished coating performance due to high porosity and presence of unmelted particles in the microstructure. Also, oxidation level is high in APS due to higher temperature. Higher oxidation of the coatings produces higher porosity. HVOF produces coatings which show mixed corrosion performance. Coatings produced by guns with independent temperature and velocity produce coating with compact microstructure and lower porosity. WCCoCr coating deposited by third generation gun produced coating with smoother and low porosity microstructure. Cold spray guns produce coatings with compact microstructure as obtained for Ni coatings. The higher velocity produced by the cold spray system enables particles with enormous velocity to undergo particle deformation and produce coatings with very small porosity.

Feed Rate

Feed rate is an important parameter which has large influence on the particle state. As observed in Ni studies with lower feed rate corrosion performance was poor due to overheating of particles. At higher feed rate the particles had to compete to get thermal energy for melting. Thus, due to inefficient heating of particles, the coating microstructures had large porosity and poor corrosion performance. In the case of NiCr velocity decreased due to drag force with increase in feed rate. Hence, velocity decreased with increase in feed rate. However, corrosion performance initially increases and then decreases with increase in feed rate.

Addition of Cr

Corrosion performance improved with addition to Cr to both the system Ni and WC-Co. Comparing the corrosion potential of Ni and NiCr as well as WC-Co and WC-Co/Cr, it can be observed that Ecorr for NiCr and WC-CoCr are higher than the system without Cr. Addition of Cr enables to form oxides of chromium which confers corrosion resistance to the system.

Oxygen/ Fuel Content

Oxidation of particles during flight affects the corrosion performance of the coating. Oxides are brittle and as the particles impinge on the substrate micro cracks can develop and porosity are induced in the microstructure of the coating. In HVOF in which oxygen and fuel are mixed to achieve combustion, it is observed that with increase in oxygen content corrosion performance decreases as was observed for NiCr and CrC-NiCr.

Thickness Impact

Thickness has profound effect on corrosion performance as described in previous chapters. With increase in thickness the electrolyte path becomes more tortuous and offers resistance to electrolyte. Furthermore, for optimized parameters there is a minimum thickness range below which the coatings offer poor corrosion protection to the substrate. For NiCr and WCCoCr it was observed that for coating thickness above 200 µm corrosion resistance was appreciable. However for CrC-NiCr corrosion resistance was not increasing monotonically with thickness. Residual stress was found to be important.

Porosity

Porosity is an important property which depends on processing parameter, stress and has the greatest influence on corrosion performance. Though there are different pores like semi-open, closed and open pores, open pores and semi-open pores affect corrosion performance drastically. Semi open pores present on surface can lead to pitting and crevice corrosion. Interconnected porosity leads to easy passage of electrolyte to the substrate. Finally, the electrolyte is simultaneously in contact with the substrate and coating which leads to galvanic corrosion. In thermal spray this form of corrosion due to interconnected porosity is common. Porosity is affected by different processing parameters. Velocity plays important role in affect porosity of the coatings. Higher velocity leads to peening and plastic deformation of the particles and thus aspect ratio. With flattening of particles there is better cohesion and porosity is reduced. However, with high velocity the likelihood of dwell time of particles in flame is reduced. Due to inefficient heating of particles melting state and deposition efficiency may be reduced. This in turn may affect porosity and coating thickness growth rate.

In the case of APS deposited Ni and NiCr, it was observed that the coatings had large porosity and unmelted particles which hampered their corrosion performance. HVOF coatings show reduced porosity and compact microstructure. Low temperature and high velocity feature of HVOF enables particles to get less oxidized and have proper melting state. There after the particles on impingement with the substrate, are well flattened and dense coating is obtained. It was observed for WC-Co/Cr -TG, the porosity was extremely low compared to WC-Co/Cr SG. For WC-Co/Cr -TG **,** temperature was low and velocity was high as compared to WC-Co/Cr-SG. This factors contributed to WC-Co/Cr -TG to achieve high compact microstructure and high corrosion performance.

Residual Stress

During deposition and post deposition process various stresses are introduced in the material system. Pores and interconnected path physical dimension changes under influence of residual stress. Compressive stresses tend to close the pores whereas tensile stress tends to widen the dimension of pores. Sometimes, coatings may crack under the influence of stress. In the corrosion investigation of NiCr and 75%Cr_3C_2-25 %NiCr coatings, those under compressive stress showed better corrosion performance compared to the coatings under tensile stress.

8.3 Post Processing Effects on Corrosion

Surface Polishing

Generally, thermal spray coatings have high roughness which affects the corrosion performance. The valleys present on the surface acts as starting point of pitting corrosion. As the surface is polished any pores present on the surface is closed and corrosion performance is improved. The effect of polishing on corrosion performance was clearly evident from WC-Co/Cr for which the corrosion potential increased from ~ -0.350 V to ~ -0.250 V after polishing. Moreover, with polishing corrosion potential was less dependent on thickness which resulted due to closing of surface pores.

Apart from the above influence on corrosion resistance performance, the effect of processing parameters on variability was investigated. For Ni, NiCr and WC-Co/Cr microstructure and variability had relation. Coatings with compact microstructure, less porosity showed lesser variability. Coatings with uniformity in microstructure had tight corrosion potential distribution. The corrosion potential variation study is important for understanding reliability of the coating and guarantying the corrosion performance within corrosion potential distribution.

Chapter 9

Conclusion of the Electrochemical Studies

Electrochemical studies performed on different thermal sprayed coatings were encouraging in validating thermal sprayed coatings for EHC replacement. The significant conclusion pertinent to the corrosion studies are:

1) **APS** deposited coatings have large porosity in their microstructure, due to which the probability of interconnected porosity increases with porosity level. This facilitates the passage of electrolyte or corrosive medium to the substrate which results into corrosion of the substrate. Hence, corrosion performance of the coating and thereby corrosion protection of the substrate is poor.

2) **Cold spray** produces coatings with compact microstructure which offers strong resistance for flow of electrolyte to the substrate. The corrosion performance of these coatings are excellent and at par with bulk counterpart.

3) **HVOF sprayed** coatings exhibit mixed corrosion performance. Some coatings show performance near to the substrate while other coatings exhibit excellent performance. The coating performance depends on the evolution of microstructure and porosity level. This in turn depends on the processing parameters selected during deposition. Many of the parameters are coupled and controlling the parameters to engineer the microstructure is complex in nature.

4) Interconnected porosity dictates the corrosion performance of the coating. Higher porosity increases the probability of interconnected porosity.

5) For HVOF moderate temperature ranges is suitable to semi melt or melt the particles so that on impact the splats are well flattened without oxidation or phase transformation. Similarly, high velocity enables the particle to peen the substrate and plastically deform the particle and forms flatten splats with lesser porosity. Independent control of temperature and velocity enable to reduce phase transformation of the particles.

6) Feed rate is one of the important parameter influencing particle temperature and thereby microstructure. For dense microstructure optimized feed rate is required. Lower feed rate overheat the particles and excessive oxidation can occur whereas higher feed rate results into inefficient heating and hence porous microstructure.

7) Higher oxygen flow results into oxidation whereas higher fuel acts as shroud and consumes neighboring ambient oxygen which results into low oxide content in the coating..

8) Coatings with compressive stress show better corrosion performance compared to coatings with tensile or lesser compressive stress.

9) There is certain minimum thickness (mostly~ 200 µm) of the coatings above which coating show better corrosion performance. However, other factors like residual stress, oxidation, particle state, etc factor are important along with thickness.

10) Surface polishing improves corrosion performance by closing surface pores.

11) Addition of Cr improves corrosion performance.

12) Presence of defects can undermine corrosion performance in best optimized coating.

Chapter 10

Future Scope of Present Work

The present study mainly aimed to understand processing effects on corrosion performance. To extend the present study and obtain knowledge of applicability of the thermal spray coatings under different adverse condition the following studies can be pursued:

10.1 Corrosion Studies of Amorphous TS Coatings

In the present study all the TS materials and coatings are in crystalline state. Amorphous material will not show in principle any grain boundaries. Consequently the concept of interconnected pores is weak and corrosion studies of such coatings will bring out importance of amorphous coatings in corrosion resistance applications.

10.2 Variations in Ambient Conditions

Present corrosion studies are conducted in neutral NaCl solution at room temperature. In future the studies will be conducted under varying temperature condition. Temperature has a marked influence on corrosion rate of the coatings. Furthermore, the effect of acidity or alkalinity on the TS samples will be carried out. Different metals show different response to the pH of the solution. Also, from corrosion perspective solubility of oxygen in an electrolyte has profound effect on corrosion. Combinations of these factors are deleterious and effects are multiplied. This study is useful from marine applications. The ocean and sea exhibit variation in temperature, pH and oxygen content throughout the part of the word.

10.3 X-ray Photoelectron Spectroscopy (XPS) /X-ray Diffraction

These characterization techniques will help in understanding formation of different ‘complexes’ and complex oxides during corrosion events. The formed metal complexes have deep implication on wear and erosion processes.

XPS involves the ejection of electrons usually from core level due to impingement of energetic x-ray photons. Binding energy of the emitted electrons can be accurately calculated by XPS. Furthermore, elements can not only be identified but also the chemical environment, oxidation state and concentrations of the elements can be obtained. XPS is a very highly surface sensitive popular research tool in corrosion science. It provides unambiguous chemistry and detailed mechanism of the corrosion process taking place on the surface. In TS coatings influence of different oxide content and passivation elements like Cr can be studied by XPS.

The advantage of XPS is that it is non-destructive technique. Most specimens are not affected by the energetic x-ray. Almost all elements across the periodic table can be detected by XPS. Furthermore, it gives the oxidation state of an element. It can be used to study amorphous materials. The major disadvantage of XPS is the stringent requirement of ultrahigh vacuum. Consequently, in-situ XPS studies on the TS sample is impossible.

Micro-diffraction studies will be carried to study stress and, phase formed before and after corrosion.

10.4 Post treatment effect on corrosion performance of TS coatings

Completed elimination of pores in TS coatings is highly difficult. The presence of pores deteriorates the corrosion performance of the coatings. In the present study different techniques to close the pores like laser sealing, organic/inorganic sealants, polishing techniques will be investigated.

Laser processing helps to remelt and fuse the TS coating surface. Polishing helps in reducing the surface area and consequently less geometrical surface is exposed to the electrolyte. Sealants help in closing the pores present in the TS coatings. However it is highly challenging to employ sealants for HVOF coatings due to minute pore size. The sealants cannot penetrate in the pores due to their viscosity. Furthermore, the integrity of sealant against UV radiation and aging is worth investigating for corrosion performance.

10.5 Stress Corrosion Cracking and Fatigue Corrosion Failure

Thermal spray coatings meant to replace hard chrome are subjected to corrosive atmosphere and external applied stress. Furthermore, TS coatings can have residual stress. These stresses results in enhanced corrosion failure called stress corrosion cracking (SCC). This form of corrosion study is important from the point of view of studying the failure mechanism of structural components in ships or landing gears of airplanes. Controlling the residual stress can enhance the corrosion performance under the applied stress in the corrosion environment.

Synchrotron radiation will be used to study the effect of simultaneous corrosion and tensile stress on cracking phenomenon. Synchrotron radiation due to its incomparable focusing ability can be used to study crack propagation. Micro-diffraction investigation on the stress corrosion cracking will help in understanding the influence of corrosion on crack propagation. The change in d spacing will be monitored by micro-diffraction at the tip point.

Furthermore, components coated with TS may be exposed to corrosive environment and cyclic stress. Due to these factors the adverse effects are intensified leading to the component failure. Fatigue cycle test will be carried out on substrate coated with TS coating and treated in salt fog or corrosive atmosphere.

References to Chapters

1) *Corrosion Understanding The Basics*, Chapter 1 Page no. 1, Edited by J. R. Davies, ASM International, USA.

2) Einar Mattson, Basic corrosion technology for scientists and engineers, 1989, Chapter 3, Ellis Horwood Limited,Great Britain.

3) R. Winston Revie and Herbert H.Uhlig, Corrosion and corrosion control- An introduction to corrosion science and engineering, 2008,Chapter 2, John Wiley and sons Inc, USA.

4) E. E. Stansbury and R. A. Buchanan, Fundamental of electrochemical corrosion,2000, Chapter 1, ASM, International, USA.

5) V. Raghavan, Materials science and engineering –a first course, 2004, Chapter 13, Prentice Hall-India.

6) Bruce. D. Craig, Fundamental aspects of corrosion films in corrosion science, 1991 Chapter 1, Plenum press.

7) Allen J. Bard and Larry R. Faulkner, Electrochemical methods –fundamentals and applications,2001, Chapter 1, John Wiley and sons Inc, USA.

8) Gamry application notes.www.gamry.com.

9) Adam Winkelman, Erik B. Svedberg, Robert E. Schafrik, David J. Duquette, *Preventing Corrosion from Wearing Our Future Away,* Advanced materials and processes 169 (2011) p.26.

10) W. Callister, *Introduction to materials Science and engineering*, Chapter 19, John Wiley and sons Inc.

11) Elisabete Almeida, *Surface Treatments and Coatings for Metals. A General Overview. 2. Coatings: Application Processes, Environmental Conditions during Painting and Drying, and New Tendencies*, Industrial engineering chemical research, 40 (2001) p. 15-20.

12) Gerard Barbezat, Arno Refke, Jorg Vetter and Montia Nestler, *Surface Solutions for the Requirements of Tomorrow*, Sulzer Technical Review 4(2007) p. 8-11.

13) Jochen Haring, *Modern Surface Solutions- More than Coatings*, Sulzer Technical Review, 4(2007) p. 4-7.

14) Daryl E. Crawmer, *Introduction to coatings, equipment, and theory* published in Handbook of Thermal Spray Technology edited by J. R. Davies, 2004, page 43-46, ASM International, USA.

15) H. Herman, S. Sampath and R. McCune: *Thermal Spray: Current status and future trends*, in Materials Research Bulletin, 25 (2000) p. 17- 25.

16) S. Sampath and H. Herman: *Rapid solidification and microstructure development during plasma spray deposition*, in Journal of Thermal Spray Technology, 5 (1996) p. 445- 456.

17) L. Pawlowski : *The science and engineering of thermal spray coatings*, 2008, Second edition, John Wiley & Sons.

18) Robert B. Heimann: *Plasma- spray coating principles and applications*, Chapter 1, page no 8, VCH.

19) www.sulzermetco.com.

20) S. Sampath: *Thermal Sprayed Ceramic Coatings: Fundamental issues and practical considerations*, Int. J. Materials and Product Technology, 35 (2009) p.425-447.

21) Atin Sharma, Andrew Gouldstone, Sanjay Sampath and Richard Gambino: *Anisotropic electrical conduction from heterogenous states in plasma sprayed* TiO_2 *coatings* in Journal of applied Physics, 100 (2006) p. 114906.

22) J. R. Davies: *Introduction to Thermal Spray Processing in Handbook of Thermal Spray Technology*,2004, p. 3-13, ASM International, Ohio, USA.

23) P. Fauchis, A. Vardelle, and B. Dussoubs: *Quo vadis thermal spraying?* in Journal of Thermal Spray Technology, 10 (2001) p.44- 66.

24) Z.Wang, A. Kulkarni, S. Deshpande, T. Nakamura and H. Herman: *Effect of pores and interfaces on effective properties of plasma sprayed zirconia coatings* in Acta Materialia,. 51 (2003) p. 5319 – 5334.

25) Image Courtesy- CTSR, SUNY AT Stony Brook, New York, U.S.; www.gordonengland.co.uk

26) Alfredo Valarezo, Ph.D thesis dissertation," Process Design for Reliable High Velocity Thermal Spray Coatings: An Integrated Approach through Process Maps and Advanced in *situ* Characterization, 2008.

27) Maria Oksa, Erja Turunen , Tomi Suhonen , Tommi Varis and Simo-Pekka Hannula, *Optimization and Characterization of High Velocity Oxy-fuel Sprayed Coatings: Techniques, Materials, and Applications,* Coatings 1(2011) p.17-52.

28) George P. Sutton and Oscar Biblarz, *Rocket propulsion Elements*, Chapter 2, John Wiley and sons Inc.2010.

29) J. Stokes and L. Looney, *HVOF system definition to maximise the thickness of formed components,* Surface and Coatings Technology 148 (2001) p.18-24.

30) www.twi.co.uk

31) H Edris, D. G. McCartney and A. J. Sturgeon, *Microstructural characterization of high velocity oxy-fuel sprayed coatings of Inconel 625*, Journal of Materials Science, 32(1997) p. 863-867.

32) Frank J. Hermanek, *What is thermal spray?* International thermal spray association, 5th edition, 2011.

33) Gotz Matthaus, Thermico Advanced Coating Solutions.

34) Gerard Barbezat and Klaus Landes, *Plasma Torch-System Triplex:Increased Production and a More Stable Process,* Sulzer Technical Review, 4 (1999) p. 32-35.

35) Terry Khaled, *A look at Hard Chrome Replacement*, Report # ANM -112N-01-02, FAA reports.

36) www.azom.com.

37) Jan Alexander: *Toxicity Versus Essentiality of Chromium* Scan. J Wok. Environ. Health, 19(1993) p. 126.

38) Sik Choi Kwon, K-H Lee, J-K Kim, M Kim, G-H Lee, K-S Nam, D Kim and D-Y Chang in *Plasma Aided Process as Alternative to Hard Chromium Electroplating*, J. Kor. Inst. Surf. Eng, 36 (2003) p.48-58.

39) L. Fedrizzi, S. Rossi, R. Cristel and P. L. Bonora: *Corrosion and wear behaviour of HVOF cermet coatings used to replace hard chromium* in Electrochimica Acta, 49 (2004) p. 2803-2814.

40) K. O. Legg, M. Graham, P. Chang, F. Rastagar, A. Gonzales, and B. Sartwell: *The replacement of Electroplating* in Surface and Coatings Technology, 81 (1996) p. 99- 105.

41) K. O. Legg and Bruce Sartwell, *Alternatives to Functional Hexavalent Chromium Coatings : HVOF Thermal Spray*, www.hazmat-alternatives.com.

42) Robert. B. Heimann and Hans D. Lehmann: *Recently patented work on thermally sprayed coatings for protection against wear and corrosion of engineered structures* in Recent Patents on Materials Science, 1 (008) p. 41-55.

43) J. E. Cho, S. Y. Huang and K. Y. Kim: *Corrosion behaviour of thermal sprayed WC coatings having various metallic binders in strong acidic environment in Surface and coatings technology*, 200 (2006) p. 2653-2662.

44) B. D. Sartwell, R. Kestler, K. O. Legg, W. Assink, A. Nardi and J. Schell : *Validation of HVOF WC/Co, wc/CoCr and Tribaloy 800 Thermal Spray Coatings as a replacement for hard chrome plating on C-2/ E-2/P-3 and C-130 propeller hub system components* in open public document, Naval Research Laboratory, Washington, DC 20375, 2003, p. 1-102.

45) D. Toma, W. Brandl and G. Marginean: *Wear and corrosion behavior of thermally sprayed cermet coatings* in surface and coatings technology, 138 (2001) p. 149-158.

46) C. Monticelli, A. Frignani and F. Zucchi: *Investigation on the corrosion process of Carbon steel coated by HVOF/Co cermets in neutal solution* in Corrosion Science, 2004, 46 (2004) p. 1225-1237.

47) G. Antou, G. Montavon, F. Hlawka, A. Cornet and C. Coddet*: Exploring thermal spray gray alumina coating pore network architecture by combining stereological protocols and impedence electrochemical spectroscopy* in Journal of Thermal Spray Technology, 2006, vol. 15 (2006) p.765-772.

48) Joan M. Perry, Anne Neville and Trevor Hodgkiess: *A comparison of the corrosion behavior of WC-Co-Cr and WC-Co HVOF thermally sprayed coatings by in situ atomic force microscopy (AFM)* in Journal of Thermal Spray Technology, 11(2002) p. 536-541.

49) A. M. Human and H. E. Exner: *The relationship between electrochemical behavior and in service corrosion of WC based cemented carbides* in Int. J. of Refractory Metals and Hard Materials, 15 (1997). 65-71.

50) A. M. Human and H. E. Exner: *Electrochemical behavior of tungsten-carbide hardmetals* in Materials science and Engineering A, A209 (1996) p. 180-191.

51) S. Sampath: *Thermal Sprayed Ceramic Coatings: Fundamental issues and practical considerations*, Int. J. Materials and Product Technology, 35 (2009) p, 425-447.

52) P. Fauchis, M. Fukumoto, A. Vardelle and M. Vardelle: *Knowledge concerning splat formation*: An Invited Review in Journal of Thermal Spray Technology, 13 (2004) p. 337-359.

53) I. A. Gorlach: *Development of thermal spraying process for anticorrosion surface protection* in Proceedings of the International Multi Conference of Engineers and Computer Scientists 2008 Vol II IMECS 2008, 19-21 March, 2008, Hong Kong.

54) S. Kuroda, H. Fujimori, T. Fukushima and S. Kitahara, *Measurement of Temperature and Velocity of Thermally Sprayed Particles using Thermal Radiation*, Transactions of Japan Welding Society, 22 (1991) 82-89.

55) A. Vaidya, V. Srinivasan, T. Streibl, M. Friis, W. Chi and S. Sampath: *Process maps for plasma spraying of yttria- stabilized zirconia: An integrated Approach to design, optimization and reliability* in Materials Science and Engineering A, 497 (2008) p. 239 – 253.

56) D. A. Stewart, P. H. Shipway and D. G. McCartney*: Microstructural evolution in thermally sprayed WC-Co coatings: Comparison between nanocomposite and conventional starting powders* in Acta Materialia, 48 (2000) p. 1593- 1604.

57) J. R. Davies: *Introduction to Thermal Spray Processing in Handbook of Thermal Spray Technology*, 2004, p. 3-13, ASM International, Ohio, USA.

58) J. E. Cho, S. Y. Huang and K. Y. Kim: *Corrosion behaviour of thermal sprayed WC coatings having various metallic binders in strong acidic environment in Surface and coatings technology*, 200 (2006) p, 2653-2662.

59) S. Tobe: *A review on protection from corrosion, oxidation and hot corrosion by thermal spray coatings* in Thermal Spray: Meeting the Challenges of the 21St Century: Procedings of the 15th International Thermal Spray Conference, 25 – 29 May 1998, Nice, France, p. 3 – 11.

60) Norio Sato: *Green corrosion chemistry and engineering : opportunity and challenges*, Edited by Sanjay K. Sharma, chapter 1, 2011, Wiley VCH.

61) Alec Groysman: *Corrosion for Everybody*, chapter 1, pp. 42, Springer.

62) Katharine B. Small, David A. Englehart and Todd A. Christmann: *Guide to etching specialty alloys in Advanced Materials and Processes*, February 2008, pp. 32-37.

63) R. Winston Revie and Herbert H. Uhlig: Corrosion and corrosion control- An introduction to corrosion science and engineering, 2008, Chapter 3, John Wiley and sons Inc, USA.

64) Gamry application notes on primer for electrochemistry, www.gamry.com.

65) C. W. Oatley, *The early history of the scanning electron microscope*, *J. Appl. Phys*, 53(1982) R1.

66) C. W. Oatley, W. C . Nixon and R. F. W. Pease: *Advances in Electronics and Electron Physics*, Edited by James. Dwyer McGee, 1966, Page 181, Volume 21, Elsevier Science and technology publisher.

67) Joseph Goldstein, Dale E. Newbury, David C. Joy, Charles E Lyman, Patrick Echlin, Eric Lifshin, Linda Sawyer and Joseph Michael: *Scanning Electron Microscopy and X-ray Microanalysis*, chapter 3, 2003, 3rd edition, Springer.

68) H. E. Exner: *Physical Metallurgy*, Edited by R. W. Cahn and P. Haasen, 1996, 4th edition, chapter 10, North Holland, Netherlands.

69) N Espallargas, J Berget, J Guilemany, A Benedetti, P Suegama, *Cr_3C_2-NiCr and WC-Ni thermal spray coatings as alternatives to hard chromium for erosion-corrosion resistance*,Surface Science Coatings and Technology,202(2008) p.1405-1417.

70) S. Sharafat, A. Kobayashi, S. Chen and N.M. Ghoniem, *Production of high-density Ni-bonded tungsten carbide coatings using an axially fed DC-plasmatron*, Surface and Coatings Technology 130 (2000) p. 164-172

71) C. J. Li, Y. Y. Wang, T. Wu, G. C. Ji, A. Ohmori, *Effect of types of ceramic materials in aggregated powder on the adhesive strength of high velocity oxy-fuel sprayed cermet coatings*, Surface Science Coatings and Technology,145(2001) p.113- 120.

72) C. Borchers, F. Gartner, T. Stoltenhoff and H. Kreye, *Microstructural bonding features of cold sprayed face centered cubic metals*, Journal of Applied Physics, 96 (2004) p. 4288-4292.

73) M. Magnani, P. H. Suegama, N. Espallargas, S. Dosta, C. S. Fugivara, J. M. Guilemany and A. V. Benedetti, *Influence of HVOF parameters on the corrosion and wear resistance of WC-Co coatings sprayed on AA7050 T7*, Surface and Coatings Technology, 202 (2008) p.4746-4757.

74) S. Kuroda, Y. Tashiro, H. Yumoto, S. Taira, H. Fukanuma, and S. Tobe, *Peening Action and Residual Stresses in High-Velocity Oxygen Fuel Thermal Spraying of 316L Stainless Steel*, Journal of Thermal Spray Technology, *10* (2001) p. 367-374.

75) M. Barlatta, G. Bolleli, B. Bonferroni and Lusvarghi. *Wear and corrosion behavior of HVOF-sprayed WC-CoCr coatings on Al alloys*, Journal of Thermal Spray Technology., 19 (2010) p. 358-367.

76) D. Zois, T. Wentz, R. Dey, C. Weyan, S. Sampath, Submitted to *J. Therm. Spray Technol*.

77) M.Magnani, P.H. Suegama, A. A. C. Recco, J.M. Guilemany, , C. S. Fugivara and A. V. Benedetti, *WC-CoCr coatings sprayed by high velocity oxygen-fuel (HVOF) flame on AA7050 aluminum alloy: electrochemical behavior in 3.5% NaCl solution*, Materials Research, 10 (2007) p. 377-385.

78) A.D. Mah, *Heats of Formation of Chromium Oxide and Cadmium Oxide from Combustion Calorimetry*, J. Am. Chem. Soc., 76 (1954) p 3363-3365.

79) C.M. Hackett, G.S. Settles and J.D. Miller, *On the Gas Dynamics of HVOF Thermal Sprays,* Proceedings of the 1993 National Thermal Spray Conference , Anaheim, CA, 7-11(June 1993) p.167-172.

80) J. Matejicek, S. Sampath, D. Gilmore, R. Neiser, *In situ measurement of residual stresses and elastic moduli in thermal sprayed coatings: Part 2: processing effects on properties of Mo coatings,* Acta Mater. 51, (2003) p. 873-885.

81) A. Vaidya, T. Streibl, L. Li, S. Sampath, O. Kovarik, R. Greenlaw, *An integrated study of thermal spray process-structure-property correlations: A case study for plasma sprayed molybdenum coatings., Mater. Sci. Eng.* A, 403(2005) p.191–204.

82) R. Ghafouri-Azar, J. Mostaghimi, S. Chandra, *Modeling development of residual stresses in thermal spray*, coatings *Comp. Mater. Sci*., 35 (2006) p. 13–26.

83) S. Koruda, T. Dendo, S. Kitahara, *Quenching stress in plasma sprayed coatings and its correlation with the deposit microstructure,* J. Thermal Spray Technol. 4 (1995) 75–84.

84) R. A. Itoh, M. Hirata and M. Ayagaki, Effects of Substrate Temperature During Spraying on the Properties of Sprayed Coatings *Proceedings of the 1993 National Thermal Spray Conference*, Anaheim, CA, 7-11 (June 1993) p. 593-600.

85) R. McPherson, *A review of microstructure and properties of plasma sprayed ceramic coatings, Surf. Coat. Technol.*, 39/40 (1981) p 173-181.

86) Robert. B. Heimann and Hans D. Lehmann: *Recently patented work on thermally sprayed coatings for protection against wear and corrosion of engineered structures* in Recent Patents on Materials Science, 1(2008) p. 41-55.

87) J. E. Cho, S. Y. Huang and K. Y. Kim: *Corrosion behaviour of thermal sprayed WC coatings having various metallic binders in strong acidic environment in Surface and coatings technology*, 200(2006) p.2653-2662.

88) D. Toma, W. Brandl and G. Marginean: *Wear and corrosion behavior of thermally sprayed cermet coatings* in surface and coatings technology, 138 (2001), p. 149-158.

89) C. Monticelli, A. Frignani and F. Zucchi: *Investigation on the corrosion process of Carbon steel coated by HVOF/Co cermets in neutal solution* in Corrosion Science, 46(2004) p. 1225-1237.

90) G. Antou, G. Montavon, F. Hlawka, A. Cornet and C. Coddet*: Exploring thermal spray gray alumina coating pore network architecture by combining stereological protocols and impedence electrochemical spectroscopy* in Journal of Thermal Spray Technology, 15 (2006) p.765-772.

91) Joan M. Perry, Anne Neville and Trevor Hodgkiess: *A comparison of the corrosion behavior of WC-Co-Cr and WC-Co HVOF thermally sprayed coatings by in situ atomic force microscopy (AFM)* in Journal of Thermal Spray Technology, 11 (2002) p. 536-541.

92) A. M. Human and H. E. Exner: *The relationship between electrochemical behavior and in service corrosion of WC based cemented carbides* in Int. J. of Refractory Metals and Hard Materials, 15 (1997)p. 65-71.

93) A. M. Human and H. E. Exner: *Electrochemical behavior of tungsten-carbide hardmetals* in Materials science and Engineering A, A209(1996) p. 180-191.

94) V. Souza and A. Neville, *"Mechanisms and kinetics of WC-Co-Cr high velocity oxy-fuel thermal spray coating degradation in corrosive environmen", Journal of Thermal Spray Technology*, 15, (2006) p. 106-117.

95) L. Fedrizzi, S. Rossi, R. Cristel, P. L. Bonora, *Corrosion and wear behaviour of HVOF cermet coatings used to replace hard chromium*, Electrochemica Acta, 49 (2004) p. 2803-2814.

96) M.Magnani, P. H. Suegama, N. Espallargas, S. Dosta, C. S. Fugivara, J. M. Guilemany, A. V. Benedetti: *Influence of HVOF parameters on the corrosion and wear resistance of WC-Co coatings sprayed on AA7050T7* in Surface and Coatings Technology, 202 (2008) p. 4746-4757.

97) P. H. Suegama, C. S. Fugivara, A. V. Benedetti, J. Fernandez, J. Delgado, J. M. Guilemany, *Electrochemical behavior of thermally sprayed stainless steel coatings in 3.4% NaCl solution*, Corrosion Science, 47 (2005) p. 605-620.

98) M. Magnani, P. H.Suegama, N. Espallargas, C. S. Fugivara, S. Dosta, J. M. Guilemany and A. V. Benedetti, *Corrosion and Wear Studies of Cr_3C_2NiCr-HVOF Coatings Sprayed on AA7050 T7 Under Cooling*, Journal of Thermal Spray Technology, 18 (2009) p. 353-363.

99) T. A. Skothein, R. L. Elsenbaumer and J. R. Reynolds, *Handbook of Conducting Polymers*, chapter 31, 1998, Marcel and Dekker. Inc, New York, USA.

100) S. Houdkova, M. Kasparova, F. Zahalka, *The Influence of Spraying Angle on Properties of HVOF Sprayed Hardmetal Coatings*, Journal of Thermal Spray Technology, 19 (2010) p. 893-901.

101) S. H. Leigh, C. C. Berndt, *Evaluation of off-angle thermal spray*, Surface and Coatings Technology, 89 (1997) p. 213-224.

102) W. Tillman, E. Vogli, B.Krebs, *Influence of the Spray Angle on the Characteristics of Atmospheric Plasma Sprayed Hard Material Based Coatings*, Journal of Thermal Spray Technology, 17 (2008) p. 948-955.

103) Panadda Niranatlumpong and Hathaipat Koiprasert, *Improved corrosion resistance of thermally sprayed coating via surface grinding and electroplating techniques*, Surface & Coatings Technology, 201 (2006) p. 737–743.

104) E. Arslan, Y. Totik, E. Demirci, and A. Alsaran, *Influence of Surface Roughness on Corrosion and Tribological Behavior of CP-Ti After Thermal Oxidation Treatment*, Journal of Materials Engineering and Performance, 19 (2010) p. 428- 433.

105) G. Chen, X. Wen and N. Zhang, *Corrosion Resistance and Ion Dissolution of Titanium with Different Surface Microroughness,* BioMed. Mater.Eng, 8(1998) p. 61-74.

106) J.M. Guilemany , N. Espallargas , P.H. Suegama and A.V. Benedetti, *Comparative study of Cr3C2–NiCr coatings obtained by HVOF and hard chromium coatings*, Corrosion Science 48 (2006) 2998–3013.

107) J.M. Guilemany, N. Espallargas, P.H. Suegama, A.V. Benedetti, and J. Fernández, *High-Velocity Oxyfuel* Cr_3C_2*-NiCr Replacing Hard Chromium Coatings*, Journal of Thermal Spray Technology, 14(2005)335- 341.

108) J.A. Picas, A. Forn, G. Matthaus, *HVOF coatings as an alternative to hard chrome for pistons and valves,* Wear 261 (2006) 477–484.

109) Maria Oksa 1, Erja Turunen , Tomi Suhonen , Tommi Varis and Simo-Pekka Hannula, *Optimization and Characterization of High Velocity Oxy-fuel Sprayed Coatings: Techniques,* Materials, and Applications, Coatings 1(2011),17-52.

110) J.-J. Han, R. Knight, L.S. Schadler, *Residual Stresses in HVOF-Sprayed Cr3C2/NiCr-Coatings*, Thermal Spray 1999: United Thermal Spray Conference (DVS-ASM),pages 771-776.

111) J. Kawakita, S. Kuroda, T. Fukushima, *Development of Dense Corrosion Resistant Coatings By an Improved HVOF Spraying Process*, Thermal Spray 2003: Advancing the science & applying the technology, (Ed.) C. moreau and B Marple,Page 353- 359, Published by ASM International, Materials Park, Ohio, USA, 2003.

112) D. P .Kashyap 1, T.S Sidhu 1 , S. Prakash, *Parametric effects of HVOF Process on erosion corrosion behavior of coatings-A Review*, National Conference on Advancements and Futuristic Trends in Mechanical and Materials Engineering (February 19-20, 2010) India.